



AIRBUS



POLITECNICO DI TORINO

Corso di Laurea Magistrale in Ingegneria Aerospaziale

Tesi di Laurea Magistrale

Optimization for Propulsion Airframe Architecture set-up

Candidata :
Naomi LUGLIO

Relatori :
Remi AMARGIER
Simone CONIGLIO
Marco GHERLONE
Joseph MORLIER

Anno Accademico 2019/2020

Abstract — The Ultra High Bypass Ratio Turbofan (UHBR) has the potential to provide an important reduction in noise and burnt fuel compared to the existing subsonic engines. Unfortunately, its integration in our commercial aircraft induces some problems that have not been solved yet: between them, the increased weight of the propulsion architecture with, consequently, higher inertial and aerodynamics loads. The present work is the result of an internship at Airbus and it aims to investigate the possibility of an innovative Power Plant Structure design to make the UHBR integration easier and more efficient. The Free Size Optimization and the Topology Optimization were used for this purpose. Several design criteria were taken into account during the optimization processes: the stiffness of the Power Plant Structure, the loads on the Outlet Guide Vane blades and the impact of tip clearance variation into the Thrust Specific Fuel Consumption. Firstly, the possibility of reducing the tip clearance variations during aircraft operations by optimizing the dimensions of the Inner Fixed Structure of the Thrust Reverser Unit was investigated through the Free Size Optimization. Secondly, the Topology Optimization method was used to optimize the topology and connectivity of a Large Design Space including the Power Plant Structure. Before the present work, this Large Design Space model was supposed to be glued to the engine: that made the structure to have an high Degree of Static Indeterminacy. Actually, since highly hyperstatic structures can not well support thermal deformations, the engine mounts of currently operating aircraft are made up of hinged assemblies. That is the reason why, in order to make our Topology Optimization solutions more manufacturable, by introducing more realistic modelling hypothesis, in this work the glued interfaces between pylon and engine were replaced by discrete assemblies: the latter can be considered as simple models of the hinged assemblies currently used on real operating aircraft. In order to evaluate the impact of the load path on the Power Plant Structure and its performances, three different configurations of discrete assemblies were considered and compared. Moreover, in order to evaluate the influence of two important engine deformation criteria on the Power Plant Structure, two formulations were adopted for the optimization problem. The *Classic Formulation* aims to minimize the compliance under a volume fraction constraint while in the *Complete Formulation* two additional constraints were added: one to limit the *Thrust Specific Fuel Consumption* variation caused by tip clearance degradation and one to control the loads on the blades of the Outlet Guide Vane. This work provided a deep understanding about the *cowl load sharing* for the Power Plant Structure and a better knowledge concerning the impact of some engine deformation design criteria on the optimal solution.

Keywords : Ultra High Bypass Ratio, innovative pylon design, tip clearance, compliance, OGV blade loads, Topology Optimization, Free Size Optimization, hyperstatic structures, discrete assemblies.

Contents

Introduction	1
0.1 Work context	1
0.2 Motivations	1
0.3 Objectives	3
0.4 Overview	4
1 The Ultra High Bypass Ratio Turbofan	5
1.1 Turbofan Engines	5
1.2 Promises of the UHBR Turbofan	5
1.3 Challenges of the UHBR Turbofan	7
1.3.1 Fuel consumption minimum point	7
1.3.2 Core components dimensions	7
1.3.3 Aerodynamic issues	7
1.3.4 Deformations	8
2 Structure Optimization	10
2.1 Software Environment	10
2.2 Finite Element Method	10
2.3 Optimal Solution Conditions	11
2.4 CONLIN method	12
2.5 Dual Method Approach	14
2.6 Free Size Optimization	15
2.7 Topology Optimization	16
2.7.1 Implicit Methods	16

2.7.2	<i>Solid Isotropic Material with Penalization (SIMP)</i>	16
2.7.3	Numerical instabilities using SIMP approach	18
2.7.4	Explicit Methods	22
2.8	Objective and constraint aggregations	24
2.9	Convergence Criteria	24
3	Power Plant and Performance Modelling	26
3.1	Power Plant Structure	26
3.2	State of art of the project and new objectives	29
3.3	Tip Clearance Model	30
3.4	Outlet Guide Vane Moment Model	34
4	Free Size Optimization	36
4.1	FS Design Space	36
4.2	Free Size Optimization Problem	37
4.3	Free Size Optimization Results	38
4.4	Free Size Optimization Conclusion	40
5	Topology Optimization Problem Formulation	42
5.1	Design Space for the Topology Optimization	42
5.1.1	Boundary Conditions	43
5.1.2	Materials	44
5.1.3	Multi-Model Topology Optimization	45
5.2	Introduction of Discrete Assemblies	45
5.3	Topology Optimization Formulation	50
6	Topology Optimization Results without constraints on $TSFC$ and M_{OGV}	53
6.1	<i>FRMX</i> Configuration	53
6.2	<i>REMX</i> Configuration	59
6.3	<i>FAN_REMX</i> Configuration	65
6.4	Topology Optimization with glued interfaces between the Design Space and the Engine	71

7	Topology Optimization Results with constraints on $TSFC$ and M_{OGV}	76
7.1	Topology Optimization of $FRMX$ configuration - Complete Formulation . .	76
7.2	Pareto front	79
7.2.1	$TSFC$ Pareto Front	81
7.2.2	M_{OGV} Pareto	82
8	Conclusions and Perspectives	88
9	Annexes	90
9.1	$TSFC$ Pareto - Optimization Convergence	90
9.2	M_{OGV} Pareto - Optimization Convergence	94

List of Figures

1	Passenger - Kilometer Performed - ICAO Statics - source:[ICAO 2018] . . .	2
2	Carbon emission trend through 2050 - NASA - source:[NASA 2013]	3
1.1	Turbofan cut section - source:[Richter 2011]	6
1.2	Effect of fan BPR on fuel burn - source:[C.E. Hughes 2013]	6
1.3	Axisymmetric clearance change - source [S. Lattime 2002]	9
1.4	Asymmetric clearance change - source: [S. Lattime 2002]	9
2.1	Finite Element Discretization - Mesh of a turbine blade - source [Kenneth H. Huebner 2001]	11
2.2	Optimized result of a cantilever beam (<i>a</i>) with (<i>b</i>) and without (<i>c</i>) checker- board pattern (source [GW. Jang 2003])	21
3.1	Pylon primary structure location - source: Airbus Internal Documents . . .	27
3.2	Pylon primary structure components - source: Airbus Internal Documents	27
3.3	Pylon secondary structure location - source: Airbus Internal Documents - authors: CROS, SERRA, PERROT	27
3.4	Location and description of the nacelle - source: Airbus Internal Documents - authors: CROS	28
3.5	Airflow pattern with activated TRU - source: Airbus Internal Documents .	28
3.6	C-Duct and D-Duct diagram	28
3.7	Radial displacement effect on tip clearances	30
3.8	Relative displacement between the rotor shaft and the casing axis	31
3.9	Diagram of RBE3 element for casing average displacement	32
3.10	Model set-up between OGV blades and fan case - source: [Capasso 2019] .	34

4.1	Inner Fixed Structure - <i>C-Duct</i> configuration	37
4.2	Inner Fixed Structure with lower bifi in the <i>D-Duct</i> configuration.	38
4.3	Thickness distribution as result of the FS optimization for the C-duct configuration	39
4.4	Thickness distribution as result of the FS optimization for the D-duct configuration	40
4.5	Volume fraction evolution during Free Size optimization of IFS thickness .	40
4.6	Objective evolution during Free Size optimization of IFS thickness	41
5.1	Design Space for Topology Optimization (on the left) - Cut Section of the Design Space for Topology Optimization (on the right)	43
5.2	Interfaces between the Design Space and the other components	44
5.3	Stow and Reverse configuration - source: Airbus Internal Documents - author: Borrel Luce	45
5.4	Example of rear and forward mount - source: Airbus Internal Documents - Author: Edso	47
5.5	Removed TIE surfaces between DS and engine	47
5.6	FRMX configuration rods	49
5.7	REMX configuration rods	49
5.8	FAN_REMX configuration rods	49
5.9	Connecting rod general model	49
5.10	Thrust rod modelling	50
6.1	Density distribution for FRMX configuration - Classic Formulation - Threshold $\rho = 0.2$	54
6.2	FRMX architecture - Loads transmitted to the Power Plant Structure by the connecting rods for an academic load case	54
6.3	Design space compliance history over iterations for <i>FRMX</i> configuration .	57
6.4	Optimization Objective history over iterations for <i>FRMX</i> configuration . .	57
6.5	V/V^* hystory over iterations for <i>FRMX</i> configuration	57
6.6	Total compliance variation compared to baseline for <i>FRMX</i> configuration .	57
6.7	OGV bending moment variation compared to baseline for <i>FRMX</i> configuration	58
6.8	TSFC aggregation variation compared to baseline for <i>FRMX</i> configuration	58

6.9	TSFC variation for each component and its aggregation compared to baseline for <i>FRMX</i> configuration	58
6.10	Density distribution for REMX configuration - Classic Formulation - Threshold $\rho = 0.2$	59
6.11	REMX architecture - Loads transmitted to the Power Plant Structure by the connecting rods for an academic load case	61
6.12	Design space compliance history over iterations for <i>REMX</i> configuration	63
6.13	Optimization Objective history over iterations for <i>REMX</i> configuration	63
6.14	V/V^* history over iterations for <i>REMX</i> configuration	63
6.15	Design Space compliance variation compared to <i>FRMX</i> for <i>REMX</i> configuration	63
6.16	OGV bending moment variation compared to <i>FRMX</i> for <i>REMX</i> configuration	64
6.17	TSFC aggregation variation compared to <i>FRMX</i> for <i>REMX</i> configuration	64
6.18	TSFC variation for each component and its aggregation compared to <i>FRMX</i> for <i>REMX</i> configuration	64
6.19	Density distribution for FAN_REMX configuration - Classic Formulation - Threshold $\rho = 0.2$	65
6.20	<i>FAN_REMX</i> architecture - Loads transmitted to the Power Plant Structure by the connecting rods for an academic load case	67
6.21	Design space compliance history over iterations for <i>FAN_REMX</i> configuration	68
6.22	Optimization Objective history over iterations for <i>FAN_REMX</i> configuration	68
6.23	V/V^* history over iterations for <i>FAN_REMX</i> configuration	68
6.24	Design Space compliance variation compared to <i>FRMX</i> for <i>FAN_REMX</i> configuration	68
6.25	OGV bending moment variation compared to <i>FRMX</i> for <i>FAN_REMX</i> configuration	69
6.26	TSFC aggregation variation compared to <i>FRMX</i> for <i>FANconfiguration</i>	69
6.27	TSFC variation for each component and its aggregation compared to <i>FRMX</i> for <i>FAN_REMX</i> configuration	70
6.28	Density distribution for model with glued interfaces between the engine and the Design Space - Classic Formulation - Threshold $\rho = 0.2$	72
6.29	Glued interfaces model - Loads transmitted to the Power Plant Structure by the connecting rods for an academic load case	73

6.30	Design space compliance history over iterations for configuration with glued Design Space-Engine interfaces	74
6.31	Optimization Objective history over iterations for configuration with glued Design Space-Engine interfaces	74
6.32	V/V^* history over iterations for configuration with glued Design Space-Engine interfaces	74
6.33	Design Space compliance variation compared to <i>FRMX</i> for <i>TIE</i> configuration	74
6.34	OGV bending moment variation compared to <i>FRMX</i> for <i>TIE</i> configuration	75
6.35	TSFC aggregation variation compared to <i>FRMX</i> for <i>TIE</i> configuration . .	75
6.36	TSFC variation for each component and its aggregation compared to <i>FRMX</i> for <i>TIE</i> configuration	75
7.1	Density distribution for <i>FRMX</i> configuration - Complete Formulation - Threshold $\rho = 0.2$	77
7.2	<i>FRMX</i> architecture - Loads transmitted to the Power Plant Structure by the connecting rods for an academic load case - $F_{x0}, F_{y0}, F_{z0}, M_{x0}$ are the resultant applied load components - Complete Formulation	78
7.3	Design space compliance history over iterations for <i>FRMX</i> configuration - Complete formulation	79
7.4	Optimization Objective history over iterations for <i>FRMX</i> configuration - Complete formulation	79
7.5	V/V^* history over iterations for <i>FRMX</i> configuration - Complete formulation	79
7.6	Optimization Responses history over iterations for <i>FRMX</i> configuration - Complete formulation	79
7.7	Design Space compliance variation of the Complete formulation compared to the Classic Formulation	80
7.8	OGV bending moment variation of the Complete formulation compared to the Classic Formulation	80
7.9	TSFC aggregation variation of the Complete formulation compared to the Classic Formulation	80
7.10	TSFC variation for each component and its aggregation of the Complete formulation compared to the Classic Formulation	81
7.11	Pareto Front respect to <i>TSFC</i> constraint - <i>FRMX</i> configuration - Complete formulation	83

7.12	Variation of the bending moment on the OGV blades that is obtained by gradually decreasing the <i>TSFC</i> upper limit - <i>FRMX</i> configuration - Complete formulation	83
7.13	$\pi(TSFC_{j \in J_1}, p) / \pi(TSFC_{0j \in J_1}, p) = 0.85$; $\pi(M_{OGV_{j \in J_2}}, p) / \pi(M_{OGV_{0j \in J_2}}, p) = 0.85$ - Complete Formulation - Threshold=0.2	84
7.14	$\pi(TSFC_{j \in J_1}, p) / \pi(TSFC_{0j \in J_1}, p) = 0.75$; $\pi(M_{OGV_{j \in J_2}}, p) / \pi(M_{OGV_{0j \in J_2}}, p) = 0.85$ - Complete Formulation - Threshold=0.2	84
7.15	$\pi(TSFC_{j \in J_1}, p) / \pi(TSFC_{0j \in J_1}, p) = 0.65$; $\pi(M_{OGV_{j \in J_2}}, p) / \pi(M_{OGV_{0j \in J_2}}, p) = 0.85$ - Complete Formulation - Threshold=0.2	85
7.16	$\pi(TSFC_{j \in J_1}, p) / \pi(TSFC_{0j \in J_1}, p) = 0.55$; $\pi(M_{OGV_{j \in J_2}}, p) / \pi(M_{OGV_{0j \in J_2}}, p) = 0.85$ - Complete Formulation - Threshold=0.2	85
7.17	Pareto Front respect to M_{OGV} constraint - <i>FRMX</i> configuration - Complete formulation	86
7.18	$\pi(TSFC_{j \in J_1}, p) / \pi(TSFC_{0j \in J_1}, p) = 0.85$ $\pi(M_{OGV_{j \in J_2}}, p) / \pi(M_{OGV_{0j \in J_2}}, p) = 0.85$ - Complete Formulation - Threshold=0.2	86
7.19	$\pi(TSFC_{j \in J_1}, p) / \pi(TSFC_{0j \in J_1}, p) = 0.85$ $\pi(M_{OGV_{j \in J_2}}, p) / \pi(M_{OGV_{0j \in J_2}}, p) = 0.45$ - Complete Formulation - Threshold=0.2	87
7.20	$\pi(TSFC_{j \in J_1}, p) / \pi(TSFC_{0j \in J_1}, p) = 0.85$ $\pi(M_{OGV_{j \in J_2}}, p) / \pi(M_{OGV_{0j \in J_2}}, p) = 0.20$ - Complete Formulation - Threshold=0.2	87
9.1	Design space compliance history over iterations for <i>FRMX</i> configuration - Complete formulation - $TSFC/TSFC_0 = 0.75$ $M_{OGV}/M_{OGV_0} = 0.85$	91
9.2	Optimization Objective history over iterations for <i>FRMX</i> configuration - Complete formulation - $TSFC/TSFC_0 = 0.75$ $M_{OGV}/M_{OGV_0} = 0.85$	91
9.3	V/V^* history over iterations for <i>FRMX</i> configuration - Complete formulation - $TSFC/TSFC_0 = 0.75$ $M_{OGV}/M_{OGV_0} = 0.85$	91
9.4	Optimization Responses history over iterations for <i>FRMX</i> configuration - Complete formulation - $TSFC/TSFC_0 = 0.75$ $M_{OGV}/M_{OGV_0} = 0.85$	91
9.5	Design space compliance history over iterations for <i>FRMX</i> configuration - Complete formulation - $TSFC/TSFC_0 = 0.65$ $M_{OGV}/M_{OGV_0} = 0.85$	92
9.6	Optimization Objective history over iterations for <i>FRMX</i> configuration - Complete formulation - $TSFC/TSFC_0 = 0.65$ $M_{OGV}/M_{OGV_0} = 0.85$	92
9.7	V/V^* history over iterations for <i>FRMX</i> configuration - Complete formulation - $TSFC/TSFC_0 = 0.65$ $M_{OGV}/M_{OGV_0} = 0.85$	92
9.8	Optimization Responses history over iterations for <i>FRMX</i> configuration - Complete formulation - $TSFC/TSFC_0 = 0.65$ $M_{OGV}/M_{OGV_0} = 0.85$	92

9.9	Design space compliance history over iterations for <i>FRMX</i> configuration - Complete formulation - $TSFC/TSFC_0 = 0.55$ $M_{OGV}/M_{OGV_0} = 0.85$	93
9.10	Optimization Objective history over iterations for <i>FRMX</i> configuration - Complete formulation - $TSFC/TSFC_0 = 0.55$ $M_{OGV}/M_{OGV_0} = 0.85$	93
9.11	V/V^* history over iterations for <i>FRMX</i> configuration - Complete formulation - $TSFC/TSFC_0 = 0.55$ $M_{OGV}/M_{OGV_0} = 0.85$	93
9.12	Optimization Responses history over iterations for <i>FRMX</i> configuration - Complete formulation - $TSFC/TSFC_0 = 0.55$ $M_{OGV}/M_{OGV_0} = 0.85$	93
9.13	Design space compliance history over iterations for <i>FRMX</i> configuration - Complete formulation - $TSFC/TSFC_0 = 0.85$ $M_{OGV}/M_{OGV_0} = 0.45$	94
9.14	Optimization Objective history over iterations for <i>FRMX</i> configuration - Complete formulation - $TSFC/TSFC_0 = 0.85$ $M_{OGV}/M_{OGV_0} = 0.45$	94
9.15	V/V^* history over iterations for <i>FRMX</i> configuration - Complete formulation - $TSFC/TSFC_0 = 0.85$ $M_{OGV}/M_{OGV_0} = 0.45$	94
9.16	Optimization Responses history over iterations for <i>FRMX</i> configuration - Complete formulation - $TSFC/TSFC_0 = 0.85$ $M_{OGV}/M_{OGV_0} = 0.45$	94
9.17	Design space compliance history over iterations for <i>FRMX</i> configuration - Complete formulation - $TSFC/TSFC_0 = 0.85$ $M_{OGV}/M_{OGV_0} = 0.20$	95
9.18	Optimization Objective history over iterations for <i>FRMX</i> configuration - Complete formulation - $TSFC/TSFC_0 = 0.85$ $M_{OGV}/M_{OGV_0} = 0.20$	95
9.19	V/V^* history over iterations for <i>FRMX</i> configuration - Complete formulation - $TSFC/TSFC_0 = 0.85$ $M_{OGV}/M_{OGV_0} = 0.20$	95
9.20	Optimization Responses history over iterations for <i>FRMX</i> configuration - Complete formulation - $TSFC/TSFC_0 = 0.85$ $M_{OGV}/M_{OGV_0} = 0.20$	95

List of the abbreviations

UHBR	<i>Ultra High Bypass Ratio Turbofan</i>
IFS	<i>Inner Fixed Structure</i>
PPS	<i>Power Plant Structure</i>
ICAO	<i>International Civil Aviation Organization Council</i>
TSFC	<i>Thrust Specific Fuel Consumption</i>
BPR	<i>Bypass Ratio</i>
FPR	<i>Fan Pressure Ratio</i>
TRU	<i>Thrust Reverser Unit System</i>
OFS	<i>Outer Fixed Structure</i>
FEM	<i>Finite Element Method</i>
OGV	<i>Outlet Guide Vane</i>
TBS	<i>Torque Box Structure</i>
MPC	<i>Multipoint Constrain Equation</i>
LPC	<i>Low Pressure Compressor</i>
HPC	<i>High Pressure Compressor</i>
HPT	<i>High Pressure Turbine</i>
LPT	<i>Low Pressure Turbine</i>
DS	<i>Design Space</i>
DSI	<i>Degree of Static Indeterminacy</i>

SIMP	<i>Solid Isotropic Material with Penalization</i>
CONLIN	<i>Convex Linearization Method</i>
PKP	<i>Passenger Kilometer Performed</i>
LDS	<i>Large Design Space</i>
FS	<i>Free Size</i>

Introduction

0.1 Work context

This *Final Project Report* is the result of an internship at *Airbus Operations SAS*, in Toulouse. It should have lasted 6 months but, because of the Covid-19 pandemic, it has been reduced to 4 months. Despite the particular moment, I was warmly welcomed in the *Transverse Stress Team*, which is devoted to the stress analysis of the propulsion airframe. Our team is part of the *Engineering Structure group* which is composed of engineers whose work is dedicated to the Structure Analysis and Design. Our team engagement as long as a strong collaboration with the other teams allow us to identify and to take into consideration all the propulsion set-up requirements.

On the first day of work, a meeting with the main supervisor was organized in order to establish the objectives of the internship and to define a road-map. Then, after a short period which was dedicated at getting more familiar to the software environment, I was fully devoted to the accomplishment of the internship goals. Regular meetings were organized between me and my supervisors in order to expose and discuss the obtained results as well as the next steps of the internship. I worked in autonomy but my supervisors were always available to discuss and answer my questions.

Moreover, I was very involved in the dynamics of all the *Transverse Stress Team*, taking part to weekly meetings concerning the team budget and goals and joining them in convivial launches.

0.2 Motivations

This project exists at Airbus in the perspective to reach a more *eco-friendly* aviation. Passengers air traffic keeps growing around the world and doesn't seem to slow down. In fig.1 it is possible to see the increase of Passenger-Kilometer Performed (PKP) in the last 10 years according to the International Civil Aviation Organization Council (ICAO). Airbus plans a 4.3% increase in the average annual global traffic rate over the period 2019-2038 [Airbus], while Boeing forecasts a 4.6%/yr increase over the same period [Boeing]. Ac-

commodating such a growth will imply greater aircraft fleets, more flights, sky jams, more polluting emissions and continuous noise near airports. It is evident that the consequences on the health and quality life of worldwide citizens could not be positive. For example, fig.2 shows that, if no measures are taken, carbon emissions will grow dramatically through 2050. According to [E. Terrenoire 2019], in 2050 the aviation sector could be responsible for more than 2% of the total anthropogenic warming associated to fossil fuel emissions. That is the reason why aircraft manufacturers are now dealing with the necessity to make the aviation sector as *eco-friendly* as possible. In order to improve citizens life near the airport and to reduce the aviation impact on atmosphere quality, it is necessary to reduce noise and polluting emissions. For this purpose, researchers are engaged on several fronts: combustor temperatures and pressure ratio inside the aircraft, new engine concepts, better control systems, alternative thermodynamic cycles, potential alternative aviation fuels, aerodynamic improvements provided by new aircraft concepts, new aircraft systems, optimized flight and ground operations, etc. Between the research fields, the Ultra High Bypass Ratio Turbofan (UHBP) concept has the potential for significant reductions of burnt fuel, noise and emissions. Unfortunately, this new engine concept would induce some challenges which have to be solved in order to make its integration on commercial aircraft possible and efficient. In such a context, our project aims to search and investigate an innovative light integrated Power Plant Structure (PPS) which would be able to make the UHBP integration into commercial aircraft possible and efficient. For this purpose, in this work the structural Free Size Optimisation, as well as the Topology Optimization, were employed.

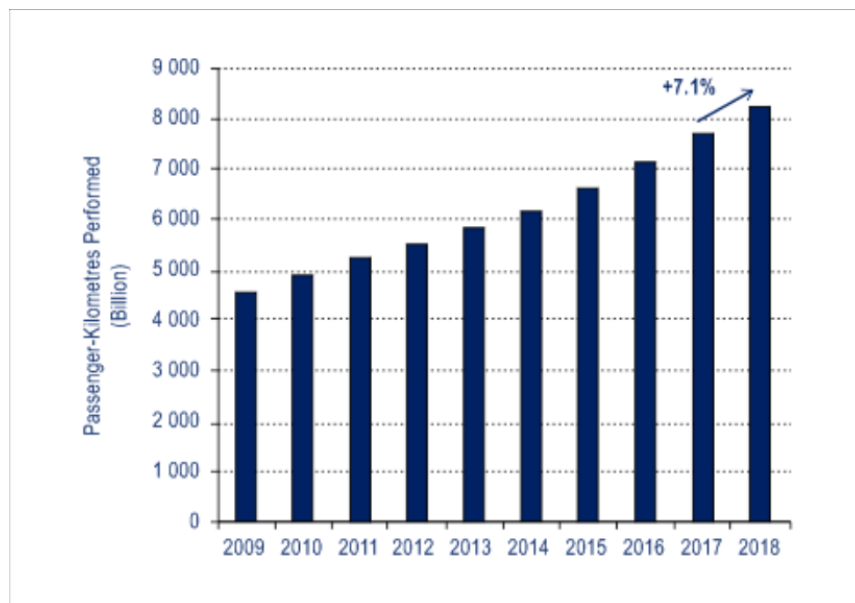


Figure 1: Passenger - Kilometer Performed - ICAO Statics - source:[ICAO 2018]

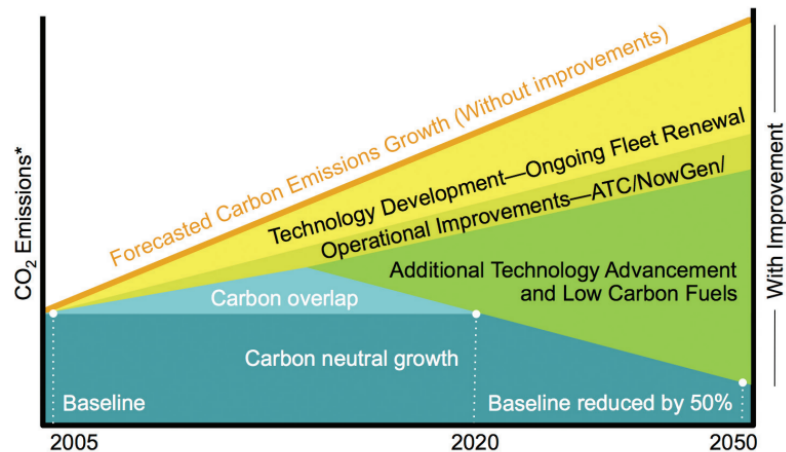


Figure 2: Carbon emission trend through 2050 - NASA - source:[NASA 2013]

0.3 Objectives

Before this work, two similar internships took place at Airbus to apply the Topology Optimization Method to a Large Design Space which included the Power Plant Structure. During these previous works, it seemed that a more stiff Inner Fixed Structure (IFS) of the Thrust Reverser Unit (TRU) could be beneficial for the limitation of tip clearance variation during the aircraft operations. For this reason, the first objective of the present work was to verify this possibility by the application of the Free Size Optimization on the IFS.

The second goal of this work was to resume the Topology Optimization on the Large Design Space by improving the modelling hypothesis. In fact, before the present work, the Large Design Space was supposed to be glued to the engine: that made the structure model to have a high Degree of Static Indeterminacy. In the real-life, since highly hyperstatic structures can not well support thermal deformations, the engine mounts of currently operating aircraft are made up of hinged assemblies. That is the reason why, in order to make our Topology Optimization solutions more manufacturable, by introducing more realistic modelling hypothesis, in this work the glued interfaces between pylon and engine were replaced by discrete assemblies: the latter can be considered as simple models of the hinged assemblies currently used on real operating aircraft.

In order to evaluate the impact of the load path on the Power Plant Structure and its performances, three different configurations of discrete assemblies were considered and compared.

Moreover, in order to evaluate the influence of two important design criteria, which are associated with the engine displacement, on the Power Plant Structure, two formulations were adopted for the optimization problem. The *Classic Formulation* aims to minimize

the compliance under a volume fraction constraint while in the *Complete Formulation* two additional constraints were added: one to limit the *Thrust Specific Fuel Consumption* variation caused by tip clearance degradation and one to control the loads on the blades of the Outlet Guide Vane. A *Pareto Front* will be performed for each design criteria.

This work provides a deep understanding about the *cowl load sharing* for the Power Plant Structure and a better knowledge concerning the impact of some design criteria on the optimal solution.

0.4 Overview

This final report is structured as follows:

- Chapter 1 introduces the UHBP Fan and the problems deriving by its integration into commercial aircraft;
- Chapter 2 introduces the Structural Optimization methods;
- Chapter 3 presents the Power Plant Structure and the Design Criteria which were considered in the present work;
- Chapter 4 illustrates the Free Size problem formulation and its results;
- Chapter 5 concerns the Topology Optimization problem formulation and the modelling of the discrete assemblies as engine mounts;
- in chapter 6 the Topology Optimization results deriving from the *Classic Formulation problem* are presented for the three configurations of discrete assemblies;
- in chapter 7 the results of the Topology Optimization problem under the Complete Formulation are presented;
- Chapter 8 sums up the conclusions and illustrates the perspectives of this work.

Chapter 1

The Ultra High Bypass Ratio Turbofan

1.1 Turbofan Engines

There are good reasons for an engine to have a high compression pressure ratio and an elevated gas temperature at the turbine entry. However, if all the spare pressure that this generates at the exit of the engine is only used to accelerate the core airflow, the engine results to be noisy and does not provide the minimum Thrust Specific Fuel Consumption (TSFC) [Rolls-Royce 2005]. In order to have a better propulsive efficiency, it is preferable to give a bigger amount of airflow less acceleration. That is the concept behind the Turbofan engine. Compared to the turbojet, an additional low-pressure turbine is added downstream of the core turbine: that provides a fan with power in order to compress additional cold air outside the core of the engine through a bypass duct (fig. 1.1). With this concept, two new design parameters are introduced: the ByPass Ratio (BPR), that is to say the ratio between the cold airflow and the core airflow, and the Fan Pressure Ratio (FPR), that is the ratio of airflow pressure after and before the fan stage. So, a turbofan engine gets its thrust by accelerating a larger mass of air to a modest jet velocity and it is the most used engine in current large commercial aircraft.

1.2 Promises of the UHBR Turbofan

The direction of turbofan technology has been moving toward higher BPR and lower FPR because that results in a reduction of the burnt fuel for a certain amount of obtained thrust (*Thrust Specific Fuel Consumption* - TSFC). That is evident in fig.1.2, where the red discontinuous curve represents the theoretical trend of TSFC depending on BPR: it is possible to remark that a greater BPR should allow an increase of the propulsive efficiency [C.E. Hughes 2013]. That is why the *Open Rotor Concept*, which is the engine concept

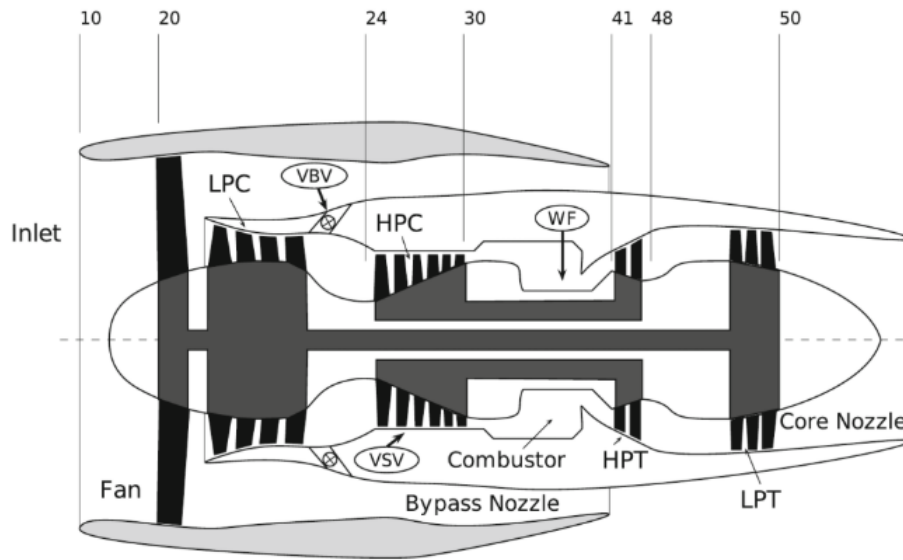


Figure 1.1: Turbofan cut section - source:[Richter 2011]

which allows the highest BPR value (between 40 and 80) has received a great interest by researchers [E.S. Hendricks 2012].

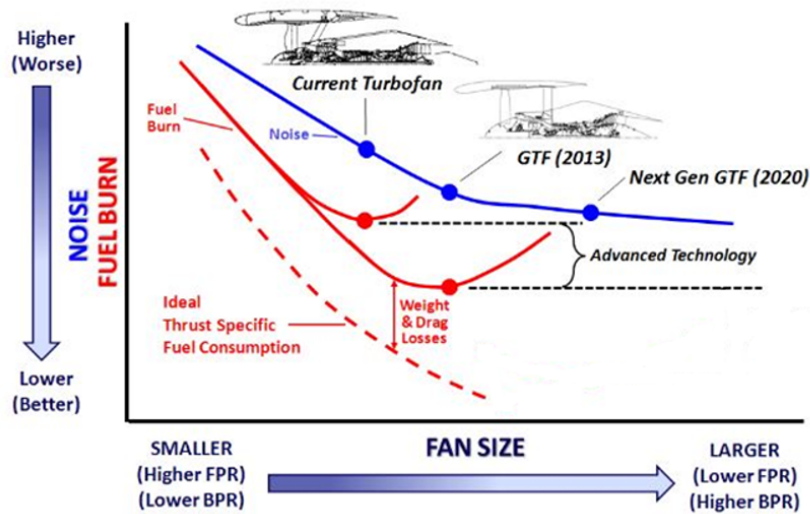


Figure 1.2: Effect of fan BPR on fuel burn - source:[C.E. Hughes 2013]

1.3 Challenges of the UHBR Turbofan

Despite its potential, the UHBR Turbofan provides also some challenges that need to be solved in order to make its integration into commercial aircraft possible, easier and efficient. Below some of these issues are briefly presented.

1.3.1 Fuel consumption minimum point

As before stated, a greater BPR should theoretically always allow a reduction of fuel consumption (red discontinuous curve in fig.1.2). However, it also implies an increase of the engine dimensions. In fact, higher BPR are made possible only by a bigger fan diameter: that also implies a larger engine nacelle, creating additional drag and inertial loads that have to be compensated by additional fuel consumption ([C.E. Hughes 2013]) in order to obtain the desired thrust. That is the reason why, beyond a certain BPR value, the negative effect of the additional drag and weight overcomes the beneficial effects of having an increased BPR (continuous red curve in fig. 1.2). However, researchers are currently engaged in the study of advanced technology whose integration could allow the delay of such a minimum point on the continuous red curve.

1.3.2 Core components dimensions

Weight and drag losses are not the only challenge imposed by an Ultra High By Pass Ratio. In fact, in order to reduce noise, the FPR is maintained as low as possible: that means that the fan rotational speed is limited. Since in the direct drive engine the fan is driven by the same shaft of the lower pressure compressor (LPC) and turbine (LPT), their rotational speed is limited too. Consequently, in order to produce the same amount of power and thrust, core components should have bigger dimensions, which means more weight and more burn fuel. The Geared Turbofan Technology is studied in order to face this problem and to allow a BPR of about 18. Of course, the drawback of such a technology is the increase in architectural complexity [James Denman 2011].

1.3.3 Aerodynamic issues

Since high BPR need to match lower FPR in order to keep the optimum power distribution ratio between the bypass and core engine, it would be more difficult to maintain fan stability margin. To overcome this issue, the *Variable Pitch Fan* could be considered as a smart and elegant solution [X. Yang 2018]: a gear system would allow to fit the fan pitch angle in order to adjust the incidence angle of fan blades and to stay inside the fan stability margin.

1.3.4 Deformations

Tip clearance change

In order to install such a great engine by minimizing the impact on aircraft performances, special Power Plant Structure designs are needed. In fact, a larger engine will be subjected to larger loads and eventually to larger deformations. Such deformations would require increased tip clearances, that is to say the gap between the engine casing and the tips of the spinning blades. Greater values of tip clearances would have disastrous consequences for fuel consumption. An industry rule-of-thumb equates a 0.25 mm increase in turbine tip clearance to an increase in engine exhaust gas temperature (EGT) of up to 10°C: that causes a reduction of turbine efficiency of up to 1% ([K.J. Melcher 2004]). Although the advantages deriving from tight tip clearances seem to be negligible, by taking into account an entire fleet, 160M\$ would be saved every year. Moreover, to limit the fuel consumption not only saves money but also the engine emissions are reduced. Tip clearance augmentation would increase also maintenance cost and would reduce life cycle of engine components. In fact, as clearances increase, the engine has to work harder to develop the same thrust and, once an engine reaches its EGT limit, it must undergo maintenance operations. Moreover, the higher temperatures at which the engine has to work reduce, in an important way, its life cycle.

Tip clearance changes during flight and ground operations derive from the displacement and the deformation of both static and rotating components under several loads. During aircraft operations, loads can be divided into engine loads (thermal, centrifugal, internal pressure and thrust) and flight loads (inertial, aerodynamic and gyroscopic). While engine loads could induce both axisymmetric and asymmetric clearance variation, the flight load can cause only the asymmetric one (fig. 1.3, 1.4). In [S. Lattime 2002], the events that may occur during flight operations and their impact on the tip clearance are illustrated: tip clearance changes are the most likely to happen during transient conditions, like takeoff, maneuver, landing, etc. Many tip clearance control systems have been proposed so far. They can be divided into two approaches: the active clearance control (ACC) and the passive clearance control (PCC). The ACC systems began to be integrated into commercial aircraft in the 1970's and they used cold air from fan to cool the support flanges of High Pressure Turbine case, reducing the case diameters and, consequently, the tip clearance during the cruise conditions. In such a way, turbine clearances could be set differently for several operating points. On the other hand, the PPC allows the setting of the clearance depending on the most severe transient condition. That means that there would be an excessive tip clearance for the cruise phase of the flight. The PPC include also the use of a abrasible material on the intern surface of the casing: after severe engine displacements, this protective material coat is milled by the rotor blade tips inducing a tip clearances increase.

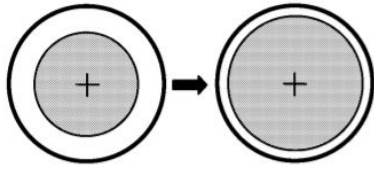


Figure 1.3: Axisymmetric clearance change - source [S. Lattime 2002]

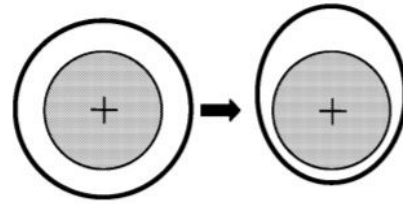


Figure 1.4: Asymmetric clearance change - source: [S. Lattime 2002]

Load on the blades of the Outlet Guide Vane

Another issue that could come up with the UHBR turbofan is an excessive load in the fan Outlet Guide Vane (OGV) blades. The OGV is an essential component that is placed downstream of the fan: its task is to reduce the swirl from the airflow coming from the fan and to connect the engine core structurally with the bypass duct and the engine mounts. That is why the OGV blades have to fulfill some specific aerodynamic requirements, like a low pressure loss [Clemen 2010]. As a consequence, their sizing can not undergo very important changes to withstand the higher amount of loads deriving from the UHBR fan integration. That is the reason why the loads on the OGV blades should be an additional criteria to take into consideration during the PPS optimization.

Since nacelle and pylon are both connected to the engine, their stiffness could have an impact on the engine displacements and, consequently, on tip clearance variation and OGV loads. That is why the research of an innovative PPS that could be able to control engine displacements is necessary in the context of UHBR integration.

Chapter 2

Structure Optimization

Most problems in structural optimization are formulated as constrained minimization problems. In a structural design problem, the objective function, as well as the optimization constraints function, are usually complex functions of the design variables and they can be determined only from an analysis on a finite element model of the structure.

2.1 Software Environment

In the present work, the following software were used:

- *Hypermesh* for the pre-processing tasks (mesh, boundary conditions, etc);
- *Optistruct* was used for the analysis and optimization process;
- *Hyperview and Hypergraph* were used for the post-processing.

2.2 Finite Element Method

Nowadays, in order to avoid or to reduce the cost that is associated with experimental tests, the numerical simulation has a key role in industrial applications. In particular, the *Finite Element Method* (FEM) is the most popular approximation method used to solve Partial Differential Equations. Thanks to this method, today it is possible to simulate numerically structures and fluid behaviour. The FEM is based on the approximation of the solution region by an assemblage of discrete elements [Kenneth H. Huebner 2001] where the unknown field variable is expressed in terms of approximating functions (fig.2.1). The latter are defined in terms of the values of the unknown field at the *nodal points*. So the nodal values of the unknown field become the only variables of the problem: field values

in other points are calculated by the approximation functions depending on nodal values. Of course, the precision of such an approximation depends on the finite element size (mesh size) and on the degree of the approximating functions. In order to find the unknown field nodal values, it is necessary to assemble the element properties: this means, for example, that for a stress analysis, it is necessary to find firstly each element stiffness and then to accomplish an assembly in order to determine the stiffness of the whole structure. That is done through the combination of the matrix equations expressing the behaviour of each element. The assembly phase allows to find a set of equations that have to be solved in order to find the unknown nodal field values. Before solving the equations, boundary conditions have to be imposed, like nodal loads or nodal known field variables. Once that done, the global system of equations can be solved to determine the nodal field values. Then, a phase of post-processing is generally performed.

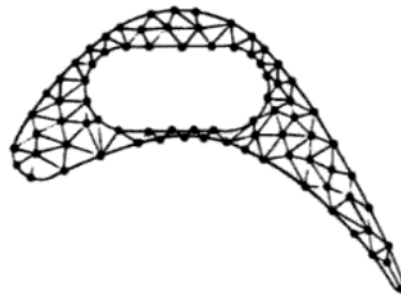


Figure 2.1: Finite Element Discretization - Mesh of a turbine blade - source [Kenneth H. Huebner 2001]

2.3 Optimal Solution Conditions

The basic structural optimization problem can be expressed in the following way:

$$\begin{aligned} \min_{\mathbf{x}} \quad & f(\mathbf{x}) \\ \text{s.t.} \quad & g_j(\mathbf{x}) \leq 0 \quad j = 1, \dots, n_g \end{aligned} \quad (2.1)$$

where n_g is the number of inequality constraints and \mathbf{x} is the vector of design variables. In the n_g inequality constraints, the *box-constraints* imposing lower and upper limits on the design variables have been included:

$$\underline{\mathbf{x}} \leq \mathbf{x} \leq \bar{\mathbf{x}} \quad (2.2)$$

In general, problem 2.1 has several local minima. The necessary conditions for a minimum of the constrained problem (2.1) are obtained by using the Lagrange multiplier method.

The Lagrangian function is defined as follows:

$$L(\mathbf{x}, \lambda) = f(\mathbf{x}) + \sum_{j=1}^{n_g} \lambda_j (g_j - t_j^2) \quad (2.3)$$

where λ_j is the j -th unknown Lagrange multipliers and t_j is the j -th slack variable which measures how far the g_j -th constraint is from being critical. A point \mathbf{x} is a local minimum of an inequality constrained problem only if a set of non-negative λ may be found such that the following equations are satisfied (Karush-Kuhn-Tucker conditions) ([Karush 1939], [H.W. Kuhn 1951]):

$$\begin{aligned} \frac{\partial L}{\partial x_i} &= \frac{\partial f}{\partial x_i} + \sum_{j=1}^{n_g} \lambda_j \frac{\partial g_j}{\partial x_i} = 0, & i &= 1, \dots, n \\ \frac{\partial L}{\partial \lambda_j} &= g_j - t_j^2 = 0, & j &= 1, \dots, n_g \\ \frac{\partial L}{\partial t_j} &= -2\lambda_j t_j = 0, & j &= 1, \dots, n_g. \end{aligned} \quad (2.4)$$

It is possible to notice that the last equation in 2.4 implies that when an inequality constraint is not critical (so that the corresponding slack variables is not zero) then the Lagrangian multiplier associated with the constraint is zero.

In order to find the solution \mathbf{x} which satisfies the necessary conditions in 2.4, different methods exist. For optimization problems as the ones that are considered in this work, where the number of design variables is larger than the number of constraints, gradient-based optimization methods are the most efficient. In *Optistruct*, optimization problems are solved through the *Convex Linearization Method* (CONLIN).

2.4 CONLIN method

The Convex Linearization Method is an extension to the approximation concepts approach ([L.A. Schmit 1974], [L.A. Schmit 1976], [L.A.Schmit 1976], [L.A.Schmit 1978]). According to these concepts, the size optimization problem was approximated by a sequence of sub-problems with a simple algebraic structure. Such sub-problems were obtained through the Taylor series expansion of the objective and constraints function with respect to intermediate linearization variables. Before the introduction of the CONLIN method, the explicit sub-problem was generally obtained by linearizing the objective function in terms of the direct design variables while the linearization of the constraints was performed with respect to the reciprocal variables. The evident reason for the success of this approximation method is that stress and displacements are exact linear functions of the reciprocal sizing design variables if the structure is in static equilibrium. So the basic structural optimization problem 2.1 would have been approximated like follows:

$$\begin{aligned} \min_{\mathbf{x}} \quad & f(\mathbf{x}) \simeq f(x^0) + \sum_{i=1}^n \frac{\partial f}{\partial x_i} (x_i - x_i^0) \\ \text{s.t.} \quad & s_j(\mathbf{x}) \simeq \sum_{i=1}^n \left(\frac{\partial s_j}{\partial (1/x_i)} \right)_{x^0} \left(\frac{1}{x_i} - \frac{1}{x_i^0} \right) \leq 0 \quad j = 1, \dots, n_s \end{aligned} \quad (2.5)$$

The approximation approaches got a lot of interest by researchers since they replace the primary optimization problem with a sequence of separable sub-problems that can be efficiently solved by the dual method approach. However, this approximation method showed some issues when, for fabricational reasons, it seemed useful to link the design variables also through linear inequality constraints so that problem 2.5 becomes like follows:

$$\begin{aligned} \min_{\mathbf{x}} \quad & f(\mathbf{x}) \simeq f(x^0) + \sum_{i=1}^n \frac{\partial f}{\partial x_i}(x_i - x_i^0) \\ \text{s.t.} \quad & s_j(\mathbf{x}) \simeq \sum_{i=1}^n \left(\frac{\partial s_j}{\partial(1/x_i)} \right)_{x^0} \left(\frac{1}{x_i} - \frac{1}{x_i^0} \right) \leq 0 \quad j = 1, \dots, n_s \\ & d_k(\mathbf{x}) \simeq \sum_{i=1}^n \left(\frac{\partial d_k}{\partial x_i} \right)_{x^0} (x_i - x_i^0) \leq 0 \quad k = 1, \dots, n_k \end{aligned} \quad (2.6)$$

Such a problem was not easy to solve since, even if it was separable, it was not convex [C. Fleury 1982]. At this stage, the Convex Linearization Method (CONLIN) was introduced by [C. Fleury 1986]. The CONLIN method is based on a hybrid approximation: in fact, each function (both objective and constraints) of the optimization problem is linearized with respect to mixed variables, either direct or reciprocal. More specifically, each function h which is involved in the optimization problem is approximated according to the following hybrid linearization:

$$h_j(x) \simeq h_j(x^0) + \sum_{+} \left(\frac{\partial h_j}{\partial x_i} \right)_{x^0} (x_i - x_i^0) + \sum_{-} \left(\frac{\partial h_j}{\partial(1/x_i)} \right)_{x^0} \left(\frac{1}{x_i} - \frac{1}{x_i^0} \right) \quad (2.7)$$

where the symbol \sum_{+} (\sum_{-}) means "summation over the terms for which $\frac{\partial h_j}{\partial x_i}$ is positive (negative)". Taking advantage of the following equality

$$\frac{\partial h_j}{\partial(1/x_i)} = -x_i^2 \frac{\partial h_j}{\partial x_i}, \quad (2.8)$$

equation 2.7 becomes like follows:

$$h_j(x) \simeq h_j(x^0) + \sum_{+} \left(\frac{\partial h_j}{\partial x_i} \right)_{x^0} (x_i - x_i^0) + \sum_{-} \left(\frac{\partial h_j}{\partial x_i} \right)_{x^0} \frac{x_i^0}{x_i} (x_i - x_i^0). \quad (2.9)$$

The attractive property of 2.9 is that each function is approximated with a convex function. Moreover, the convex linearization also yields the most conservative approximation among all the possible combinations of direct/reciprocal variables. This means that the approximations of the objective function and of the constraint functions tend to overestimate the values of the true functions. This implies that the approximated feasible domain for the optimization solution is generally inside the true feasible domain. As a consequence, the CONLIN method tends to generate a sequence of steadily improving feasible designs. Then, applying the CONLIN method, the primary optimization problem 2.1 is approximated as follows:

$$\begin{aligned} \min_{\mathbf{x}} \quad & f(x^0) + \sum_{+} f_i(x^0)(x_i - x_i^0) + \sum_{-} f_i(x^0) \frac{x_i^0}{x_i} (x_i - x_i^0) \\ \text{s.t.} \quad & g_j(x_0) + \sum_{+} g_{ji}(x^0)(x_i - x_i^0) + \sum_{-} g_{ji}(x_0) \frac{x_i^0}{x_i} (x_i - x_i^0) \leq 0 \quad j = 1, \dots, n_g \end{aligned} \quad (2.10)$$

where $f_i = \frac{\partial f}{\partial x_i}$ and $g_{ji} = \frac{\partial g_j}{\partial x_i}$. Since the CONLIN method approximates the primary optimization problem with a convex and separable one, it can be efficiently solved by the Dual Method Approach.

2.5 Dual Method Approach

Since the approximated problem deriving from the CONLIN method application is convex and separable, it can be efficiently solved by dual methods of mathematical programming. The dual method approach is a well known method in the mathematical programming community (ref. [Wolfe 1963], [Falk 1967], [Lasdon 1970], [Lootsma 1989]). Then [L.A. Schmit 1980], [C.Fleury 1979]) introduced such a method for the structural optimization. According to the dual method, the solution of the optimization problem 2.10 can be found by a *Max-Min* two-phase procedure:

$$\max_{\lambda} \quad l(\lambda) \quad (2.11)$$

$$\lambda \geq 0$$

The $l(\lambda)$ in 2.11 is the dual function resulting from the minimization of the Lagrangian function for the primary approximated problem 2.10:

$$l(\lambda) = \min_{\mathbf{x} \leq \mathbf{x} \leq \bar{\mathbf{x}}} L(x, \lambda) \quad (2.12)$$

$$L(x, \lambda) = f(x^0) + \sum_{+} f_i(x^0)(x_i - x_i^0) + \sum_{-} f_i(x^0) \frac{x_i^0}{x_i} (x_i - x_i^0) +$$

$$+ \sum_j \left(\lambda_j (g_j(x_0) + \sum_{+} g_{ji}(x^0)(x_i - x_i^0) + \sum_{-} g_{ji}(x_0) \frac{x_i^0}{x_i} (x_i - x_i^0)) \right) \quad (2.13)$$

Since the approximated primary problem 2.10 is separable, the Lagrangian function 2.13 can be written as the sum of n function $L_i(x_i)$: as a consequence, the n -dimensional minimization problem 2.12 can be divided into n single variable minimization problems. From the solution of this n simple minimization problems, the design variables \mathbf{x} are obtained in terms of the Lagrangian multipliers. Knowing $x_i(\lambda)$ the dual problem 2.11 is explicitly defined.

The only constraints of the maximization dual problem concern the non-negativity of the Lagrangian multipliers. As a result, since the dual maximization problem is a quasi-unconstrained problem, the initial implementation of CONLIN was based on the DUAL-2 method which is a Newton-type algorithm ([C. Fleury 1986]). In order to use a Newton-type method to solve the maximization problem, the first derivative of the dual function

$l(\lambda)$ is necessary as well as its Hessian matrix. For dual approaches the first derivatives of the dual function are easy to compute since they correspond to the constraints of the primary optimization problem. On the other hand the Hessian matrix introduces some discontinuity when the design variable reach their limit values ($\underline{\mathbf{x}}$, $\bar{\mathbf{x}}$). That causes some lack of reliability in the DUAL-2 optimizer since it breaks down when the Hessian matrix becomes singular. That is the reason why a more efficient optimizer was proposed by [Fleury 1989]: in the new method the Newton iteration used in the DUAL-2 optimizer is replaced by the resolution of an equivalent quadratic problem that can be solved by, for example, a conjugate gradient method with non-negativity constraints for the Lagrange multipliers. In such a way, the line search is abandoned and the Hessian matrix is allowed to be occasionally singular. Moreover, additional methods have been integrated to this optimizer in order to cope with the discontinuity of the second derivatives of the dual function. For further information, refer to the reference [Fleury 1989]. In Optistruct different arrest criteria could be employed: for example, the satisfaction of the conditions in 2.4 could be verified within a certain tolerance before arresting the iterations. Otherwise, a maximum number of iteration as well as the norm variation on the objective function between two consecutive iterations can be used as arrest criteria for the optimization process.

2.6 Free Size Optimization

Free Size Optimization method was used in this project in order to investigate the potential beneficial impact of IFS on tip clearance control. For this type of structural optimization, the structure topology and shape are fixed and only structure dimensions are optimized. In our project, the Free Size Optimization was used in order to optimize the thickness values t_i of a 2D Design Space elements. As a result, a design variable t_i is associated to each element or to each layer of the element if it belongs to a laminate. So, problem 2.1 becomes as follows:

$$\begin{aligned} \min_{\mathbf{t}} \quad & f(\mathbf{t}, \mathbf{U}(\mathbf{t})) \\ \text{s.t.} \quad & g_j(\mathbf{x}) \leq 0 \quad j = 1, \dots, n_g \\ & \mathbf{l}_b \leq \mathbf{t} \leq \mathbf{u}_b \end{aligned} \tag{2.14}$$

where \mathbf{t} are the thickness values of Design Space elements, $\mathbf{U}(\mathbf{t})$ are the nodal displacements and \mathbf{l}_b and \mathbf{u}_b are the vectors of respectively the lower and the upper bounds for the design variables.

2.7 Topology Optimization

Topology optimization is the process of determining the optimal connectivity, shape and location of structures/voids in a given design space. That allows more freedom than *size* and *shape optimization* methods: while in *size optimization* only the dimensions of the structure elements are optimized and in *shape optimization* just their optimal positions is found, in *topology optimization* also the topology of the domain can change by introducing or removing holes. That is the reason why Topology Optimization got a lot of researchers' attention and in [Joshua D. Deaton 2013] it is possible to find some of its progresses. Moreover, topology optimization is no longer just a field of research but important applications in several industries benefited from it. In this context, topology optimization became an effective tool for lease-weight and performance design in aeronautics and aerospace engineering: in [Ji-Hong Zhu 2015] it is possible to discover one among the most important applications of topology optimization in this industry field.

2.7.1 Implicit Methods

The topology optimization methods can be divided in implicit and explicit approaches. In the explicit ones the structure is described explicitly by including geometry features. On the contrary in implicit methods the optimal structure is described implicitly. Between the latter, they are worth of being mentioned the SIMP approach, where the optimal structural topology is identified from a black-and-white pixel image, and the level-set approach. The level-set approach, introduced in [Sethian 1999] and [J.A. Sethian 2000], specifies a surface in an implicit form as an iso-surface of a scalar function. This representation of structure was combined with mathematical programming method for topology optimization in [M.Y Wang 2003] and different researchers devoted their studies to the resolution of some convergence problems derived from this approach ([M. Burger 2004],[G. Allaire 2005], [L. He 2007]). The category of implicit methods include also the so-called *Evolutionary Structural Optimization* (ESO) that consists in gradually removing a finite amount of material from the design domain depending on heuristic criteria. This method was proposed in [Y.M. Xie 1997] where only removal of material was allowed. Then, some versions of this approach where elements could both be introduced and removed (Bi-directional ESO) were introduced [O.M. Querin 1998]. Anyway, despite its achievements and progresses in topology optimization, ESO/BESO methods have faced criticism about their validity and their heuristic base ([M. Zhou 2001]),.

2.7.2 *Solid Isotropic Material with Penalization* (SIMP)

The most widely used methodologies for structural topology optimization are the density-based methods which include the Solid Isotropic Material with Penalization (SIMP). Find-

ing the optimal structure Ω_s in a given design space Ω through a density-based method consists in determining the distribution of a density scalar function ρ defined on the design space where ρ takes the value 1 in Ω_s and the value 0 in Ω/Ω_s . Then the general structural optimization problem 2.1 through a density-based method can be formulated as follows:

$$\begin{aligned} \min_{\rho} \quad & f(\rho) \\ \text{s.t.} \quad & \int_{\Omega} \rho dx \leq V^* \\ & \rho(x) = 0 \text{ or } 1, \forall x \in \Omega \end{aligned} \tag{2.15}$$

where V^* is the total volume bound. The topology optimization problem is usually discretized by dividing Ω into N finite elements and the density is approximated to be constant in each element. Then the discretized version of problem (2.15) is the following one:

$$\begin{aligned} \min_{\rho} \quad & f(\rho) \\ \text{s.t.} \quad & V = \sum_{i=1}^N \rho_i v_i \leq V^* \\ & \rho_i = 0 \text{ or } 1, i = 1, \dots, \dots, N \end{aligned} \tag{2.16}$$

where v_i is the volume of i^{th} element. In the precedent formulations of topology optimization problem, the density variable ρ is a binary variable as it could only be equal to 1 or 0. As stated in [Kohn 1986], it is known that the 0-1 continuous topology problem in (2.15) lacks solution because the set of feasible design is not closed. This is the reason why the original problem in (2.15) is usually modified in such a way that the new version has a solution. Then, the modified problem is discretized and solved. There are two main ways to obtain a well-posed problem from the original one:

- through *relaxation*, that consists into an enlargement of the set of the feasible solutions. The *Homogenization approach* introduced by [M.P. Bendsøe 1988] belongs to this category. This approach allows the density variables to take intermediate values between 0 and 1 by associating macroscopic density to a microscopic porous and periodic micro-structure. That means that the optimal solution is characterised by the presence of grey zones that correspond to perforated micro-structures. The manufacturability of this grey zones represent the main drawback of this approach;
- through *restriction*, that is to say to find the solution of the topology problem in a set of feasible solutions which is smaller than the original one but it makes the problem well-posed.

Moreover, problems (2.15) and (2.16) can not be solved through the robust gradient-based methods because of the binary nature of density variables. That is the reason why in the Simple Isotropic Material with Penalization method in [M.P.Bendsøe 1989], the binary density variable is replaced by a continuous variable allowed to take all values from 0 to

1 while penalizing the intermediate density. The discretized SIMP optimization problem can be written as follows:

$$\begin{aligned} \min_{\rho} \quad & f(\rho) \\ \text{s.t.} \quad & V = \sum_{i=1}^N \rho_i v_i \leq V \\ & 0 < \rho_{min} \leq \rho_i \leq 1, i = 1, \dots, N \end{aligned} \quad (2.17)$$

The lower bound ρ_{min} is introduced in order to prevent singularity of the equilibrium problem. In the SIMP method, the stiffness of each element depends on the *p-power* of its density:

$$K_i(\rho) = \sum_{i=1}^N \rho_i^p K \quad (2.18)$$

where K is the element stiffness matrix and p is the imposed penalization. By imposing a value of p higher than 1, the local stiffness is lowered if the element density ρ_i is lower than 1. By this way the penalization makes inefficient to have intermediate densities in the optimal design. As the penalization increases, the continuous design variables are forced towards a black and white (0/1) solution with its ill-posedness. Then, the SIMP method is very efficient to avoid integer programming techniques but it does not make the optimization problem *well-posed*. For this reason, several methods had to be developed to solve the numerical instabilities deriving when structural topology optimization is solved by SIMP method.

2.7.3 Numerical instabilities using SIMP approach

As stated in [O. Sigmund 1998], numerical instabilities occurring in topological optimization can be divided into three categories:

- *Mesh dependence*, that is to say the problem of having important qualitative changes in the optimal solution when using a different mesh;
- *Checkerboards*, that refers to the problem that optimal solution often has regions which alternate solid and void elements ordered in a checkerboard style;
- *Local minima*, that refers to the problem of obtaining very different optimal solutions after little changes in optimization parameters.

Reference [O. Sigmund 1998] indicates the most effective tools allowing to avoid or moderate these numerical instabilities: these are summarized in the following paragraphs.

Mesh dependence

When refining the design space mesh, a better finite element modelling of the same optimal structure should be expected rather than a qualitatively different optimal solution. Nevertheless, dissimilar topologies could be obtained after re-meshing of the Design Space. This problem is referred as *mesh-dependence* and it is caused by the non-existence of a solution in the original continuous topology problem (2.15). In order to prevent this problem, the existence of a solution should be guaranteed. This could be done through a *relaxation* or *restriction* method. The *restriction* methods aim to impose a global or local constraint on the density variation. Here the main restriction methods that have been proposed and implemented by researchers:

- *Perimeter control.* This method was introduced by [L. Ambrosio 1993] and its first numerical implementation was done in [R.B. Haber 1996]. The perimeter of the structure Ω_s is constituted by the sum of holes contours and outer boundaries. The perimeter control restriction method consists of imposing an upper limit to the perimeter of Ω_s in order to restrict the domain of feasible solutions:

$$\int_{\Omega} |\Delta\rho| dx < P^*. \quad (2.19)$$

For the discretized problem, this global constraint is reformulated as follows:

$$\sum_{k=1}^K l_k \sqrt{\langle \rho \rangle_k^2 + \varepsilon^2} - \varepsilon < P^* \quad (2.20)$$

where $\langle \rho \rangle$ is the jump of material density through the k interface and K is the number of interfaces in the current solution. The parameter ε assures the differentiability of the constraint. Nevertheless, as it is a global constraint, the perimeter control scheme does not prevent the presence of tiny members in the optimal structure. Furthermore, this scheme implies the introduction of a new constraint that could deteriorate the convergence of the problem.

- *Global gradient constraint.* This scheme, as the following ones, can be used just when ρ has been relaxed to be a continuous variable. It involves the introduction of the following new global constraint:

$$\left(\int_{\Omega} (\rho^2 + |\Delta\rho|^2) dx \right)^{\frac{1}{2}} \leq M. \quad (2.21)$$

Proof of the solution existence after introducing this global constraint was given by [Bendsøe 1995] but the lack of numerical experiments using this *restriction* scheme induced researchers to prefer the *perimeter control* scheme rather than this one.

- *Local gradient constraint.* This scheme implies the introduction of the following $2N$ additional local constraints where N is the number of the elements in the design space:

$$\left| \frac{\partial \rho}{\partial x_i} \right| < c (i = 1, 2) \quad (2.22)$$

This scheme was firstly applied in [Niordson 1983a] for the thickness variation of plates while [Niordson 1983b] proved the existence and the FE-convergence of the solution. This method is very efficient to reduce the *mesh dependence* of the optimal solution but it is considered impractical for most topology optimization because of its higher computational cost.

- *Mesh independent filtering.* This scheme modifies the design sensitivity of a specific element based on a weighted average of the element sensitivities in a fixed neighborhood. This method was firstly proposed by [Sigmund 1994],[Sigmund 1997] and it has been proven to be very efficient to make solution more mesh-independent without adding further constraints. Its only drawback is that it is totally heuristic.

Checkerboard pattern

The checkerboard layout of material is one of the numerical instability that can occur during a topology optimization. The checkerboard problem is illustrated in fig. 2.2.b and it consists of regions in the optimal topology where elements and voids are disposed in a *checkerboard fashion*. This problem is due to the non-convergence of the finite element solution ([A.R. Diaz 1995],[C.S. Jog 1996]). Some prevention techniques could be adopted in order to avoid this phenomenon:

- *Smoothing* of the output picture by ignoring the problem that caused the checkerboard pattern;
- Several researchers proposed the use of *higher order finite elements* ([A.R. Diaz 1995],[C.S. Jog 1996]) or of *non conform finite elements* ([GW. Jang 2003]) in order to avoid checkerboard patterns;
- Also the aforementioned *restriction methods* used to avoid *mesh dependence* problems, i.e. *filtering* or *global and local variation constraints*, help to avoid the occurrence of checkerboard patterns;
- A convolution integral factor was proposed by [K.T Zuo 2007].

Local minima

Topology optimization problem are often non-convex, that is to say that they present several stationary solutions that are not necessarily close to the global minimum solution.

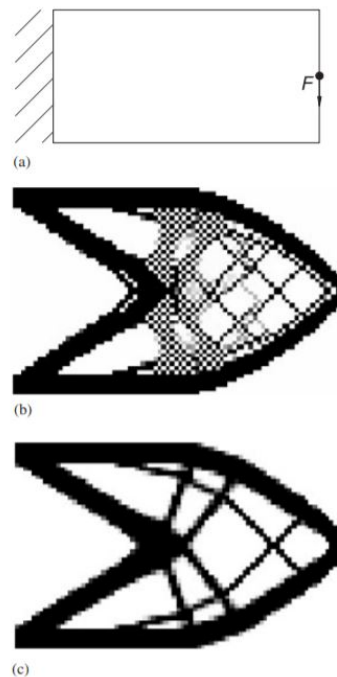


Figure 2.2: Optimized result of a cantilever beam (a) with (b) and without (c) checkerboard pattern (source [GW. Jang 2003])

As stated in [O. Sigmund 1998], the schemes used to produce a well-posed optimization problem tend to convexify it. That is why *continuation* methods can be applied in order to get an optimal solution closer to the global optimum. The continuation method consists of gradually modify the optimization problem from a convex artificial one to the original one in a finite number of steps. Different type of *ad-hoc* continuation methods have been developed. Between them, the continuation method proposed in [G. Allaire 1993] allows the presence of grey elements at first while introducing gradually the penalization scheme in order to finally obtain a *black and white* layout. A continuation method can be applied even to the perimeter constraint ([R.B. Haber 1996]) or the *mesh independence* filter ([Sigmund 1997]).

Implicit Methods Disadvantages

As before mentioned, the topology optimization implicit methods optimize the distribution of material in the design space describing the structure in an **implicit** way. For example in the SIMP method, structural boundary can only be extracted from a binary image while in the level set approach it has to be determined by calculating the contour lines of the level function through some interpolation techniques. Although topology optimization has done remarkable achievements through the implicit methods, there are still some problems

associated with the implicit solution approach that are worth of attention.

- Design engineers are supposed to translate the results obtained by topological optimization into one or more computer-aided-design (CAD) architecture to be further evaluated. In the density-based methods, structural boundaries can only be *extracted* from a pixel-based image. In this case, intermediate densities have to be threshold to black and white design, leading to a loss in the performance compared to the optimal solution. In the level-set approach, some interpolation techniques are required to approximate the contour line of the level function. Consequently, it is not easy to establish a direct link between the solution obtained by an implicit topology optimization method and the CAD modeling systems, where the geometries/topologies of structures are usually described explicitly by geometric primitives and by Boolean operations between them.
- In implicit approach, like the density-based methods or the level-set method, a large number of design variables is needed, especially for 3D problems, in order to describe the topology of a optimized solution. That results in an important computational cost.
- Since no geometry information is embedded in the optimized solution obtained by implicit methods, it is not straightforward to control the structural features of the optimized solution (i.e. minimum length scale, minimum curvature, etc.) even if great progresses have being reached by researchers [J. Liu 2016]

2.7.4 Explicit Methods

All the lacks in implicit approaches can justify the attempts of doing topology optimization through a more explicit representation of the structural topology by incorporating geometric features. Between the explicit approaches that can be found in the literature, the following ones achieved some remarkable results: the *Method of Moving Morphable Componenets* (MMC) with the use of ersats material model or the extended final element method (XFEM), the *Geometry Projection* (GP) method and the *Moving Node Approach* (MNA).

The MMC method was introduced by [Guo X. 2014] where rectangular structural components were used as primary building blocks of the topology optimization. The optimal structural topology can be obtained by determining the geometry characteristic parameters, the orientation as well as the connectivity of these components. Through the overlapping of the components, the structure topology is optimized. For the structural analysis, the background finite element mesh is fixed and the extended finite element method (XFEM) introduced by [Wei P. 2009] is adopted. In XFEM, the stiffness matrix is build by remeshing the elements cut by component boundaries in order to take into account the distribution of

material in these elements while the total number of the degrees of freedom is unchanged during the optimization process. In [X. Guo 2016] curved shape components are introduced. [W. Zhang 2016] introduced a minimum length scale control by imposing a lower bound to the minimum dimension of each component and to their intersection. In [W. Zhang 2017a] 3D topology optimization was performed through MMC by using cuboid-like structural components. Moreover, in this last work, XFEM method for the structural analysis was replaced by the ersatz model material in order to enhance the computation efficiency. In [W. Zhang 2017b], B-spline curves are used to describe the boundaries of moving morphable components (MMC) or moving morphable voids (MMV) and some techniques are developed in order to avoid the self-intersection of splines and to preserve the smoothness of structural boundaries when topological changes occur. In [W. Zhang 2018] the MMV method was used to solve a stress-constrained topology problem through an adaptive FE mesh in order to guarantee sufficient accuracy in the stress computation and in the optimal topological layout. Finally in [X. Lei 2019] the MMC framework is used to obtain a training data set to be used through Machine Learning techniques in order to achieve real-time structural topology optimizations.

The GP was initially introduced by [J. Norato 2004] for shape optimization but then it was adapted for explicit topology optimization methods. GP method consists of a filtering technique to project the design geometry onto the fixed FE analysis domain. By this method, the indicator function that describes the structures layout is filtered to obtain a volume fraction distribution. As the filter can be differentiable, the robust gradient-based optimizer can be used to solve the topology optimization. In [J. Norato 2015] the GP was applied for the explicit topology optimization by using round-ended bars as structural blocks. In [S. Zhang 2016] Geometry projection approach was implemented for 3D solid structures composed of rectangular plates obtaining one of the best performance provided by explicit approaches. Further improvements of GP were achieved by [S. Zhang 2016] where this method was implemented in order to solve a stress-constrained explicit topology optimization and in [H. Kazemi 2018] and [H. Kazemi 2020] where multi-material design was treated.

The MNA was proposed by [Overvelde 2012]. In this method, the building blocks are defined by mass nodes with the aim of reducing the design variables and the number of degrees of freedom.

Finally, in [Coniglio 2019] a Generalized Geometry Projection (**GGP**) was introduced in order to solve explicitly topological optimization problems. All the aforementioned methods can be considered as a particular case of GGP.

Anyway, despite their achievements and improved performances, explicit methods are not sufficiently mature to be implemented in commercial software but they represent an important research field for future applications. The SIMP method remains the most popular method currently implemented in commercial software like *OptiStruct*.

2.8 Objective and constraint aggregations

Optimization problems often need to fulfill several constraints. An high number of constraints could affect the optimization process that would become more computationally expensive. A straight forward way to reduce the constraints number is to ensure that the maximum constraint is fulfilled, replacing all the constraints by:

$$G_{max} = \max(g_1, g_2, \dots, g_{n_g}) \leq 0 \quad (2.23)$$

However, the max function is not differentiable, which is not convenient for gradient-based optimization methods. That is the reason why several aggregation methods were suggested in the literature in order to approximate the max function. In *Optistruct* the *p-aggregation* method is used where the max function is approximated as follows [P. Duysinx 1998]:

$$\max(g_1, g_2, \dots, g_{n_g}) \simeq \pi(g_i, p) = \left(\sum_{i=1}^{n_g} g_i^p \right)^{\frac{1}{p}} \quad (2.24)$$

The p factor is an index of the approximation quality: an higher value allows a better approximation of the max function but it could induce an higher computational cost. In this work, p has been imposed to be equal to 4.

Nevertheless, the *p-aggregation* is only one of the possible aggregations methods. The Kresselmeier-Steinhauser function, for example, ([G. Kreisselmeier 1980]) is between the most acknowledged ones:

$$\max(g_1, g_2, \dots, g_{n_g}) \simeq \frac{1}{P} \ln \left(\frac{1}{n_g} \sum_{j=1}^{n_g} e^{Pg_j} \right) \quad (2.25)$$

Also the Kresselmeier-Steinhauser function tends to the real value of the max function if $P \rightarrow +\infty$.

These aggregation approaches are also used to aggregate objectives and constraints functions that are load case or model (for multi-model optimization) dependent.

2.9 Convergence Criteria

In *Optistruct* two convergence tests are used and the satisfaction of only one is required so that the solution is considered as converged:

- the *Regular Convergence* is reached when the change in the objective function is less than the objective tolerance and the constraint violations are less than 1%;

- the *Soft Convergence* is achieved when there is little or no change in the design variables for two consecutive iterations.

In the following paragraphs, the convergence tolerance for each optimization process will be specified.

Chapter 3

Power Plant and Performance Modelling

3.1 Power Plant Structure

In current large commercial aircraft, engines are supported by pylons who are made up of a primary and a secondary structure. The first one aims to support the engine and to convey efforts from the propulsion system to the aircraft (fig.3.1 and 3.2). The secondary structure supports the aerodynamic surfaces and other fundamentals systems (fig.3.3). The engine is enclosed by the nacelle that contains also other important subsystems like electrical generators (fig.3.4). Moreover, the nacelle aims to be an aerodynamic fairing for the engine, to provide an appropriate air intake for the airflow, to support the Thrust Reverse Unit System (TRU) and to attenuate engine noise. The Power Plant Structure (PPS) is made up of the pylon and the nacelle.

The Thrust Reverser Unit is a braking aid system that reduces the landing distance and it is activated after the touchdown by the pilot. Its activation leads to a deviation of the secondary airflow that is returned forward of the nacelle (fig. 3.5). This creates a force backward, called reverse thrust, which contributes to the deceleration of the aircraft. The Thrust Reverser Unit is composed of several parts, including the Inner Fixed Structure (IFS) and the Outer Fixed Structure (OFS). These structures form a duct for the cold airflow. Two different architectures are possible for the Thrust Reverser Unit: the *C-Duct* and the *D-Duct*. The main difference between them is that in the D-Duct configuration a lower bifi connects the 6 o'clock TRU beams to the IFS (fig. 3.6) while they are not directly connected in the C-Duct configuration.

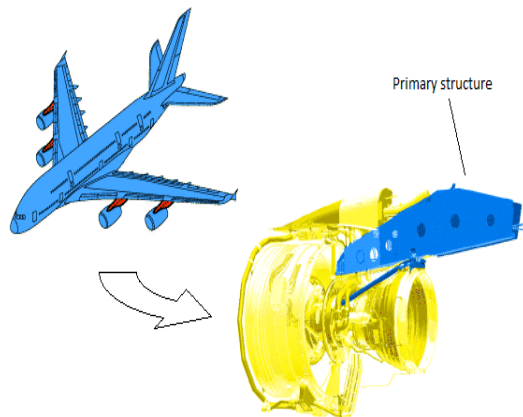


Figure 3.1: Pylon primary structure location - source: Airbus Internal Documents

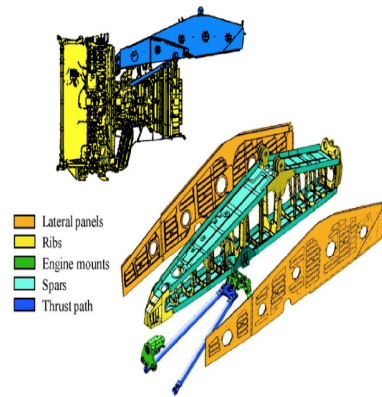


Figure 3.2: Pylon primary structure components - source: Airbus Internal Documents

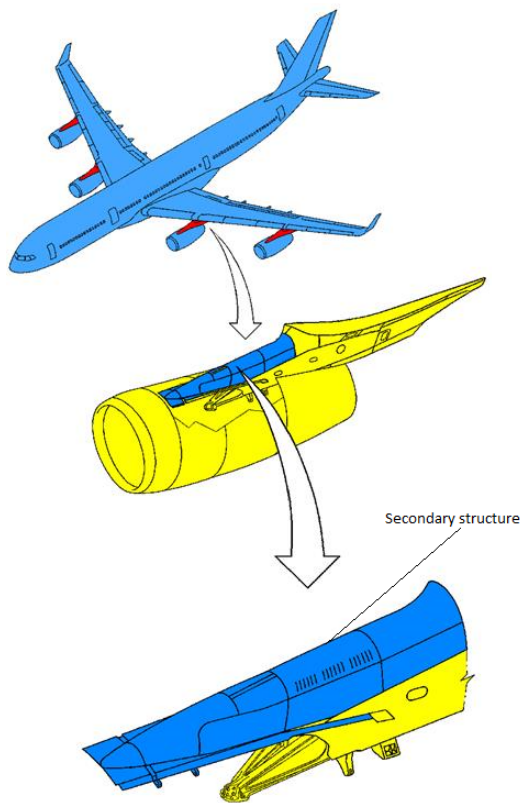


Figure 3.3: Pylon secondary structure location - source: Airbus Internal Documents - authors: CROS, SERRA, PERROT

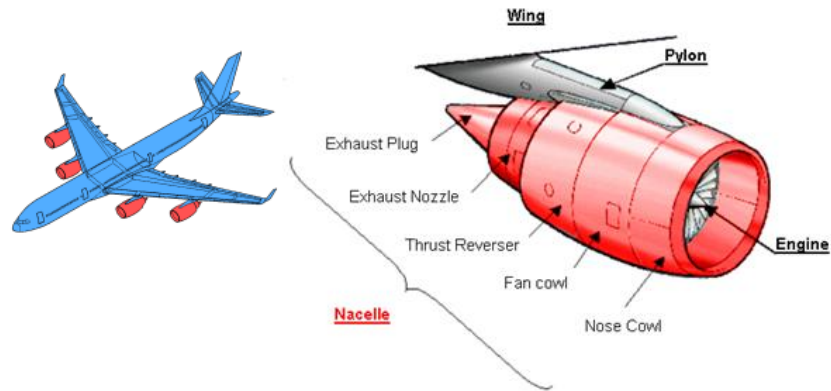


Figure 3.4: Location and description of the nacelle - source: Airbus Internal Documents - authors: CROS

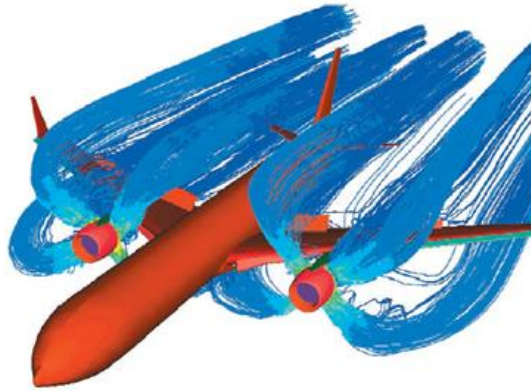


Figure 3.5: Airflow pattern with activated TRU - source: Airbus Internal Documents

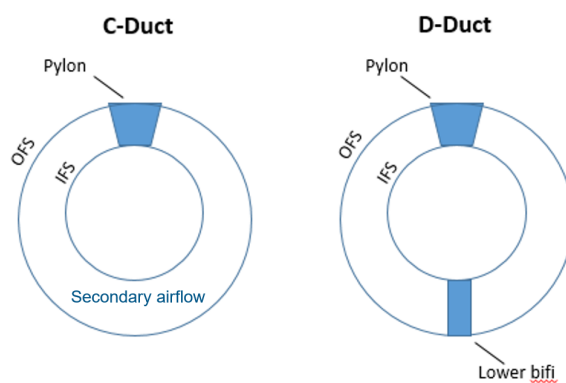


Figure 3.6: C-Duct and D-Duct diagram

3.2 State of art of the project and new objectives

The present project is the continuation of previous works accomplished at Airbus:

- The first key contribution was given by Simone Coniglio with his PHD Thesis "*Propulsion Airframe Topology Optimization with performance and stress criteria using Eulerian and Lagrangian Approaches*" (2016-2019) [Coniglio 2019]. In his work, Abaqus was used for the engine model while Matlab was used for the design zone model and topology optimization. During his thesis, the space to be optimized was the pylon primary structure. Tip clearances criteria were already included in the optimization process;
- The second contribute was given by Martin Vlashi's internship at Airbus. He optimized two different design spaces by using *Optistruct* software: a Small Design Space that was mainly made up of the pylon secondary structure and the upper bi-fi and a Large Design Space that included secondary structure, upper bi-fi, pylon, fan case, nacelle and lower bi-fi. Moreover, he introduced the Outlet Guide Vane blades (OGV) stress as design criteria in the optimization process;
- The third contribute was given by Gabriele Capasso [Capasso 2019] during his internship at Airbus. He optimized the Large Design Space (LDS) on an updated engine model by using *Optistruct* software. Moreover, he reduced the necessary number of optimization responses in order to accelerate the computational cost of the optimization process.

The aim of my internship was to undertake the work that had already been done and to try to go further. In order to move toward a light but stiff PPS architecture, this internship had three main objectives:

1. During the previous works, the stiffness of the Inner Fixed Structure of the Thrust Reverser Unit seemed to be beneficial to limit the TSFC increase caused by the tip clearance degradation. That is the reason why the first objective of the present work was to verify and quantify the potential impact of the IFS stiffness on the tip clearance control. For this purpose, a 20% increase in the IFS thickness has been supposed respect to the original model: the additional thickness distribution over the IFS has been optimized by Free Size Optimization in order to minimize the *TSFC* augmentation caused by the tip clearance variation. By comparing the resulting *TSFC* from the optimization respect to its value in the original model, the potential beneficial effect of the IFS stiffness on tip clearance control has been assessed. This optimization problem has been solved both for a *C-Duct* and a *D-Duct* configuration of the Thrust Reverser Unit in order to assess also the influence of the lower bifi on the *TSFC* increase caused by the tip clearance degradation.

2. The second goal of the present work was to resume the Topology Optimization on the Large Design Space (LDS) to improve the modelling hypothesis respect to the previous works. In fact, before this work the Large Design Space was supposed to be glued to the engine by making the model highly hyperstatic. Such a modelling hypothesis is far from being realistic since highly hyperstatic assemblies are not appropriate for the engine mounts since they don't support thermal expansions. That is the reason why, in order to make the Topology Optimization solutions more manufacturable, in this work the glued interfaces between pylon and engine were replaced by discrete assemblies: the latter can be considered as simple models of the hinged assemblies currently used on real-life operating aircraft.

The Topology Optimization was employed in order to obtain the most stiff Power Plant Structure under certain constraints (depending on the used formulation). In order to evaluate the impact of the load path in the Topology Optimization solution, three different configurations of discrete assemblies were modelled.

Moreover, the Free Body Diagram has been added to the post-processing of each Topology Optimization solution in order to better understand the load paths in the propulsive architecture.

3. The third objective of this work was to study the influence of the engine strain design criteria (TSFC deriving from tip clearance degradation and loads on the OGV blades) on the stiffest PPS solution. For this purpose, two additional constraints were added to the *Classic Formulation* of the Topology Optimization Problem and a *Pareto Front* has been done for each design criteria.

3.3 Tip Clearance Model

As already mentioned, the tip clearances control should be considered as a fundamental design criteria for the Power Plant Structure. The term *tip clearance* defines the gap between the engine casing and the rotor blades tips (fig. 3.7). In a cylindrical reference

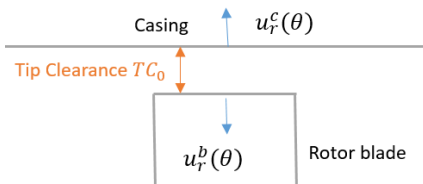


Figure 3.7: Radial displacement effect on tip clearances

system, the tip clearance can be defined as the sum of the initial tip clearance TC_0 and its

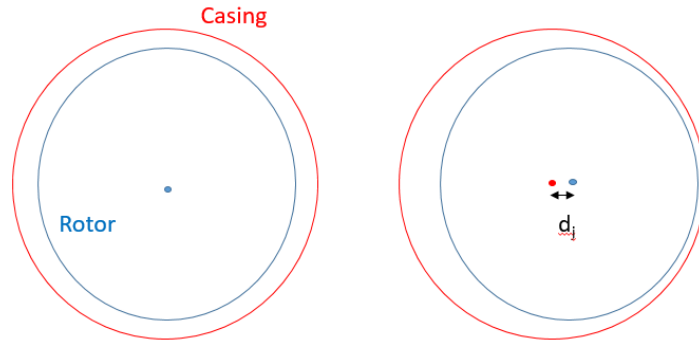


Figure 3.8: Relative displacement between the rotor shaft and the casing axis

variation due to the radial relative displacement of casing and rotor blade:

$$TC(\theta) = TC_0 + u_r^c(\theta) - u_r^b(\theta) \quad (3.1)$$

where $u_r^c(\theta)$ and $u_r^b(\theta)$ are the radial displacement respectively of the rotor and the blade tip. Tip clearance variation is mainly caused by three phenomenons during the engine running:

- the rotor shaft bending;
- the casing deformation;
- the centrifugal and thermal loads on rotor blades.

A useful approach in tip clearance computation is proposed in [M.B. Graf 1997] where clearance variation due to radial relative displacement is expressed in terms of Fourier series:

$$TC(\theta) = \sum_{i=0}^{\infty} c_i \cos(i\theta + \phi_i). \quad (3.2)$$

The c_1 term of the Fourier series represents the relative displacement of the rotor shaft respect to the casing axis (ref.3.8). Only this term was taken into consideration in the optimization processes of this work. In fact, to consider other terms would have been too computationally expensive. Moreover, the c_1 term is the most impacted by PPS properties while the other terms, like for example the ovalization of the casing, mainly depend on the casing local properties.

In order to compute the relative displacement between casing axis and shaft, the casing axis displacement has to be calculated. This is done by imposing the casing axis displacement equal to the average of displacement values at the nodes of the stator for the

considered stage. By this way, the relative displacement d_j between casing axis and rotor shaft at the j -th stage can be calculated as follows:

$$d_j = \sqrt{\left(\frac{1}{m_j} \sum_{l=1}^{m_j} v_{sjl} - v_{\alpha j}\right)^2 + \left(\frac{1}{m_j} \sum_{l=1}^{m_j} w_{sjl} - w_{\alpha j}\right)^2} \quad (3.3)$$

where

- m_j is the number of nodes of the stator at the stage j ;
- $v_{\alpha j}$ and $w_{\alpha j}$ are the two components of the transverse displacement for the shaft node at the j -th stage;
- v_{sjl} and w_{sjl} are the two components of the transverse displacement for the l -th node on the stator at the j -th stage.

In order to calculate the casing axis displacement to use in equation 3.3, an RBE3 element was created for each stage. An RBE3 element defines the motion at a reference grid point (slave) as the weighted average of the displacement values at other grid points (masters). In our model, all the master nodes have the same weight for the calculation of the slave displacement. For each stage, a slave node is created on the engine shaft at the exact x coordinate of the considered stage (fig 3.9), while the RBE master nodes are the nodes on the internal surface of the casing at the considered x -coordinate. In such a way, the motion of the slave node will be determined by the average displacement of the stator nodes.

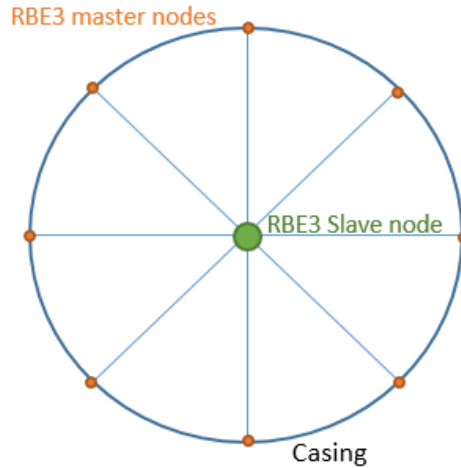


Figure 3.9: Diagram of RBE3 element for casing average displacement

In order to calculate the shaft rotor displacement for each stage, the displacements of the shaft nodes at the stage x -coordinate have to be requested. Once that done, in order to

compute the relative displacement between the casing axis and the rotor shaft at the j -th stage (equation 3.3), the following response should have been requested:

$$d_j = \sqrt{(v_{RBE3slavenode_j} - v_{shaft_j})^2 + (w_{RBE3slavenode_j} - w_{shaft_j})^2}. \quad (3.4)$$

This means that 5 responses had to be computed for each stage. In order to reduce the number of optimization responses, another node was added by [Capasso 2019] for each stage: its axial displacement and rotations were constrained while the other displacement components were imposed, through two MPC (Multipoint Constrain equation), as follows:

$$v_j = v_{RBE3slavenode_j} - v_{shaft_j} \quad (3.5)$$

$$w_j = w_{RBE3slavenode_j} - w_{shaft_j}. \quad (3.6)$$

By imposing as output response the displacement of this last node for each stage, the relative displacements between the casing axis and the rotor shaft can be directly obtained at every stage. What we would like to reduce is not the relative displacement d_j itself but the impact of all tip clearance variations on the engine performances like the fuel consumption. That is the reason why a simplified expression of the *Thrust Specific Fuel Consumption* (TSFC) had been defined in terms of the relative displacements d_j to be used in the optimization process:

$$TSFC = \sum_c^{n_c} \sum_s^{n_{cs}} \frac{d_{c,s} k_{c,s}}{L_{c,s}} \quad (3.7)$$

where:

- n_c is the number of components (Fan, Low Pressure Compressor (LPC), High Pressure compressor (HPC), High Pressure Turbine (HPT) and Low Pressure Turbine (LPT));
- $n_{c,s}$ is the number of stages for the c -th component;
- $d_{c,s}$ is the calculated relative displacement between the engine casing and the rotor shaft for the s stage;
- $k_{c,s}$ is a factor that takes into account the impact on TSFC depending on the considered stage;
- $L_{c,s}$ is the length of the blade at the considered stage.

The $k_{c,s}$ definition is domain of the engine manufacturers. Moreover, it is important to notice that the relative displacement for each stage has been normalized in 3.7 by the

length of the blades. In fact, stages can be very different between them: for example, the fan blade length could be 50 times the one of a compressor blade. That makes this normalization necessary in order to have a more realistic index of tip clearance influence on the *Thrust Specific Fuel Consumption*.

3.4 Outlet Guide Vane Moment Model

The importance of *Outlet Guide Vane* component has already been stated: it reduces the swirl from the airflow coming from the fan. In a UHBR turbofan, the OGV blades would have bigger length compared to the conventional turbofan. That could induce additional loads which, because of the OGV aerodynamic requirements, could not be compensated by an important resizing of the blades. That is the reason why it is necessary to take the loads in the OGV blades into account during the optimization of the Power Plant Structure in the context of the UHBR integration. However, a stress constrained optimization, like the one which was considered during Martin Vlashi's internship, would have been very computationally expensive. Since we are at a preliminary design phase, a stress constrained problem was not worth of being performed. That is the reason why the resulting load on all the OGV blades was employed as design criteria since Gabriele Capasso's work. More specifically, just the resulting bending moment is constrained for the topology optimization since it is the real critical load for the OGV blades.

In the FEM model, there are 40 OGV blades and each of them has 4 RBE3 elements at the interface with the fan case. In the original model (*baseline*), each RBE3 of the OGV blades was linked to an RBE3 element on the fan case by a rigid element. Nevertheless, in order to obtain the loads passing through the interface between OGV blades and fan case, and still trying not to demand many additional output responses, the set-up in the fig. 3.10 was introduced by [Capasso 2019]. In such architecture, the RBE3 elements of the

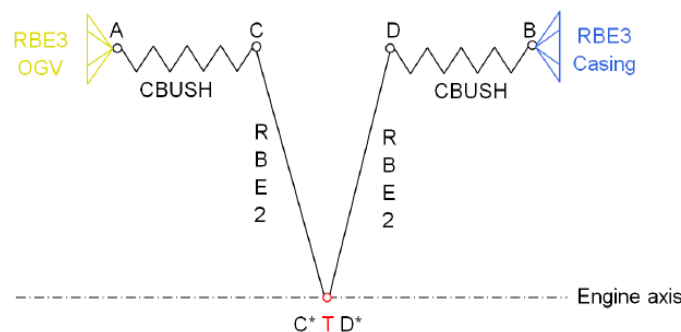


Figure 3.10: Model set-up between OGV blades and fan case - source: [Capasso 2019]

baseline are unchanged. Then, for each of them, two RBE2 elements link the node C to

Load Case ID	Configuration TRU	Category
1050	Stow	Fatigue
1052	Stow	Fatigue
1055	Stow	Fatigue
1056	Stow	Fatigue
2001	Stow	Limit
2004	Stow	Limit
2005	Stow	Limit
2007	Stow	Limit
2008	Stow	Limit
2009	Stow	Limit
2012	Stow	Limit
2014	Stow	Limit
2017	Stow	Limit
2018	Stow	Limit
2019	Stow	Limit
2040	Stow	Limit
1193	Reverse	Fatigue
2192	Reverse	Limit

Table 3.1: Load cases

C* and D to D*. In order to get the resulting loads, a node T was created and its motion was imposed equal to the relative displacement between C* and D* in all directions and for all the 160 OGV/casing interface nodes: that is done through several MPC equations. Since the node T is finally clamped, it is possible to obtain the resulting loads of the OGV by demanding just the loads on node T. From the component y and z of the moment at node T, the resulting bending moment is calculated.

Load Cases

In this work, both Limit Load Conditions and Fatigue Load Conditions have been taken into consideration. These load conditions are the combination of inertial and aerodynamic loads as well as distributed forces and moments deriving from the engine. Table 3.1 represents the load conditions that have been taken into consideration in this work.

Chapter 4

Free Size Optimization

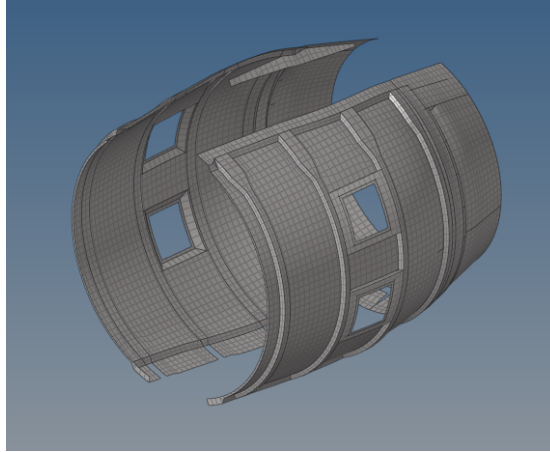
During the previous works, it seemed that the Inner Fixed Structure of the Thrust Reverser Unit could have a potential beneficial impact on the tip clearances variation. In order to verify that, the impact of a more stiff IFS with respect to the original model on the tip clearance control has been evaluated. More specifically, an increase by 20% of the IFS volume has been supposed respect to the original model (*baseline*): the distribution of the additional thickness has been optimized by Free Size Optimization (FS) in order to minimize the *TSCF* deriving from the tip clearance variation and see if it is reduced with respect to the original model.

4.1 FS Design Space

The *Inner Fixed Structure* of the Thrust Reverser Unit is the inner surface of the secondary flow duct (fig. 4.1). In the *baseline* model the IFS is connected to the pylon by four hinges by side, which are placed in correspondence with the vertical stiffeners of the IFS. The IFS is also connected forward to the torque box and it is latched at the bottom to the engine.

As result of the Free Size Optimization, a thickness value, inside an imposed range, will be associated to each element of the *Inner Fixed Structure*. Consequently, the design space of the performed Free Size Optimization is made up of the thickness range of the IFS elements.

The design space is made up of 12782 shell elements (*TRIA3* and *QUAD4*) whose thickness can change between their original value in the *baseline* up to 8 times that value in order to minimise the tip clearance impact on the *Thrust Specific Fuel Consumption*.

Figure 4.1: Inner Fixed Structure - *C-Duct* configuration

4.2 Free Size Optimization Problem

Beyond the *box-constraints* introducing the lower and the upper bounds for the Design Space elements, a volume constraint is added in order to limit the Design Space Volume to 1.2 times the original value. As a result, the Free Size Optimization allows us to know if the 20% more of the IFS volume, appropriately distributed, could induce any benefit for the tip clearances impact on TSFC. To sum up, the adopted formulation for the Free Size Optimization problem of the IFS elements is the following one:

$$\begin{cases} \min(\max_{i \in J_1} TSFC(\mathbf{U}(t))) \\ t_{k0} \leq t_k \leq 8t_{k0} \\ V_{IFS}(t) \leq 1.2V_{IFS_0} \end{cases} \quad \forall k \in T_k \quad (4.1)$$

where \mathbf{U} are the nodal displacements, t_k is the k -th element thickness of the IFS, t_{k0} is its original thickness in the baseline, T_k is the set of the IFS elements and J_1 are the fatigue load cases. In fact, since tip clearance variation is mainly due to the fatigue loads during transient conditions, limit load conditions are neglected for tip clearances control. Moreover, if an element belong to a composite laminate, a design variable is actually associated to each layer.

In order to limit the additional IFS volume to 20% of the original one, a constraint on the volume of the design space is also imposed: in 4.1 V_{IFS} is the current IFS volume and V_{IFS_0} is the IFS volume in the original model.

The Free Size Optimization has been performed for both the configurations of the Thrust Reverser Unit: the *C-Duct* configuration as well as the *D-Duct* model. For the latter, a lower bifi connects the *Outer Fixed Structure* and the *Inner Fixed Structure* (fig. 4.2). The lower bifi was supposed to be of the same material as the 6 o'clock Thrust

Reverser Unit beams. However, since the purpose of this study is to analyse the IFS impact on the TSFC, the lower bifi was not included into the Design Space. For this study,

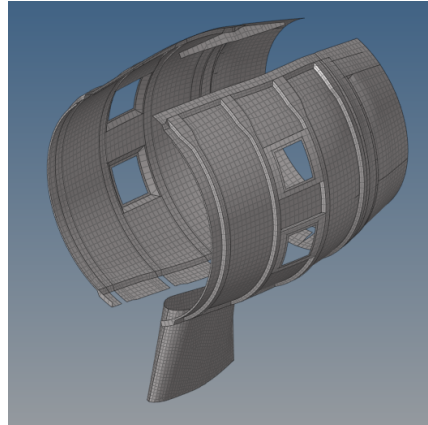


Figure 4.2: Inner Fixed Structure with lower bifi in the *D-Duct* configuration.

only the loads conditions with the *Thrust Reverser* in the stow configuration 3.1 have been taken into account.

As the *max* function in 4.1 is not a derivable function, a *p-aggregation* was used to approximate the maximum TSFC value between the fatigue load cases.

The optimization process stops if one of the following conditions is satisfied:

- The solution has converged, that means that the regular and/or the soft convergence criteria has been satisfied. For this purpose, the objective tolerance has been imposed equal to 0.0001. This means that the regular convergence would be satisfied if the relative change in the objective function between two design iterations is less than 0.0001.
- A maximum number of iterations, that in this case it is equal to 500, has been reached.

4.3 Free Size Optimization Results

In the original model, the components with the highest thickness values were the vertical stiffeners and the bottom part of the IFS. When the IFS is submitted to the Free Size optimization in 4.1, the thickness distribution that is shown in fig.4.3 has been obtained for the *C-Duct* configuration. It is possible to notice that the additional mass is placed on the vertical stiffeners near the hinges as well as at the interface with the torque box and on the bottom part of the Design Space. Also the horizontal stiffener which is placed between the first and the second vertical one, is thicker than in the original model.

For the *D-Duct* configuration, the same components as for the *C-Duct* receive the additional mass: the only difference is that stiffeners and torque box interface have their thickness lightly reduced compared to the *C-Duct* configuration while more elements of the bottom part, near the junction with the lower bifi (fig.4.4), are made thicker.

Fig. 4.5 shows the volume constraint evolution over the iterations for both the *C-Duct* and *D-Duct* configuration. It is possible to see that in both cases the volume constraint is active: that means that all the 20% of the additional volume respect to the baseline is used in order to minimize the TSFC. Moreover, it is possible to observe that, for both the configurations, the solution converged in less than 23 iterations since the *Regular Convergence* is reached.

Finally, fig. 4.6 shows the evolution of the objective function $\max_{i \in J_1} TSFC(\mathbf{U}(\mathbf{t}))$ during the optimization process for the *C-Duct* and the *D-Duct* configuration. Thanks to the additional volume which has been provided to the IFS, the *C-duct* configuration improved its *TSFC* performance associated with tip clearance degradation by 8% respect to the original model: this means that the *Inner Fixed Structure* could really have a beneficial impact for the tip clearance control.

By comparing the *C-duct* curve to the *D-duct* evolution, it is evident that also the presence of a lower bifi has a beneficial impact on the *TSFC* associated with the tip clearance variation. In fact, at iteration 0 the lower bifi introduction makes the *TSFC* decrease by 4% compared to the baseline. Moreover, a better gain is also obtained from the Free Size Optimization respect to *C-duct* configuration: at the final iteration, a TSFC reduction by 14% is obtained respect to iteration 0.



Figure 4.3: Thickness distribution as result of the FS optimization for the C-duct configuration

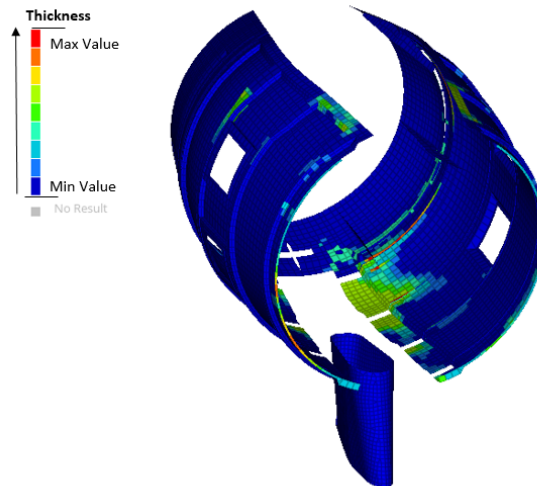


Figure 4.4: Thickness distribution as result of the FS optimization for the D-duct configuration

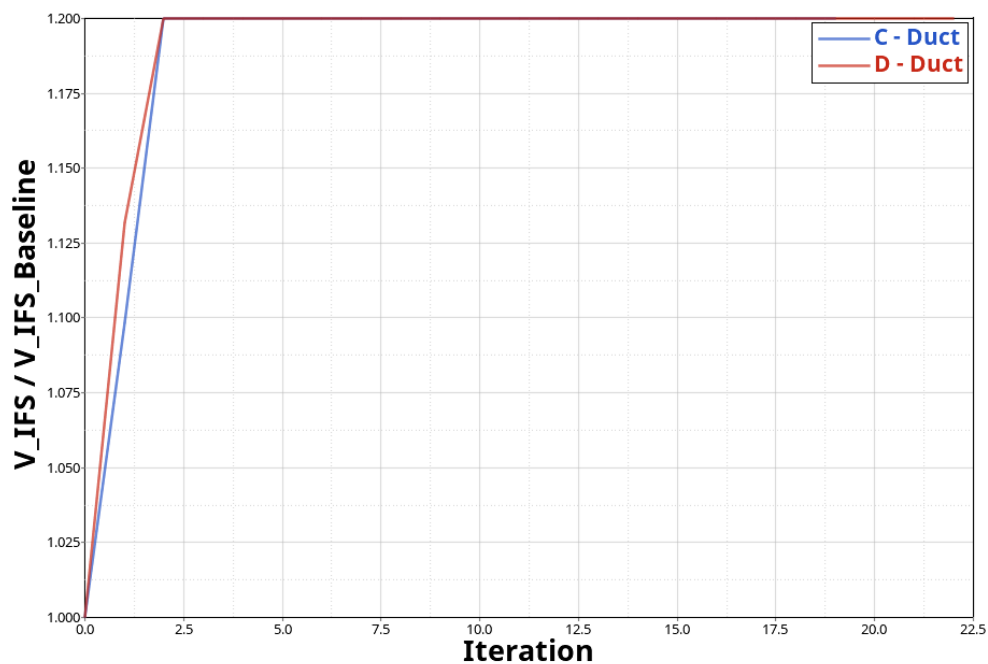


Figure 4.5: Volume fraction evolution during Free Size optimization of IFS thickness

4.4 Free Size Optimization Conclusion

A Free size Optimization has been performed in order to assess the potential benefit of the IFS stiffness on the tip clearance control. For this purpose, the volume of the Thrust

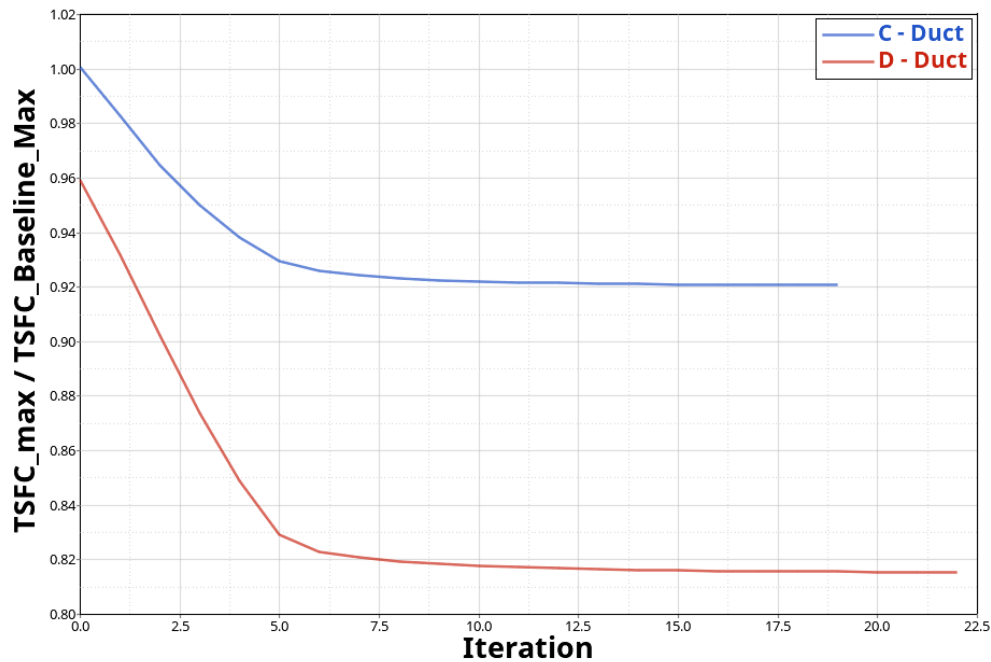


Figure 4.6: Objective evolution during Free Size optimization of IFS thickness

Reverser Inner Structure has been increased by 20%. The additional thickness has been optimized in order to minimize the $TSFC$ associated with the tip clearance variation. The Design Space elements thickness could change between their original values to 8 times that values. The results of the Free Size Optimization show that a more stiff IFS could really improve the tip clearance control since the $TSFC$ resulting from the FS optimization was reduced with respect to the original model.

By performing the Free Size Optimization both on the *C-Duct* and *D-Duct* configuration, also the impact of the lower bifi presence on the $TSFC$ has been evaluated. The lower bifi presence improves the tip clearance control of about 4% compared to the *C-Duct* configuration. Moreover, it increases also the benefit that can be obtained from a more stiff *Inner Fixed Structure*.

Chapter 5

Topology Optimization Problem Formulation

5.1 Design Space for the Topology Optimization

In order to find a Power Plant Structure that could be an innovative solution for UHPR Turbofan issues, a Large Design Space (LDS) was optimized by Topology Optimization. The considered Design Space (DS) includes the original pylon, the front secondary structure, the fan case interface, the IFS internal region, the lower bifi, the engine mounts and the fixed TRU beams (fig.5.1):

- **pylon**: the pylon design space is limited by the rear secondary structure (behind), the bifurcation of the secondary flow (forward), the OFS (on top), the wing interface (on top, behind), the IFS (below);
- **fan case region**: this zone of the design space is between the fan cowl and the fan case;
- **front mount ring**: is the design space zone that is linked to the Torque Box Structure (TBS) and it is limited by the IFS externally and the engine core casing internally;
- **rear mount ring**: it is the design space zone between low pressure turbine case (internally) and the IFS rear panel (externally);
- **IFS region**: this design space is included between the IFS (externally), the core airflow case (internally), the front mount ring (forward) the rear mount ring (behind);
- **lower bifi**: it is the design space region that links the TRU 6 o'clock beams to the IFS region;

- **TRU 6 o'clock beams:** it is the design zone delimited by the extremities of TRU 6 o'clock beams ;
- **front secondary structure and upper TRU beams:** it is is the design space zone that links the fan cowl to the pylon. It also supports the aerodynamic panels on the top. This design zone is laterally delimited by the extremities of the 12 o'clock TRU fixed beams;

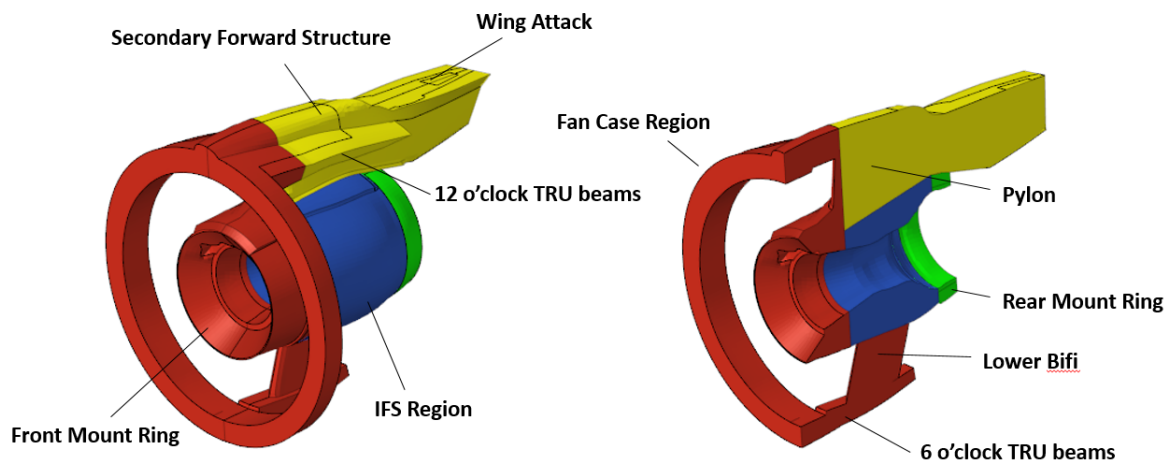


Figure 5.1: Design Space for Topology Optimization (on the left) - Cut Section of the Design Space for Topology Optimization (on the right)

Since the Topology Optimization problem is formulated through the SIMP approach, its result will associate each element of the Design Space with a density value in the range from ρ_{min} to 1. The density distribution will implicitly provide us with an innovative PPS architecture. The design space is made up of 449983 solid elements (*TETRA4* and *PYRA5*) and 14114 shell elements (*TRIA3* and *QUAD4*).

5.1.1 Boundary Conditions

Before the introduction of the discrete assemblies at the Design Space/engine interfaces, the boundary conditions were imposed as follows:

- the rear upper spar of the pylon is fixed to the wing;
- the fan case interface is glued externally to the fan cowl and internally to the fan case;

- the front secondary structure and the upper TRU beams are glued laterally to the extremities of the 12 o'clock TRU fixed beams, to the aerodynamic panels on the top and to the OFS skin internally;
- the front mount ring is glued internally to the compressor core case, forward to the torque box, while externally it is glued to the forward panel of the IFS;
- the rear mount ring is glued internally to the turbine core case and externally to the rear panel of the IFS;
- the design space of the TRU 6 o'clock fixed beams is glued to their extremities;
- the IFS region is glued externally to the IFS panel.

In fig. 5.2 it is possible to see the just mentioned interfaces where the DS was supposed to be glued to the other components: that means that the relative displacement between the surfaces is imposed to be zero. The only exception was represented by the rear mount ring interface with the turbine case where the axial relative displacement was not been constrained: that was done in order to avoid structure damaging during the thermal engine expansion. All the glued assemblies were modelled by TIE elements while the interface between the rear mount and the turbine case was modelled by *Multipoint Constrain Equation* (MPC).

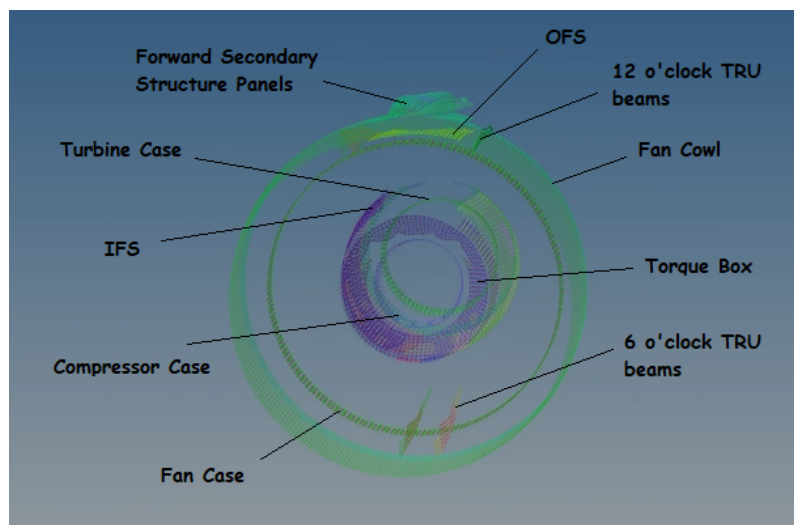


Figure 5.2: Interfaces between the Design Space and the other components

5.1.2 Materials

The material used for the Design Space is a degraded Titanium. In fact, the choice of the material determine the volume associated with a certain amount of mass: for a material

with high density, a smaller volume corresponds to a given value of mass. So, small values of density make the optimization easier since they correspond to higher values of volume fraction. Since in topology optimization similar results are obtained by using different materials which have the same specific stiffness, a degraded material is often used in order to avoid small volume fraction values. That is the reason why the Titanium in our Design Space is degraded, that is to say that it has half the Young module and half the density of the real Titanium material.

5.1.3 Multi-Model Topology Optimization

When the Thrust Reverser Unit is deployed, the nacelle changes configuration (fig. 5.3) and a different model is necessary to perform the finite element analysis. That is the reason why a Multi-Model Topology Optimization has been accomplished: this means that the same design space has been optimized in a single run by taking both the stow and the reverse configuration into account. So, for the compliance minimization, for example, the objective

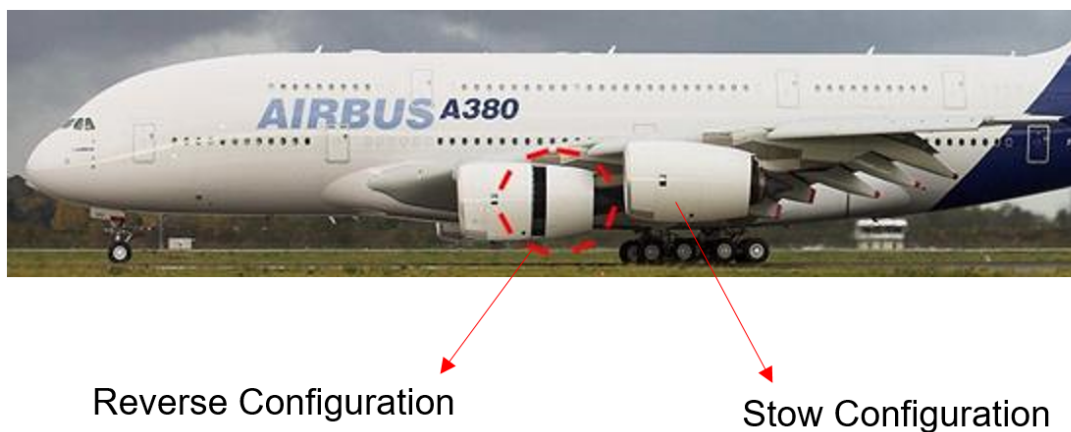


Figure 5.3: Stow and Reverse configuration - source: Airbus Internal Documents - author: Borrel Luce

of the optimization process becomes the *p-aggregation* of the compliance values deriving from the stow and the reverse configuration. Same logic is applied for the optimization constraints which are model-dependent.

5.2 Introduction of Discrete Assemblies

Before the present work, the Design Space (DS) was supposed to be glued to the other components at all the interfaces. That made the model highly hyperstatic. A structure is considered hyperstatic when a smaller number of constraints would have been sufficient in

order to reach the static equilibrium. In the real life aircraft, such hyperstatic assemblies are avoided for the following reasons:

- Firstly, hyperstatic structure are very sensitive to components geometric defects [Oussama Rouetbi 2017]. In fact, while for an isostatic assembly the defects are compensated by clearances to guarantee the assembly requirements, hyperstatic assemblies impose tight clearances. Consequently, in hyperstatic structures, the parts defects are compensated by parts deformation. That means that the mounting of the assembly induces some stress and deformation in the parts and, consequently, the functional requirements of the assembly could be compromised; that is the reason why in [Oussama Rouetbi 2017] the parts tolerances are optimized taking also their deformability into account;
- When a structure is isostatic, the static equilibrium equations are sufficient to determine the reactions forces on the structure. In a hyperstatic structure, the reaction loads are not easy to be determine if the modelled structure is complex and a Finite Element analysis is often necessary. That is the reason why hyperstatic structures make the design phase more difficult than isostatic structures since a Finite Element simulation is necessary to know the reaction forces on the structure after every even little design change;
- Another important drawback of hyperstatic assemblies is that they can not well support thermal loads since they prevent the parts from dilating: consequently, internal stresses are induced if thermal loads are applied. Such internal stresses can be very important if the Degree of Static Indeterminacy (DSI), that is to say the number of redundant constraints in the structure, is high, like for glued surfaces.

For all these reasons, in the current flying aircraft, complex hinged assemblies are employed (fig.5.4) between the pylon and the engine. Their configurations and their models depend on the aircraft.

In the previous internship, in order to allow a certain amount of thermal expansion, the relative axial displacement between the rear mount ring and the turbine casing was not constrained. Unluckily, the rear part of the engine could not be the only one to expand under thermal loads. Moreover, thermal expansions in other directions were still constrained.

Therefore, in order to move toward more realistic modelling hypothesis, in the present work the *Degree of Static Indeterminacy* has been reduced: more specifically, since thermal loads are more important at engine interfaces, TIE contact elements between engine and PPS were replaced by discrete assemblies. These assemblies can be considered as simplified models of the real hinged assemblies.

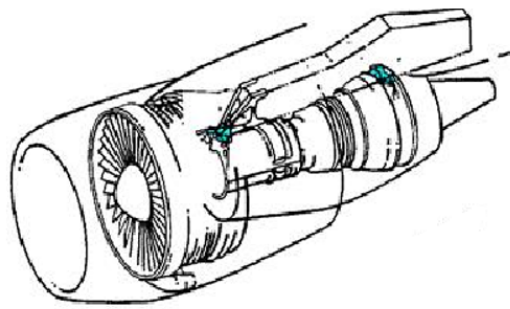


Figure 5.4: Example of rear and forward mount - source: Airbus Internal Documents - Author: Edso

Consequently, the TIE elements on the DS were removed at the the following interfaces (fig. 5.5):

- torque box;
- compressor case;
- turbine case;
- fan case.

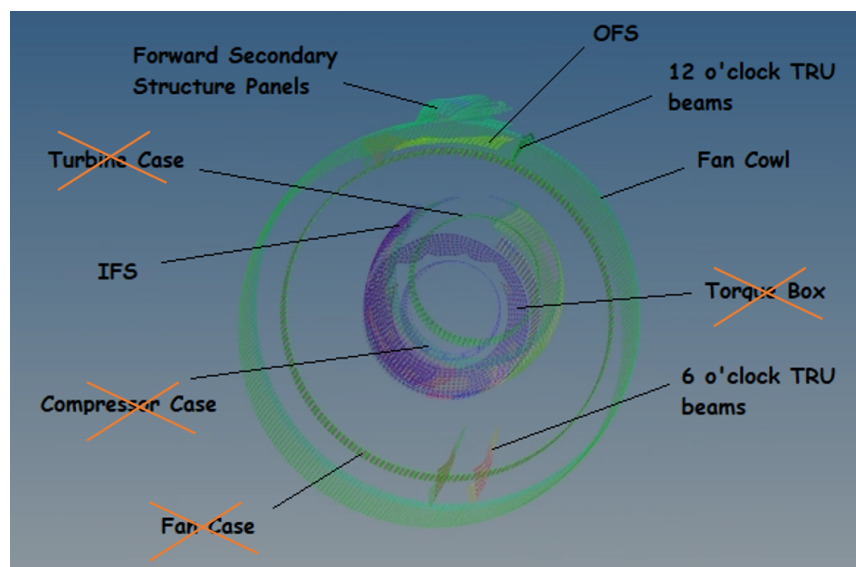


Figure 5.5: Removed TIE surfaces between DS and engine

In order to constrain the engine to the PPS, the removed glued surfaces were replaced by a system of connecting rods: the latter can be considered as simplified models of the hinged

	<i>FRMX</i>	<i>REMX</i>	<i>FAN_REMX</i>
Front mount	F_y, F_z, M_x	F_y, F_z	-
Rear Mount	F_y, F_z	F_y, F_z, M_x	F_y, F_z, M_x
Fan rods	F_y, F_z	F_y, F_z	F_y, F_z
Thrust rods	F_x, F_z	F_x, F_z	F_x, F_z

Table 5.1: Supported loads by the connecting rods for each assembly configuration

assemblies that are used in current operating aircraft. Rods can support only compression and traction so that at least six rods appropriately disposed are necessary to assure the static equilibrium of the engine.

In order to evaluate the effect of the primary load path from the engine to the pylon on the Topology Optimization solution, 3 configurations of assemblies have been investigated:

1. *FRMX*: in this configuration 9 rods have been used as in fig.5.6:

- 2 symmetric rods at the front mount. Their resulting force will be on the yz plan;
- 1 other rod on the front mount to transmit a torque moment M_x , that is to say the moment of its force respect to the virtual point joining the two just mentioned rods;
- 2 thrust rods to transmit thrust to the DS; the transmitted resulting force has an important component on x axis and a small one on the z direction;
- 2 rods at the rear mount resulting in a force on the $y-z$ plan;
- 2 rods at the fan case resulting into another force on the $y-z$ plan;

This configuration of assemblies between pylon and engine is the same as in the original model (*baseline*).

2. *REMX*: in this configuration again 9 rods have been used as in fig.5.7. The only difference compared to the previous configuration is that the third rod on the front mount, that aims to provide a torque moment M_x , is moved to the rear mount;

3. *FAN_REMX*: this configuration is equal to *REMX* with the only difference that there is no connecting rod on the front mount ring (fig. 5.8).

The loads supported by the connecting rods for each configuration are summarized in Table 5.1.

With the only exception for the thrust rods, each connecting rod connects the slave nodes of 2 RBE3 elements: one whose master nodes are on the engine case and the other

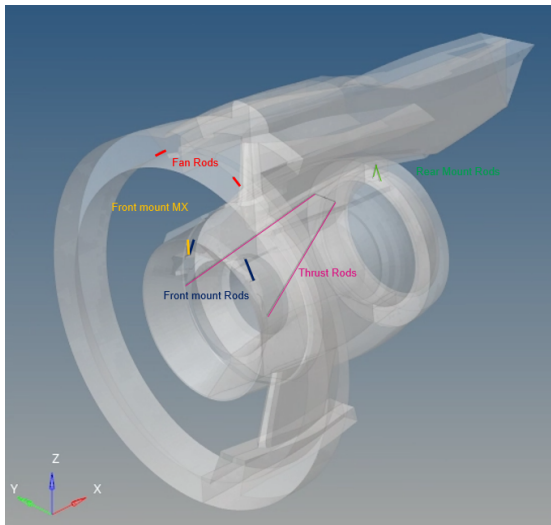


Figure 5.6: FRMX configuration rods

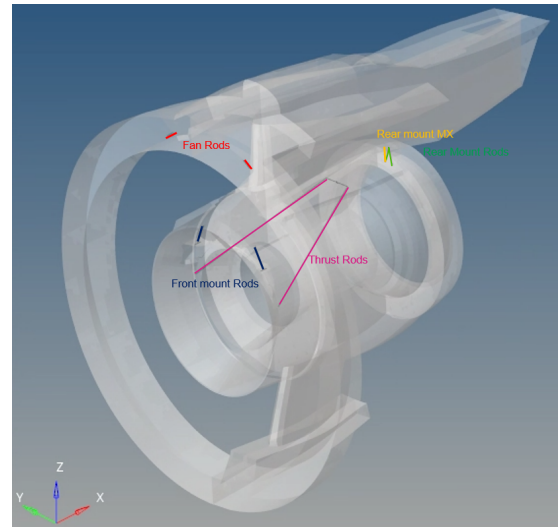


Figure 5.7: REMX configuration rods

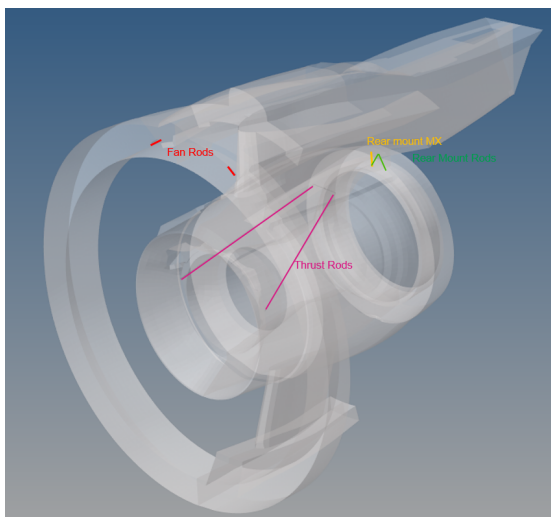


Figure 5.8: FAN_REMX configuration rods

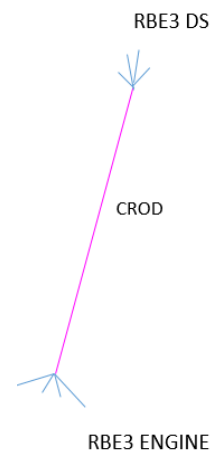


Figure 5.9: Connecting rod general model

with the masters on the Design Space (fig.5.9). The weight of each master nodes has been imposed to 1 so that the slave node's displacement is the average of the master nodes motion.

In order to limit the DSI, thrust rods are supposed to support just a resulting force along the x direction. However, a small component along z axis, due to their inclination, is also accepted. Nevertheless, if each thrust rod was directly connected to the DS by an RBE3 element (like for the other connecting rods) (fig. 5.9), a different value of traction/compression force could have been supported by each rod. This means that the y

component of their resulting force would not have been zero. In order to impose that the same amount of load passes through the thrust loads, a different assembly set-up had to be done. In fig.5.10 the thrust rods model set-up is represented. Two RBE3 are created with

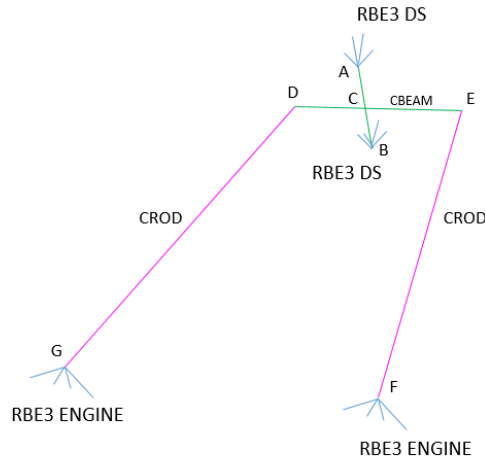


Figure 5.10: Thrust rod modelling

the master nodes on the DS. Displacement at nodes A and B are defined as the average motion of the master nodes, while their rotations are set free. Then 2 CBEAM elements are created to link A and B to C while two other CBEAM elements link the thrust rods to C node. Segment AB is perpendicular to the thrust rods plan. Since rotations at A and B are set free, the moment transmitted by the thrust rods respect to the C node has to be zero in order not to have a rigid body motion: this means that, if the global stiffness matrix is not singular, that is to say no rigid motion is present in the FEM solution, the thrust rods will have to transmit the same traction/compression force.

5.3 Topology Optimization Formulation

Topology Optimization without constraints for $TSFC$ and M_{OGV}

In order to find the stiffest PPS architecture, the following formulation has been set for the Topology Optimization problem:

$$\begin{cases} \min(\max_{i \in J} C(\rho, \mathbf{U}(\rho))) \\ V(\rho) \leq V^* \\ 0 < \rho_{min} \leq \rho_k \leq 1 \quad \forall k \in T_k \end{cases} \quad (5.1)$$

where J are all the load cases, C is the Design Space compliance, U is the vector of nodal displacements, ρ is the vector of density for DS elements, V is the volume of the DS while V^* is the upper limit of the volume constraint, ρ_k is the density value for the k -th element and T_k is the set of the DS elements. A minimum value $\rho_{min} = 0.001$ was imposed for the element density in order to avoid singularities on the stiffness matrix. The upper limit V^* of the volume constraint was imposed so that the optimized Power Plant Structure has the same mass as in the original model. Also in this case, the *max* function of problem 5.1 was replaced by a *p-aggregation* between the load conditions. By this formulation, we aim to find the stiffest architecture by using the same amount of mass for the PPS as in the original model. It is important to specify that only the compliance of the Design Space is considered for the objective computation. Therefore, the optimization problem aims to minimize the deformation energy of the Power Plant Structure regardless the compliance in the other components. In the following paragraphs, we will refer to this formulation as the *Classic Formulation*.

The optimization process stops if one of the following conditions is satisfied:

- The solution has converged, that means that the regular and/or the soft convergence criteria has been satisfied. For this purpose, the objective tolerance has been imposed equal to 0.001. This means that the regular convergence would be satisfied if the relative change in the objective function between two design iterations is less than 0.001.
- A maximum number of iterations, that in this case it is equal to 500, has been reached.

Topology Optimization with constraints for $TSFC$ and M_{OGV}

In order to limit or reduce the the tip clearance impact on TSFC and the bending moment on the OGV blades, the following formulation has also been used:

$$\begin{cases} \min(\max_{i \in J} C(\rho, U(\rho))) \\ \max_{i \in J_1} TSFC \leq TSFC^* \\ \max_{i \in J_2} M_{OGV} \leq M_{OGV}^* \\ V(\rho) \leq V^* \\ 0 < \rho_{min} \leq \rho_k \leq 1 \quad \forall k \in T_k. \end{cases} \quad (5.2)$$

In addition to the previous formulation 5.1, we find J_1 that is the set of fatigue load cases, $TSFC^*$ which is the imposed upper limit to TSFC, J_2 that is the set of limit load conditions, M_{OGV}^* which is the imposed upper limit to the total bending moment on the OGV blades. Since tip clearances variation are mainly due to fatigue loads, limit load

conditions are neglected for the *TSFC* constraint. On the contrary, excessive bending moment on the OGV blades are more likely to happen during limit load conditions: that is the reason why fatigue loads are ignored in the *M_{OGV}* constraint. Even in this case, the *max* functions, both for the objective and the constraints, were approximated by *p-aggregations*. In the following paragraphs the Topology Optimization problem formulated in 5.2 will be referred as *Complete Formulation*. The same criteria of arrest as for the *Classic Formulation* have been adopted.

Chapter 6

Topology Optimization Results without constraints on $TSFC$ and M_{OGV}

6.1 *FRMX* Configuration

First of all, a compliance minimization under a *volume fraction* constraint has been performed for the FRMX configuration (*Classic Formulation* in 5.1). The volume fraction constraint imposes that the optimized Power Point Architecture will have the same mass as in the original model. The great interest of the *FRMX* configuration is that also the original model (*baseline*) has the same configuration of assemblies.

In fig. 6.1 the solution of the Topology Optimization is illustrated where the applied threshold on the density distribution is equal to 0.2: this means that only the elements with density value higher than 0.2 are shown. We can notice that:

- with the same amount of mass as for the pylon of the original model, this Power Plant structure presents a robust front mount supporting the 3 connecting rods. Such robustness is necessary in order to recover the torque moment M_x ;
- 2 very robust ribs are created between the front mount and the rear mount;
- a complex system of truss links the front mount, the ribs and the rear mount together on the underside. This link results to be adjacent to the core case where the temperature reaches high values: that is the reason why the resistance of pylon material to high temperatures should be taken into account in order to assess the manufacturability of such a design. However, the temperature resistance of the Design Space material has not been taken into account as a design criteria in this work;
- the IFS shell is linked to the PPS though 4 contact areas by side: these could represent the hinges by which the IFS is attacked to the PPS and through which it can be

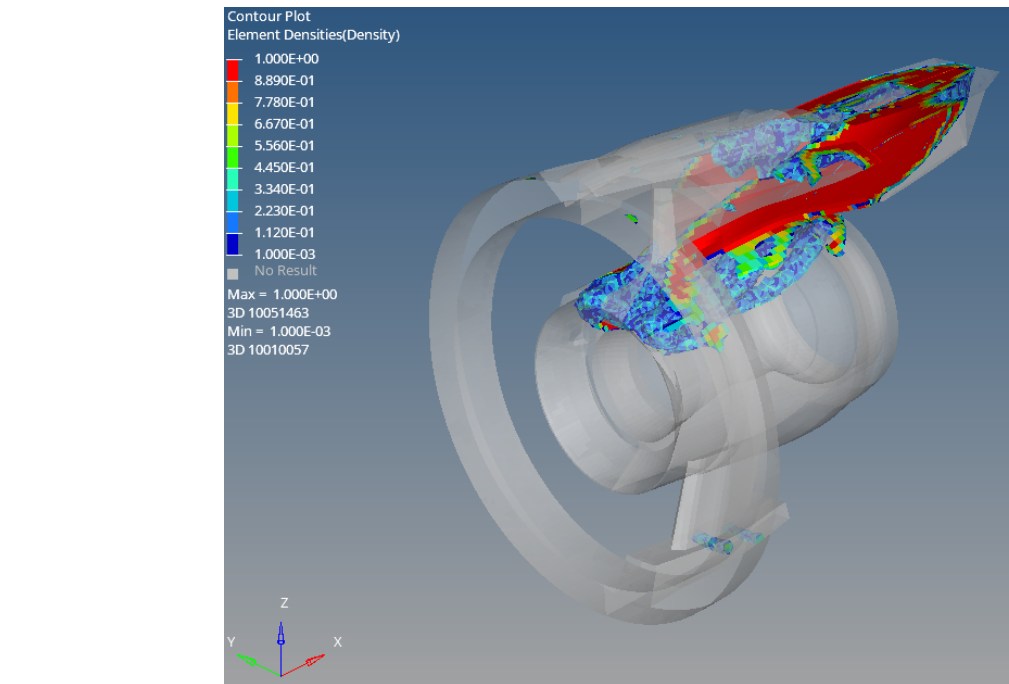


Figure 6.1: Density distribution for FRMX configuration - Classic Formulation - Threshold $\rho = 0.2$

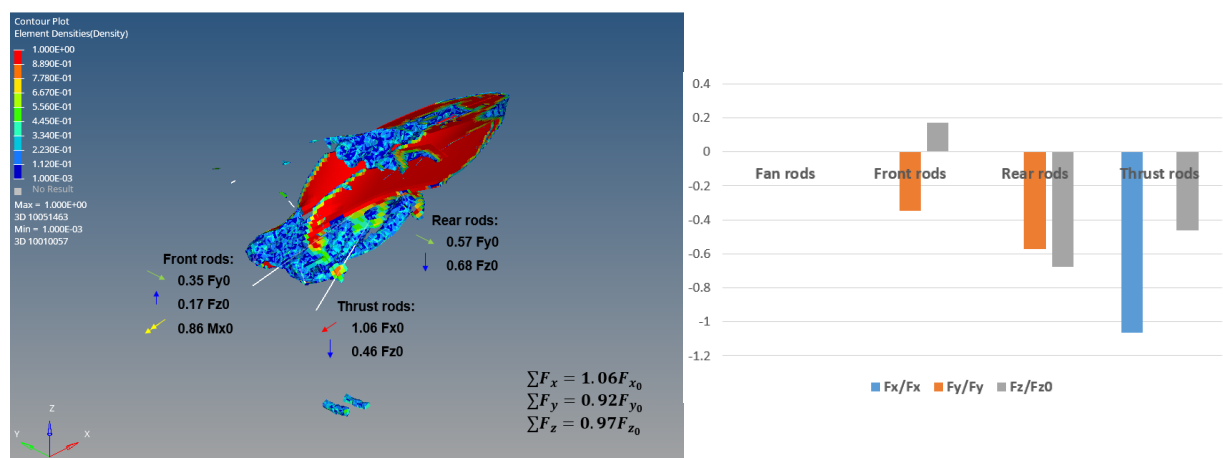


Figure 6.2: FRMX architecture - Loads transmitted to the Power Plant Structure by the connecting rods for an academic load case

opened for maintenance purposes. In order to make the structure the most stiff as possible, these hinges are placed in correspondence with the IFS vertical stiffeners, as in the original model;

- as far as the interfaces with the 12 o'clock TRU beams extremities are concerned, there are 2 resulting contact zones by side;

- two reinforcements are created between the 6 o'clock TRU beams.
- the solution still preserves some features of the classic pylon (fig.3.2), like the two lateral panels. On the contrary, the upper and lower spars have been removed.

An academic load was applied on the engine axis: its resulting components are referred as F_{x0} , F_{y0} and F_{z0} . In figure 6.2, it is possible to look at the forces applied to the Design Space by the engine through the connecting rods: the forces values are side by side with symbols representing their direction. The torque moment M_x that is shown in fig.6.2 represents the moment of the third connecting rod of the front mount respect to the virtual point joining the other two symmetric rods. First of all, the connecting rods result responsible for the transmission of almost all the applied load from the engine to the Power Plant Structure. In fact, the engine results almost in static equilibrium by summing up the applied forces with the ones on the connecting rods. This consideration has been proved to be true also for the resulting moments (not shown). Moreover, we can notice that the fan rods have no elements around: that means that no load path passes through them. Then only 7 rods contribute to the static equilibrium of the engine.

It has already been mentioned that, in order to make the engine isostatic, 6 rods, appropriately disposed, are necessary. By removing the fan rods, the solution actually has 7 rods. Nevertheless, the engine can be considered almost isostatic since an additional equation has to be added for its static equilibrium: the one imposing the same normal load on the thrust rods. Then, given the applied loads on the engine under static equilibrium, the resolution of a system of 7 equations would allow to know the forces on the connecting rods (7 unknowns) with an acceptable error. This error is due to the presence of other secondary interfaces between the engine and the Power Plant Structure: this means that small amounts of load could still pass through these secondary load paths.

Fig. 6.3 shows the history of the Design Space compliance over iterations: the limit load case 2018 of the stow configuration is the one with the highest compliance value. Then, the limit case 2192 of the reverse configuration, the limit case 2019 of the stow configuration and the fatigue load case 1193 of the reverse configuration have high value of compliance too. It is interesting to remark that the reverse configuration has an important impact on the optimization. In fig. 6.4 we can see the objective variation during the optimization process: it is possible to notice how the *p-aggregation* results conservative respect to the max function but it can be still considered a good approximation. In order to make this approximation less conservative, the *p* value of the aggregation should be increased but that could result into an higher computational cost.

Moreover, little steps in the objective history can be observed after 94 and 110 iterations: these steps are due to the optimization problem variations which are associated with the application of the continuation method. However, the solution converged after 121 iterations since the *Regular Convergence* has been reached: in fact the objective function

undergoes a relative variation that is smaller than the objective tolerance (0.001) between the 120th and the last iteration.

In fig. 6.5, the volume fraction, normalized by the upper bound value, is shown over the iterations. We can remark that the constraint is violated during the first 20 iterations. In order to fulfill this constraint, the compliance value increases for each load case (fig. 6.3). Once the volume fraction constraint fulfilled, the architecture is optimized in order to minimize the compliance aggregation.

Since the configuration of assemblies between pylon and engine is the same as in the baseline, it is interesting to make a comparison in terms of performances between these two models. Fig.6.6 shows the total compliance variation of the optimization solution respect to the baseline. It is evident that the optimized Power Plant Structure provides more stiffness since the compliance decreases for all the load cases. More specifically, we can remark that the load cases with the highest final design space compliance (fig.6.3) are also the ones who underwent the higher total compliance reduction respect to the baseline. The maximum compliance value $\max_{i \in J} C$ for this configuration decreases by 21% compared to the baseline.

Then, fig. 6.7 shows, for each load case, the relative change of the resulting bending moment on the OGV blades compared to the baseline. It turns out that the research of the stiffest Power Plant Structure is beneficial also for the total bending moment on the OGV blades: in fact, the $\max_{i \in J_2} M_{OGV}(U(t))$ is decreased by 36%.

Finally, fig.6.8 shows the relative variation of $TSFC$ for each subcase compared to the baseline: tip clearance variations seem to impact in a different way each load case. However, the optimized solution results to be less efficient for the tip clearance control especially for the fatigue load case 1193 of the reverse configuration. More generally, the $\max_{i \in J_1} TSFC(U(t))$ increases of about 41% compared to the baseline. Moreover, in fig. 6.9 the variation of the impact of every engine component on the $\Delta TSFC$ is shown: the fan seems to play a very important role but a CFD analysis should be performed to assess the validity of equation 3.7.

So, using the same configuration of assemblies between the engine and the pylon as in the original model and also the same amount of mass, the topology optimization provided us with a stiffer architecture. As far as the other design criteria are concerned, the obtained solution seems to have a positive impact on the bending moment of the OGV blades while it results worse in terms of tip clearances control. However, it should be mentioned that the compared models are based on different hypothesis and the baseline has a much higher Technology Readiness Level than the presented optimized solution.

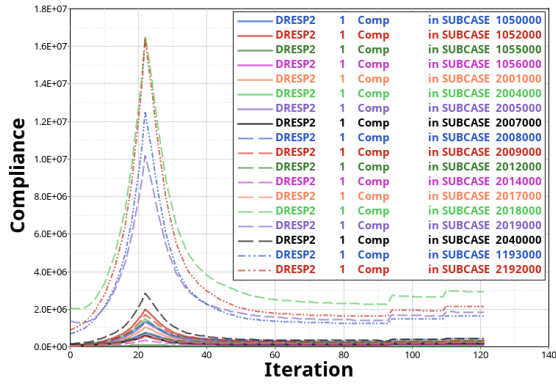


Figure 6.3: Design space compliance history over iterations for *FRMX* configuration

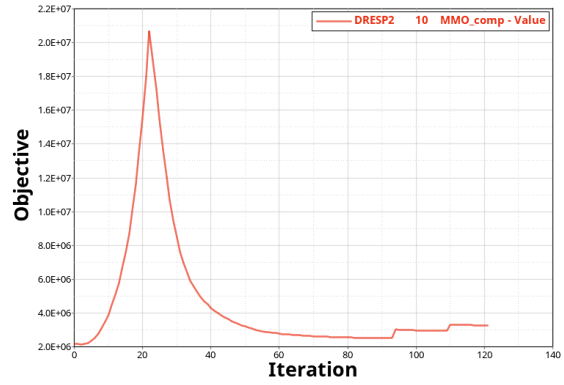


Figure 6.4: Optimization Objective history over iterations for *FRMX* configuration

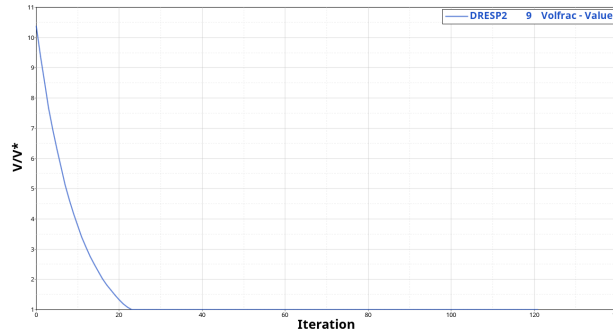


Figure 6.5: V/V^* hystory over iterations for *FRMX* configuration

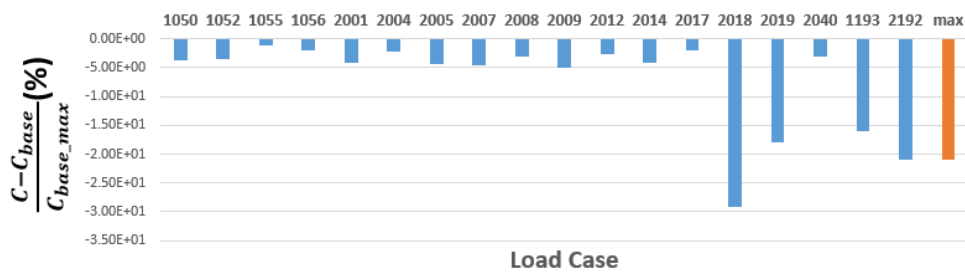


Figure 6.6: Total compliance variation compared to baseline for *FRMX* configuration



Figure 6.7: OGV bending moment variation compared to baseline for $FRMX$ configuration

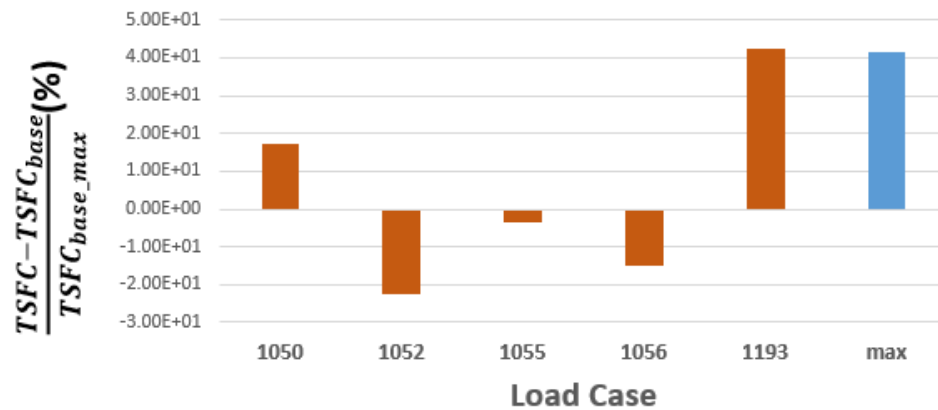


Figure 6.8: TSFC aggregation variation compared to baseline for $FRMX$ configuration

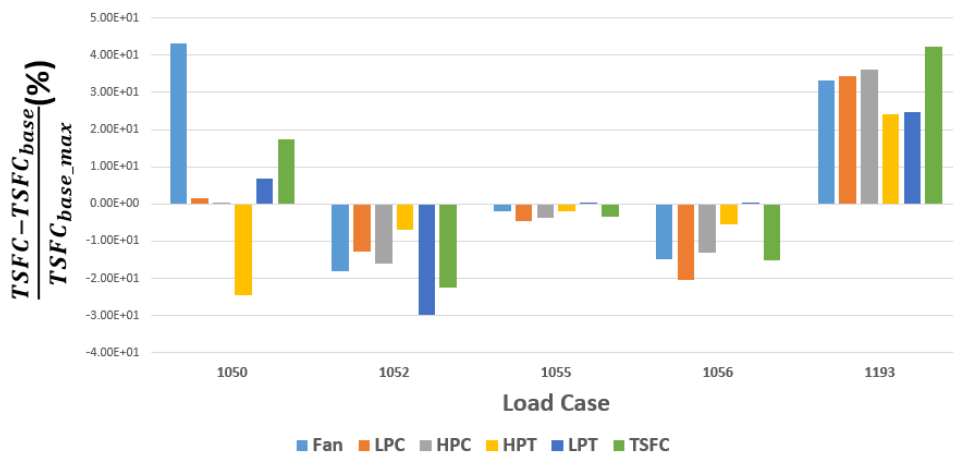


Figure 6.9: TSFC variation for each component and its aggregation compared to baseline for $FRMX$ configuration

6.2 *REMX* Configuration

A compliance minimization has been performed for the *REMX* configuration. The only difference respect to the *FRMX* is that the torque moment is recovered by the rear mount instead of the front mount. The volume fraction constraint was imposed so that the optimized Power Plant Structure has the same mass as in the original model.

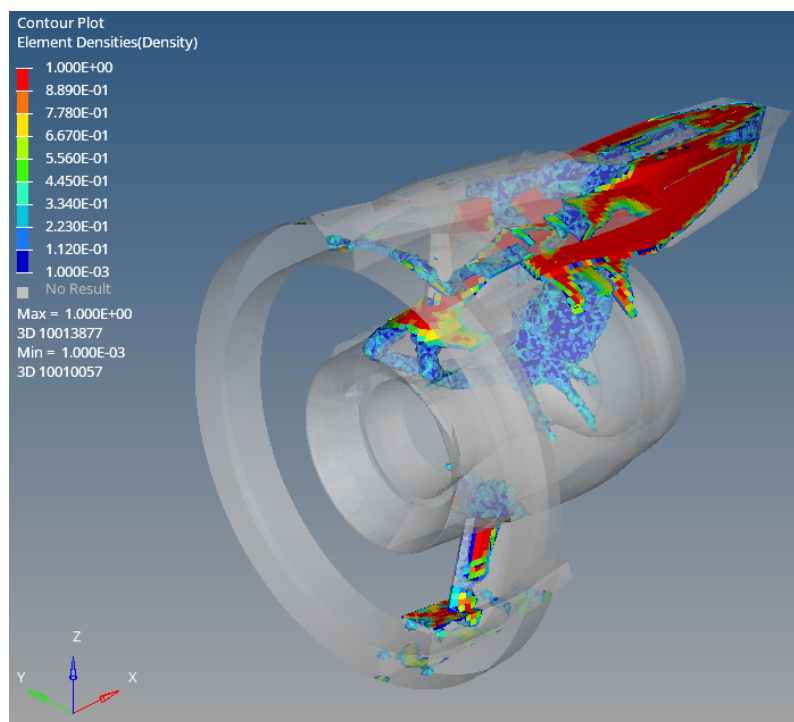


Figure 6.10: Density distribution for *REMX* configuration - Classic Formulation - Threshold $\rho = 0.2$

Fig. 6.10 shows the density distribution of the optimized solution with a threshold equal to 0.2. We can notice that the optimized architecture is very different than the one we obtained for the *FRMX* configuration. In fact we can remark that:

- the front mount rods are linked to a thick plate by two trusses: this plate not only connects the front mount rods to the pylon lateral panels, but it also provide the most forward contact area between the IFS and the pylon;
- overall, 3 contact area by side could represent the hinges linking the IFS to the pylon (instead of 4 hinges like in the *FRMX* configuration). These contact area are, also this time, in correspondence with the vertical stiffeners of the IFS.
- the solution preserves the rear secondary structures as well as the lateral panels of the *FRMX* configuration;

- a lower bifi appears connecting the 6 o'clock TRU beams to the IFS. An important reinforcement is created on the lower part of the IFS, at the junction with the lower bifi.
- a rib with a "v" shape is created between the front and the rear mount, near the thrust rods attack;
- the front mount rods, the rib and rear mount rods are linked on the bottom by two robust trusses. These trusses result, as for the previous configuration, adjacent to the core engine: resistance of materials to high temperature has to be assessed in order to evaluate the manufacturability of this solution;
- several reinforcements are deployed from the just mentioned trusses to reach the IFS. All the created IFS reinforcements make us conclude that the IFS plays an important role as primary load path in this configuration;
- a new structure also appears joining the 12 o'clock TRU beams together and the fan rods: in this configuration the fan rods are active and they give their contribute to the static equilibrium of the engine;
- 3 reinforcements are created between the lower TRU beams.

It is evident that the engine is not isostatically connected to the Topology Optimization solution. First of all, 9 connecting rods seem all being active. Moreover, summing up the forces on the connecting rods with the one applied on the engine, the engine would not result in static equilibrium (fig. 6.11). That means that an important amount of loads is supported by secondary structures: TRU beams and IFS become primary load path contributing, in an important way, to the equilibrium of the structure. This concept according to which the secondary structures contribute in an important way to the primary load path is referred as *cowl load sharing*.

The reason why the optimization algorithm found such an hyperstatic solution as the stiffest one is that the moment arm of the third connecting rods respect to the junction of the other rear rods is smaller compared to the previous assemblies configuration. In fact, for the academic load condition in fig.6.11, the rear mount manages to support only the 12% of the total applied torque moment. Then, in order to make the rear mount support all the torque moment, an higher amount of force should have passed through the third rod of the rear mount. As a result, a more robust rear mount would have been necessary to avoid excessive strains. On the other hand, the rear mount dimensions, and so its moment arm, are limited in order to assure an appropriate aerodynamic shape to the rear secondary structure.

In fig. 6.11 it is remarkable that the connecting rods manage to support almost all the axial and vertical components of the applied load while the y one must be transmitted by

secondary the structures. In the shown diagram (fig.6.11) the fan connecting rods don't seem to play an important role for the static equilibrium of the engine: nevertheless, it should be reminded that the considered academic load, represented in the figure, was not taken into account in the optimization process and it is used just to have an idea of the DSI of the obtained solution.

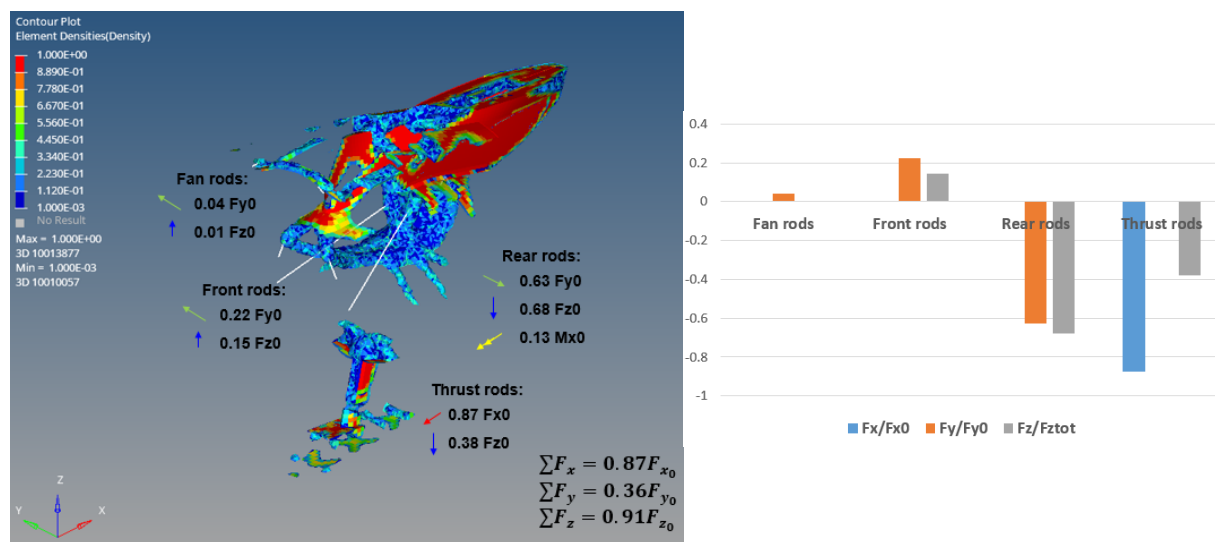


Figure 6.11: REMX architecture - Loads transmitted to the Power Plant Structure by the connecting rods for an academic load case

Fig. 6.12 shows the compliance computed in the design space during the optimization process. We can see that the higher deformation energy concerns again the 2018 load case, followed by load case 2192, 2019 and 1193. The evolution of the objective function (fig. 6.13) and the volume fraction constraint (fig. 6.14) is similar to the *FRMX*. Despite the irregularities due to the continuation method, the solution reached the *Regular Convergence* after 127 iterations.

As far as the performances are concerned, for the *REMX* configurations, as well as for the following ones, it is more interesting to compare the results to the solution obtained from the *Classic Formulation Problem* applied to the *FRMX* configuration (rather than to the *baseline*): that would allow us to compare solutions based on the same hypothesis and the same maturity degree. That is why, in the following paragraphs, the symbols C_0 , $TSFC_0$ and M_{OGV_0} are referred respectively to the compliance, the *Thrust Specific Fuel Consumption* and the bending moment on *Outlet Guide Vane* of the solution shown in fig.6.1. First of all, in fig. 6.15 we can see that the *REMX* solution results into an architecture who is less stiff than the *FRMX*, especially for the load cases who lead the optimization process (2018, 2019, 1193, 2192). The maximum compliance value $\max_{i \in J} C$ increases by 27% compared to *FRMX*.

On the other hand, this architecture has better performances in terms of *TSFC* and

bending moment on the OGV blades than $FRMX$ configuration. Fig. 6.16 shows as the bending moment on OGV blades has been reduced under every load case except for the 2018. Anyway, last column of the graph shows that the maximum value $\max_{i \in J_2} M_{OGV}(U(t))$ of bending moment is decreased by 22%. Tip clearances control is also improved by this configuration for all the load case: more specifically the maximum value $\max_{i \in J_1} TSFC(U(t))$ was decreased by 23% respect to $FRMX$. In fig. 6.18, it is evident that the configuration $REMX$ improves the aerodynamic performance in every component for almost all the load cases.

In conclusion, to support all the torque moment on the rear mount is not easy if aerodynamic constraint have to be fulfilled on the rear secondary structure: that is why other load paths, beyond the connecting rods, are activated to minimize the pylon compliance: the IFS, the lower bifi and the TRU beams contribute, in an important way, to the static equilibrium of the engine. Such a *cowl load sharing* seems to degrade the stiffness respect to the $FRMX$ solution. On the other hand, to make secondary structure contribute to the primary load path seems to improve the performances in terms of bending moment on the OGV blades and tip clearance control. The appearance of the lower bifi is again associated with an improvement of the $TSFC$ design criteria as already assessed in the IFS Free Size Optimization chapter.

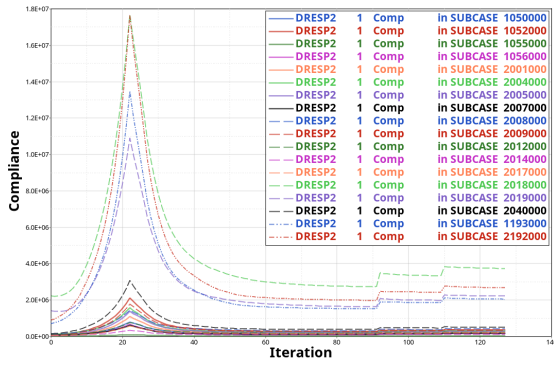


Figure 6.12: Design space compliance history over iterations for *REMX* configuration

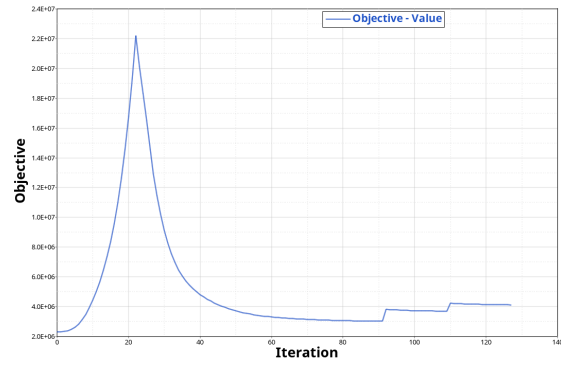


Figure 6.13: Optimization Objective history over iterations for *REMX* configuration

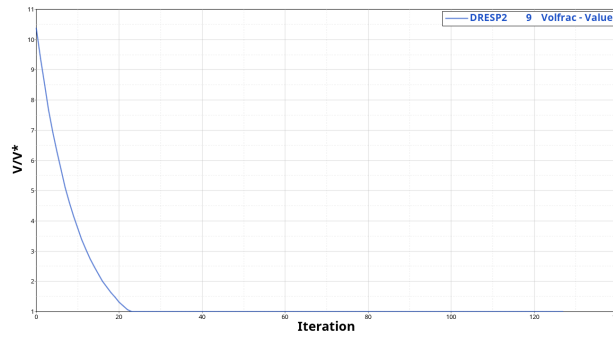


Figure 6.14: V/V^* history over iterations for *REMX* configuration

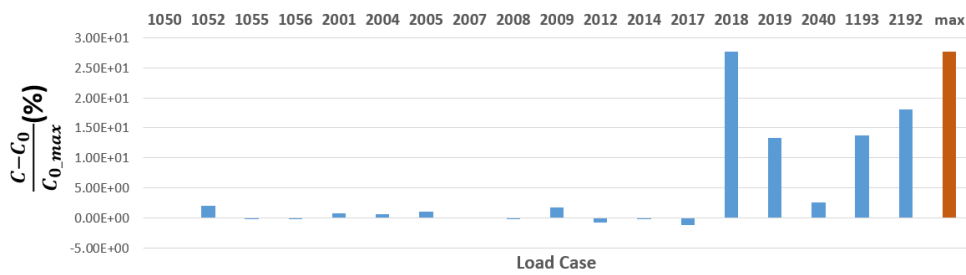


Figure 6.15: Design Space compliance variation compared to *FRMX* for *REMX* configuration

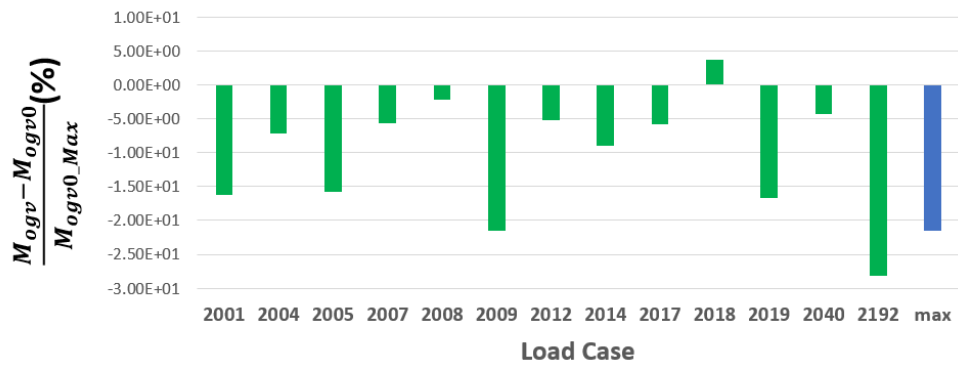


Figure 6.16: OGV bending moment variation compared to $FRMX$ for $REMX$ configuration

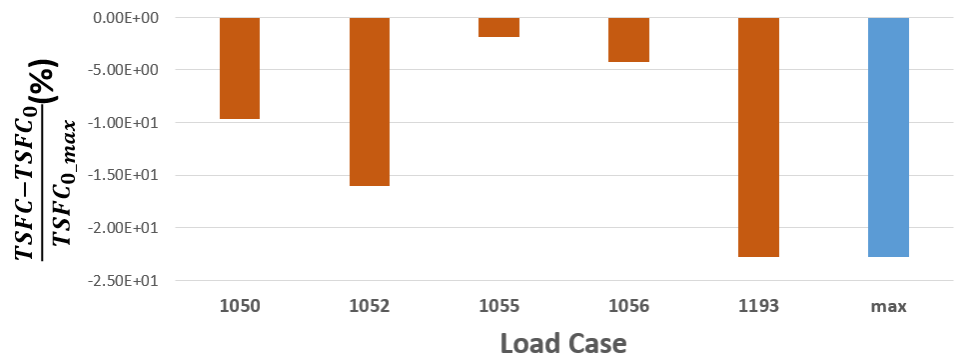


Figure 6.17: TSFC aggregation variation compared to $FRMX$ for $REMX$ configuration

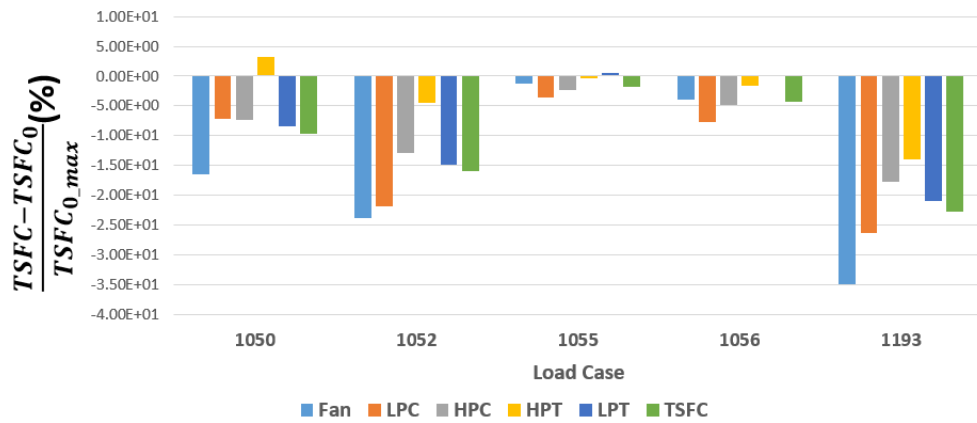


Figure 6.18: TSFC variation for each component and its aggregation compared to $FRMX$ for $REMX$ configuration

6.3 *FAN_REMX* Configuration

As for the previous configurations, also for the *FAN_REMX* a compliance minimization was performed with the same mass constraint. The only difference respect to the *REMX* configuration is that no connecting rod is placed on the front mount. As already stated, under the academic load case, all the loads are applied on the engine axis: that means that, if the connecting rods resulted to be the only load path from the engine to the Power Plant Structure in this configuration, the engine would be isostatic. In fact, in that case, the rods are disposed in such a way that the equilibrium would impose a system of 7 equations with 7 unknowns (the normal force on each connecting rod).

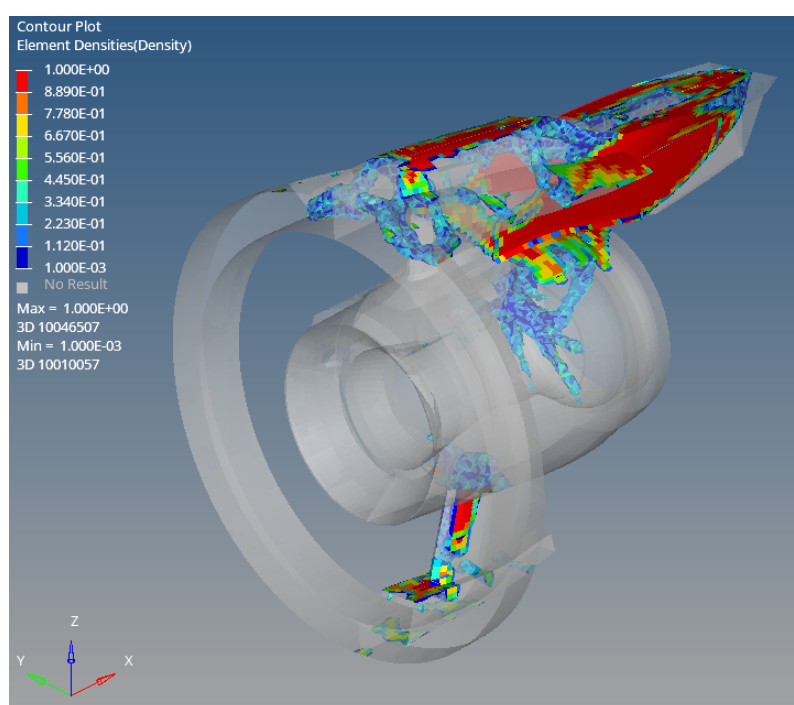


Figure 6.19: Density distribution for *FAN_REMX* configuration - Classic Formulation - Threshold $\rho = 0.2$

In fig. 6.19 the obtained density distribution is shown with a threshold equal to 0.2. It is possible to remark that:

- a lower bifi appears like in the previous configuration with the same reinforcement at the junction with the IFS;
- also this time a 'v' shape rib is created before the rear mount;
- contacts between pylon and IFS are further reduced for this configuration: only two by side while they were originally 4. However, they are always placed in correspondence with the IFS vertical stiffeners;

- no front mount is created because of the absence of connections with the engine (no connecting rods on the front mount);
- IFS reinforcements, like in the previous configuration, are deployed from the rib. Moreover, two trusses link the rear mount to this set of IFS reinforcements;
- a complex system of robust trusses is created in correspondence with the fan connecting rods: in fact, since no front mount exist, it is evident that the fan connecting rods must undergo higher forces in this configuration than in the others; a robust structure link this truss system to the "v" shaped rib;
- 3 reinforcements for the 6 o'clock TRU beams are created;
- the contact surface between the Design Space and the 12 o'clock TRU beams are larger the in the previous configurations;

In fig. 6.20 it is possible to look at the forces applied to the Design Space by the engine through the connecting rods under the academic load case. As for the *REMX* configuration, also this time an hyperstatic structure is obtained: in fact, the connecting rods are not sufficient to guarantee the static equilibrium of the engine. This means that the load path from the engine to the Design Space is not made up only of the connecting rods but other interfaces, like the TRU beams and the IFS, contribute to the static equilibrium of the engine. The reason of such an hyperstatic structure is still due to the fact that the torque moment should be recovered mainly by the rear mount but its moment arm is too small to provide a feasible stiff solution. It results to be especially the y force component that is mainly recovered by the secondary structures. Moreover, comparing the histogram in fig.6.20 with the one in fig. 6.11, we can notice that the fan rods recover now the forces that, in the *REMX* configuration, were supported by the front rods.

Looking at the design space compliance history (fig. 6.21), we can remark that, also for this configuration, the load cases leading the optimization are the 2018, 2192, 1193 and 2019. The objective and constraint evolution (fig.6.22 and 6.23) are similar as in the previous configuration: firstly an initial increase of compliance in order to fulfill the volume constraint and then, once the constraint has been fulfilled (after about 22 iterations), the objective minimization. The *Regular Convergence* has been reached after 129 iterations.

In order to do a congruent comparison, the performances of the *FAN_REMX* configuration are compared respect to the *FRMX* solution. Fig. 6.24 shows the variation of compliance, computed at the Design Space, for each subcase: this configuration results to be less stiff for every load case. The obtained stiffness is even worse than the one obtained with the *REMX*. In fact, it seems that the worst compliance value $\max_{i \in J} C$ increases by 41% respect to *FRMX* (vs. to +27% with *REMX*).

However, also this time the *cowl load sharing* seems to be beneficial for the engine strain criteria, like the bending moment on the OGV and the tip clearances impact on

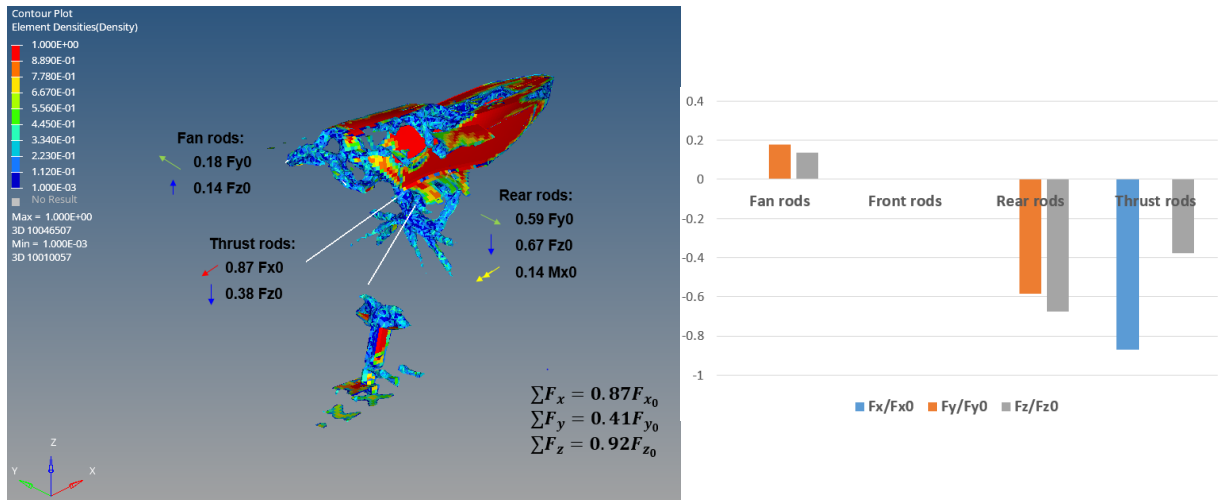


Figure 6.20: *FAN_REMX* architecture - Loads transmitted to the Power Plant Structure by the connecting rods for an academic load case

TSFC. Fig.6.25 shows that, with this configuration, the bending moment on the OGV blades is much reduced compared to the *FRMX* under the majority of the load cases. This configurations proves actually to be the most efficient for the bending moment on the OGV blades since it allows a reduction of $\max_{i \in J_2} M_{OGV}(U(t))$ by 26% respect to the *FRMX* configuration.

Fig.6.26 shows that tip clearances are reduced under every load case and that the $\max_{i \in J_1} TSFC(U(t))$ is reduced by 61% compared to *FRMX* configuration: also the tip clearances control takes advantage from this configuration.

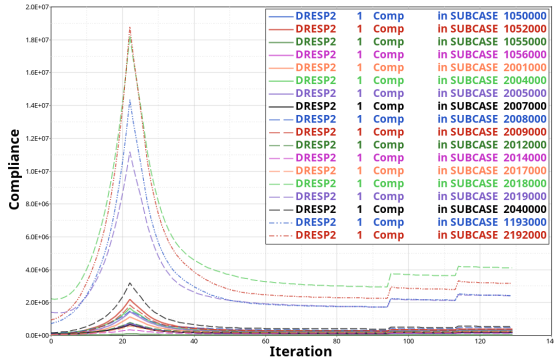


Figure 6.21: Design space compliance history over iterations for FAN_REMX configuration

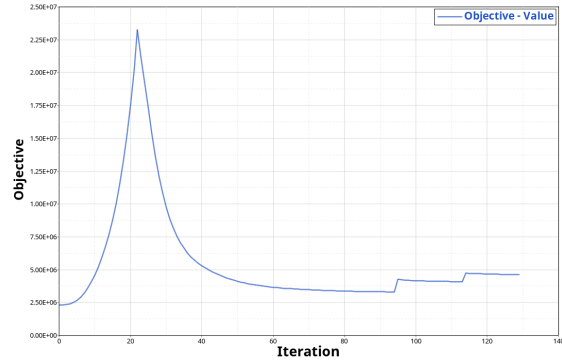


Figure 6.22: Optimization Objective history over iterations for FAN_REMX configuration

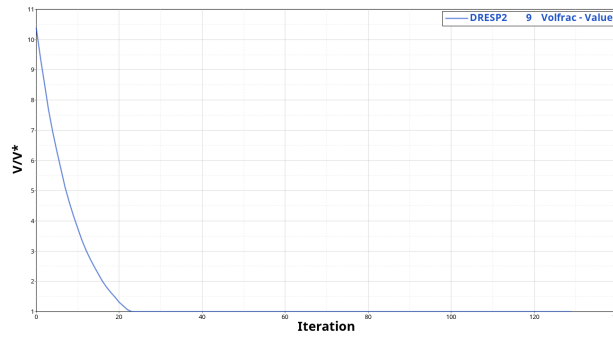


Figure 6.23: V/V^* hystory over iterations for FAN_REMX configuration

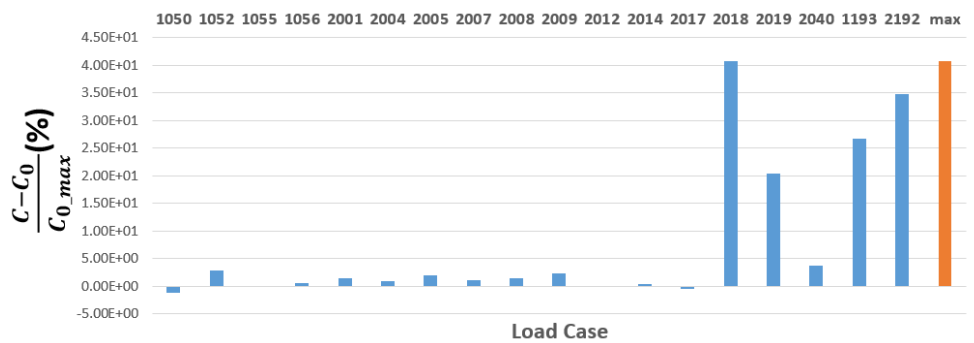


Figure 6.24: Design Space compliance variation compared to $FRMX$ for FAN_REMX configuration

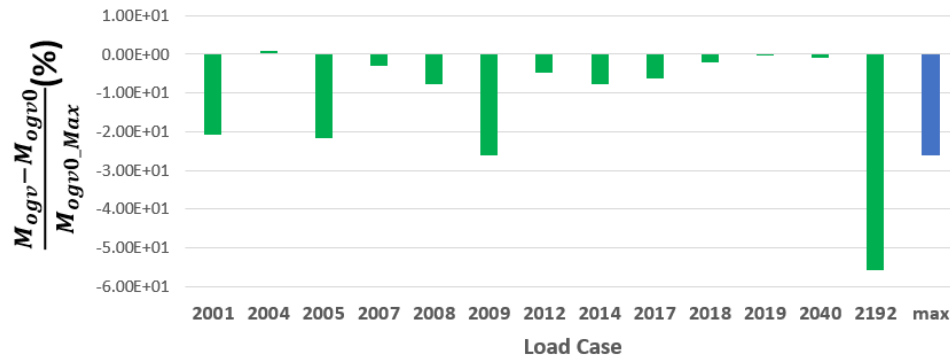


Figure 6.25: OGV bending moment variation compared to *FRMX* for *FAN_REMX* configuration

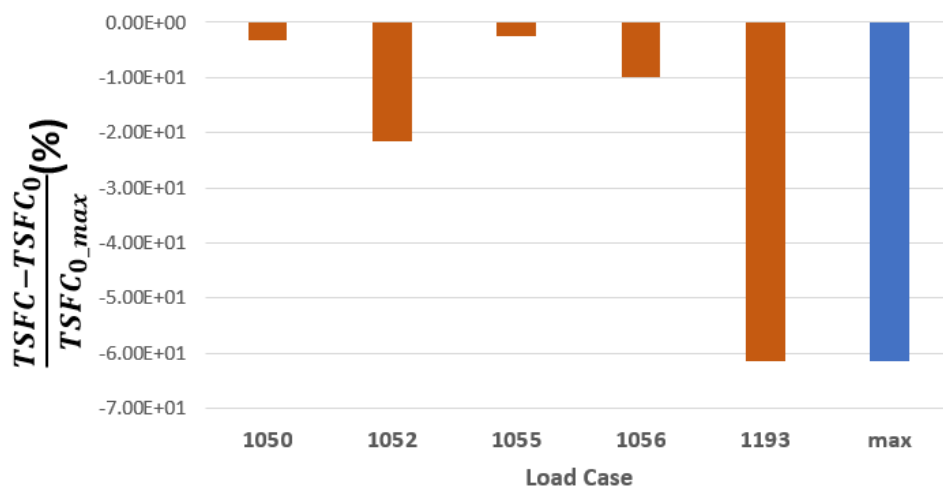


Figure 6.26: TSFC aggregation variation compared to *FRMX* for *FAN* configuration

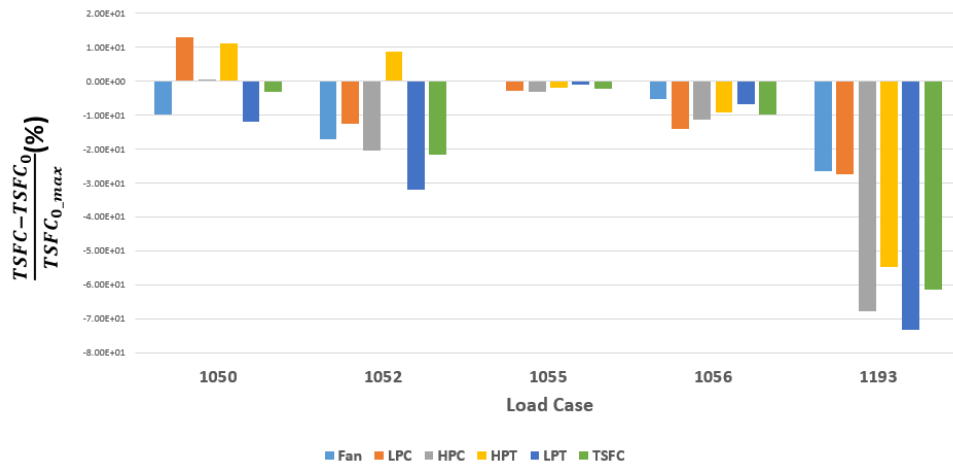


Figure 6.27: TSFC variation for each component and its aggregation compared to $FRMX$ for FAN_REMX configuration

6.4 Topology Optimization with glued interfaces between the Design Space and the Engine

In order to show the impact of the TIE replacement by the connecting rods, the *Classic Problem* (5.1) solution is here presented by keeping the glued interfaces between the Design Space and the engine. This optimization problem is the same as the one solved during Gabriele Capasso's previous internship and it is shown in this work in order to make a comparison with the solutions obtained using the connecting rods.

In this configuration we replaced the connecting rods by the original TIE elements and MPC (for the rear mount) as in fig.5.2. Only at the rear mount interface with the turbine case the axial relative motion was not constrained. The obtained density distribution is shown in fig. 6.28. It is possible to remark that:

- the fan case presents some reinforcements: two on the upper side and two at the bottom. Moreover two lateral stiffeners are created between the fan case and the fan cowl;
- two reinforcements as in the *FRMX* configuration are created between the 6 o'clock TRU beams;
- a tighter and robust front mount, compared to the *FRMX* configuration, is created;
- a central rib is created, whose shape is like a "v", between the front mount and the rear mount. However, it is less robust than the *FRMX* configuration ribs;
- a robust rear mount is glued to the turbine case;
- also this time, the solution tries to create a structure, adjacent to the engine core, connecting the front mount, the ribs and the rear mount like a sort of spar;
- some reinforcements are also created on the IFS external circumference;
- the IFS is supported by the Power Plant Structure only on a contact area near the rear mount.

Fig.6.29 shows the resulting forces on the Design Space at the interfaces with the engine for the academic load case. The Power Plant Structure manages to make the engine stay in equilibrium since the resulting forces and moments (not shown) equilibrate the applied load on the engine;

- the fan case stiffeners transmit a certain amount of F_y and F_z to the fan cowl;
- the front mount seems to support all the thrust and some amount of F_y ;

- the rear mount aims to take F_y and F_z in order to equilibrate the engine.

Secondary structures do not contribute in an important way to the primary load path.

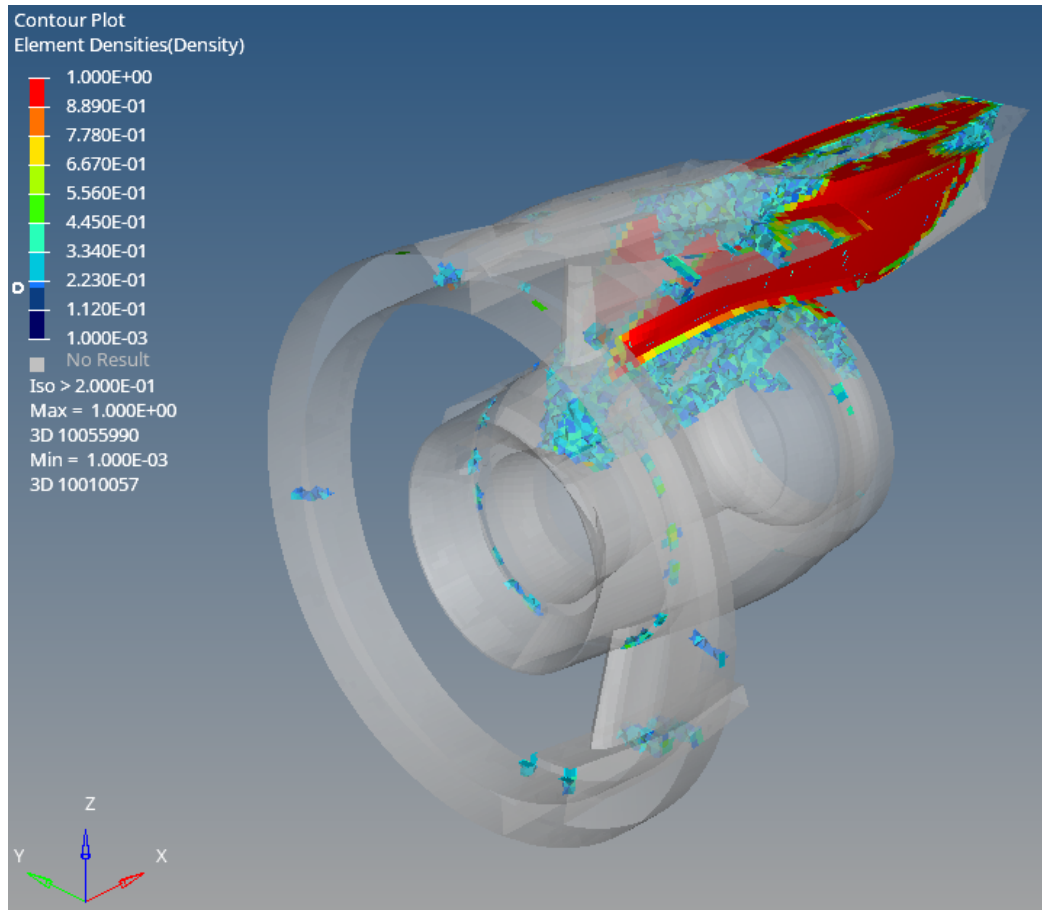


Figure 6.28: Density distribution for model with glued interfaces between the engine and the Design Space - Classic Formulation - Threshold $\rho = 0.2$

As far as the convergence history of the optimization responses are concerned (fig.6.30, 6.31 and 6.32), a similar behaviour to the previous configurations has been observed. The *Regular Convergence* has been reached after 118 iterations. On the other hand, the presence of glued surfaces, instead of the connecting rods, allows a better performance in terms of compliance and engine displacements. The comparison is always made respect to the reference configuration, that is to say the *FRMX*:

- fig.6.33 shows that, thanks to the glued interfaces with the engine, the deformation energy inside the Power Plant Structure is reduced for almost every load case. More specifically, the $\max_{i \in J} C$ is reduced by 27%;

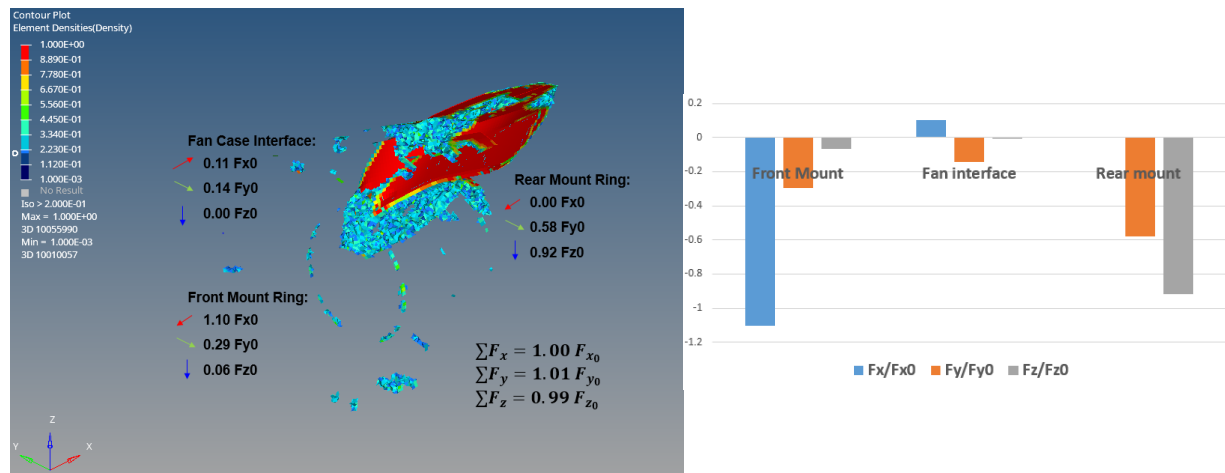


Figure 6.29: Glued interfaces model - Loads transmitted to the Power Plant Structure by the connecting rods for an academic load case

- also the resulting bending moment on the OGV blades is reduced for the majority of the load cases and the $\max_{i \in J_2} M_{OGV}$ is reduced by 23% (fig.6.34);
- only the load case 1050 undergoes an increase in TSFC while all the other load case benefit from the glued interfaces (fig.6.35). More specifically, the $\max_{i \in J_1} TSFC$ was reduced by 5% respect to the *FRMX* configuration. The glued interfaces between pylon and engine seem to reduce the TSFC impact of the Fan component for all the load cases (fig.6.36) while the effect on the other components depend on the considered load case.

Finally, the introduction of discrete assemblies between the Design Space and the engine results in a less stiff Power Plant Structure with degraded performances also in terms of *TSFC* and M_{OGV} . On the other hand, by replacing the glued interfaces through the connecting rods system, we move toward more realistic model hypothesis and more manufacturable solutions.

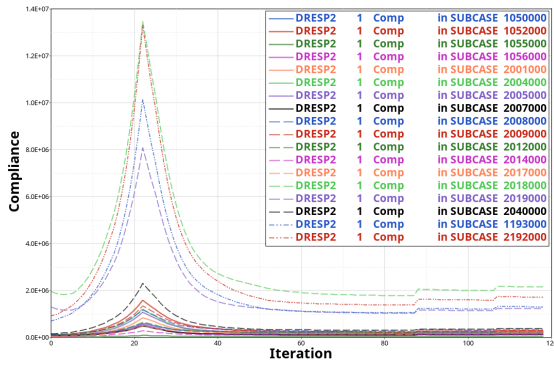


Figure 6.30: Design space compliance history over iterations for configuration with glued Design Space-Engine interfaces

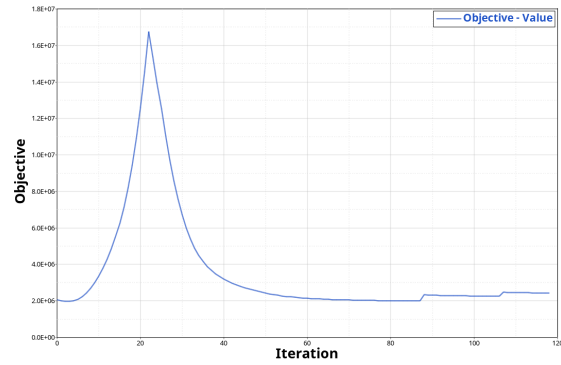


Figure 6.31: Optimization Objective history over iterations for configuration with glued Design Space-Engine interfaces

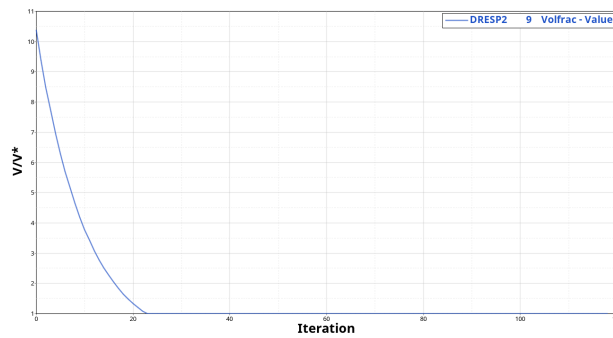


Figure 6.32: V/V^* hystory over iterations for configuration with glued Design Space-Engine interfaces

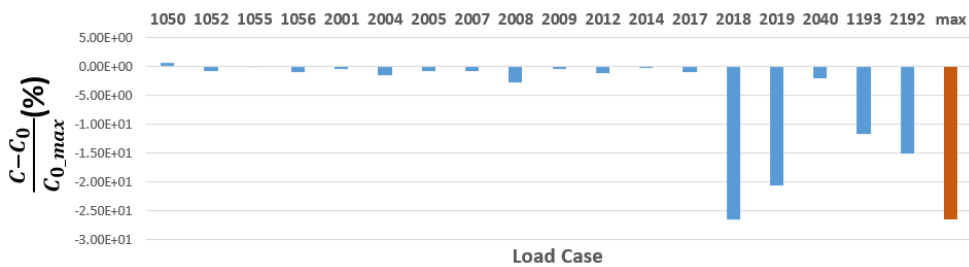


Figure 6.33: Design Space compliance variation compared to $FRMX$ for TIE configuration

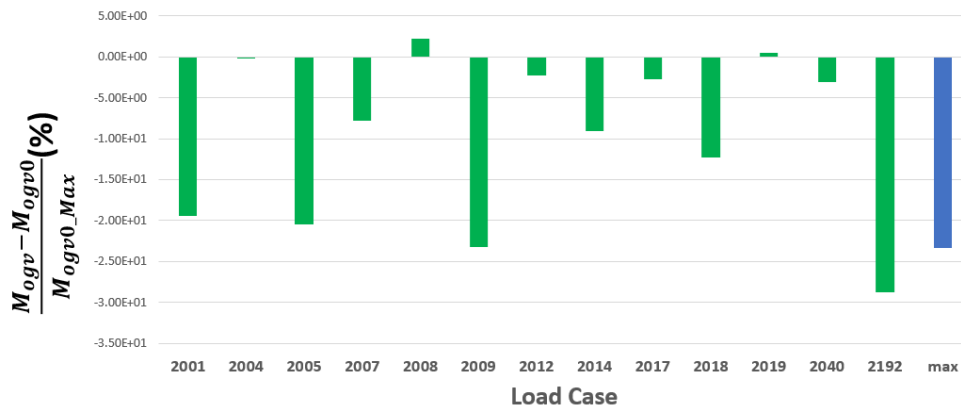


Figure 6.34: OGV bending moment variation compared to *FRMX* for *TIE* configuration

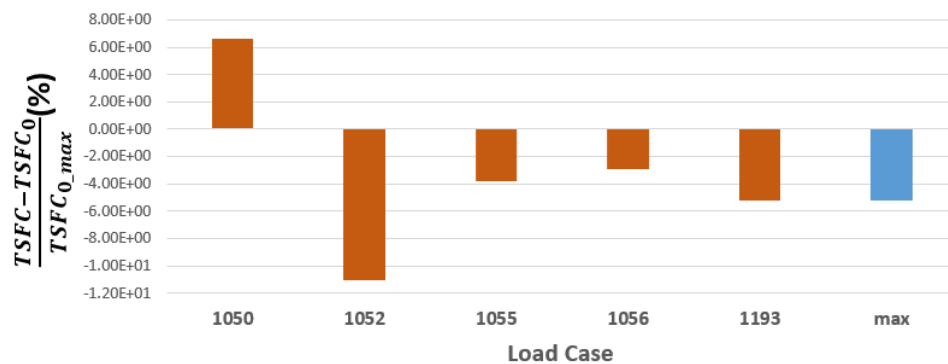


Figure 6.35: TSFC aggregation variation compared to *FRMX* for *TIE* configuration

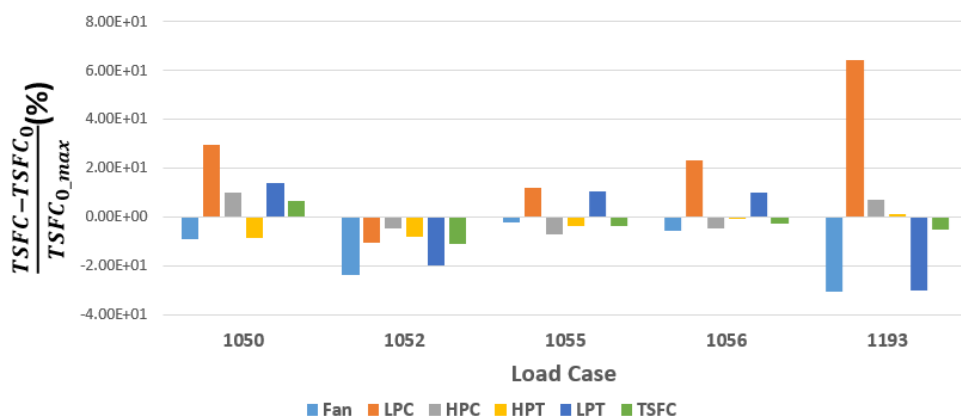


Figure 6.36: TSFC variation for each component and its aggregation compared to *FRMX* for *TIE* configuration

Chapter 7

Topology Optimization Results with constraints on $TSFC$ and M_{OGV}

7.1 Topology Optimization of *FRMX* configuration - Complete Formulation

As seen in the previous paragraphs, the FRMX configuration is the one which allows the lowest compliance compared to the other configurations. On the other hand, the performances which are associated with the engine displacements ($TSFC$ and M_{OGV}) could be still improved. That is the reason why the FRMX configuration has been submitted to a Topology Optimization with two additional constraints respect to the *Classic Formulation*: one on the $TSFC$ impact of the tip clearances and one on the bending moment of the OGV blades. The problem formulation, that will be called *Complete Formulation*, has been illustrated in 5.2. The additional constraints have been introduced to reduce the p-norms functions of $TSFC_{j \in J_1}$ and $M_{OGV_{j \in J_2}}$ by 15% respect to the values obtained by the *Classic Formulation* for the same configuration of connecting rods.

The obtained density distribution, with a threshold equal to 0.2, is shown in fig.7.1. Compared to the *Classic Problem* solution (fig. 6.1), we can remark the following variations:

- a lower bifi structure is created, connecting the 6'clock TRU beams to the IFS. Once again, the presence of a lower bifi proves to be important for the engine displacements control;
- at the junction with the lower bifi, the IFS elements are made thicker by some shell elements of the Design Space. This is in accordance with what was assessed by the Free Size Optimization results: when the lower bifi is present, the bottom part of the

7.1. Topology Optimization of *FRMX* configuration - Complete Formulation 77

IFS could be made thicker in order to further improve the tip clearances;

- the already existing ribs, which are adjacent to the engine core, are now less robust;
- an additional "x" shaped rib is created between the thrust rods and the rear mount rods.

As for the previous configurations, in fig. 7.2 the forces passing through the connecting rods and their resulting values are shown for the academic load case. Compared to solutions obtained from the *Classic Formulation* (fig.6.2), the connecting rods are slightly less charged and secondary structures, like the lower bifi, contribute to form a primary load path by connecting the lower TRU beams to the Design Space through the IFS: the solution presents an higher DSI than in the *Classic Problem* and the *cowl load sharing* proves again to be beneficial for the design criteria that are associated to the engine displacements.

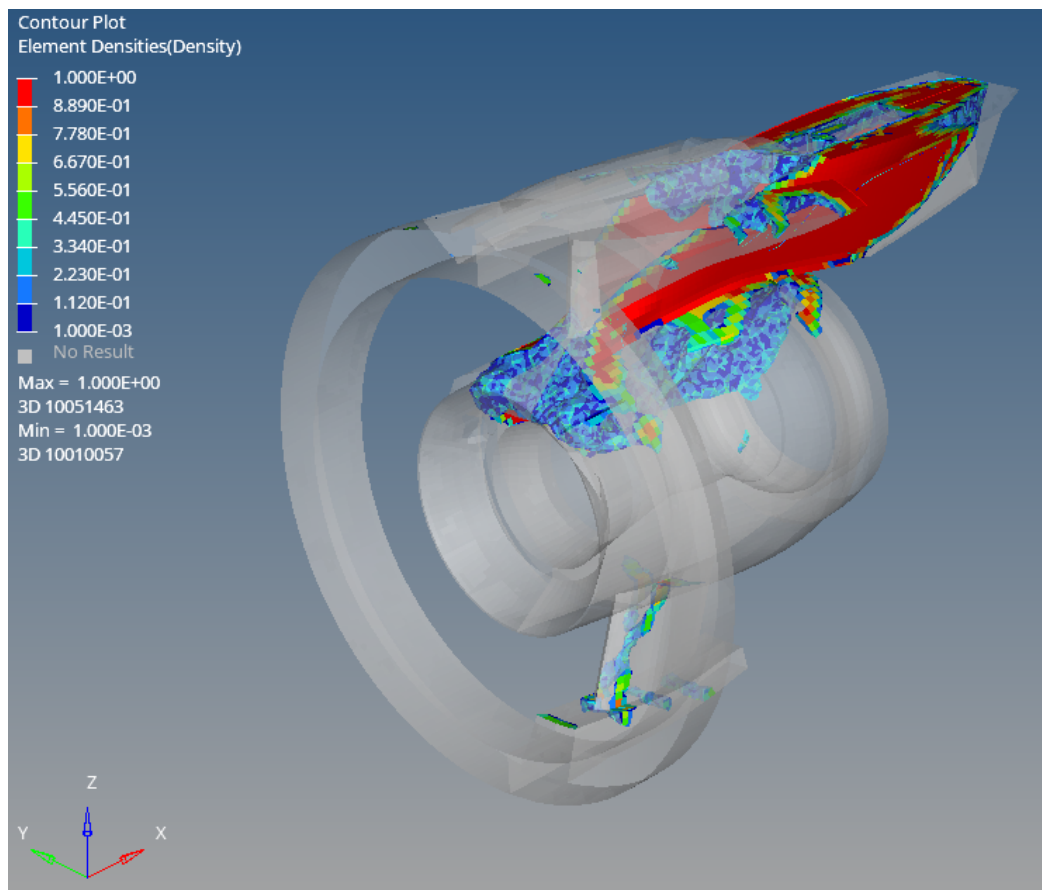


Figure 7.1: Density distribution for *FRMX* configuration - Complete Formulation - Threshold $\rho = 0.2$

In the figures 7.4, 7.4 and 7.5, 7.6, it is possible to remark the following behaviours during the optimization:

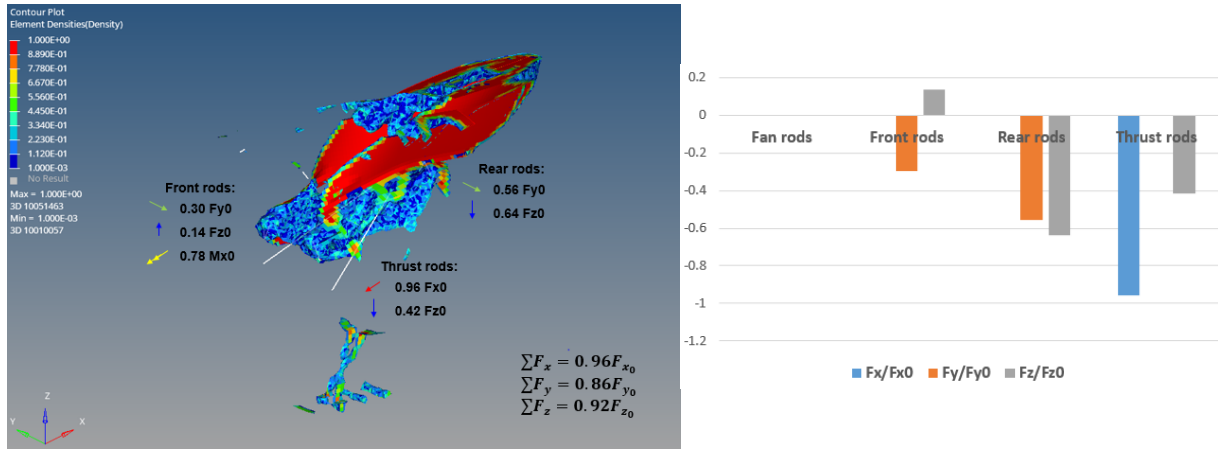


Figure 7.2: *FRMX* architecture - Loads transmitted to the Power Plant Structure by the connecting rods for an academic load case - $F_{x0}, F_{y0}, F_{z0}, M_{x0}$ are the resultant applied load components - Complete Formulation

- As for the previous solutions, the volume fraction constraint is violated at the first iterations. To make it fulfilled, the compliance must increase. Then, once the constraint fulfilled, the deformation energy is minimized;
- Even if the continuation methods cause more evident irregularities, the solution reached the *Regular Convergence* after 125 iterations;
- the load case 2018, together with the 2019, 1193 and 2192, are again the ones with the highest energy deformation for the Design Space.
- the M_{OGV} and the $TSFC$ are initially inactive. They increase fast during the first 20 iterations in order to make the volume fraction constraint fulfilled. Once that happens, they decrease as well as the compliance. Finally they increase again in order to further reduce the compliance: the $TSFC$ constraint becomes active after 50 iterations while the M_{OGV} becomes active only after about 90 iterations.

On the other side, the introduction of the additional constraints induces some differences concerning the Power Plant Structure performances. The architecture performances are compared respect to the *FRMX* solution which was obtained by the *Classic Formulation*. First of all, almost all the load cases undergo an higher energy deformation. However, this compliance augmentation results enough limited since the $\max_{i \in J} C$ increases by only 3.7% (fig. 7.7).

On the other hand, this limited compliance increase allows performances improvements that are not negligible: all the load conditions benefit of a reduction on tip clearances and M_{OGV} . More specifically, the $\max_{i \in J_1} TSFC$ is reduced by 17.7% (fig.7.9) and the $\max_{i \in J_2} M_{OGV}$ by 18.0% (fig.7.8). It is worth to remember that the optimization problem

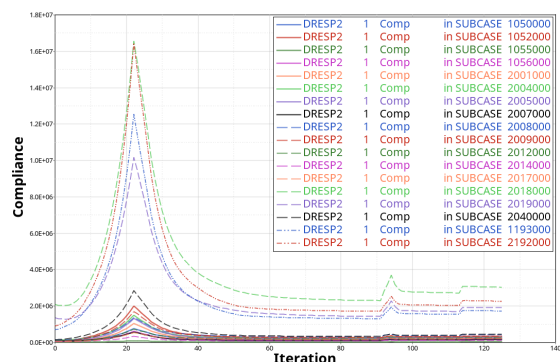


Figure 7.3: Design space compliance history over iterations for *FRMX* configuration - Complete formulation

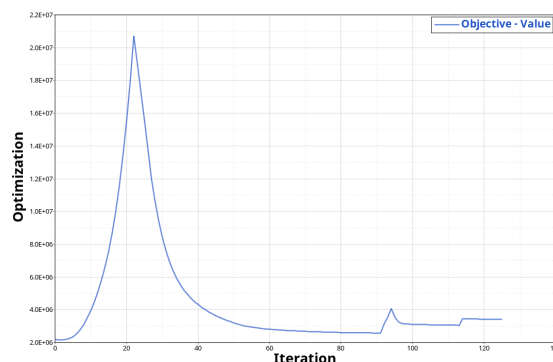


Figure 7.4: Optimization Objective history over iterations for *FRMX* configuration - Complete formulation

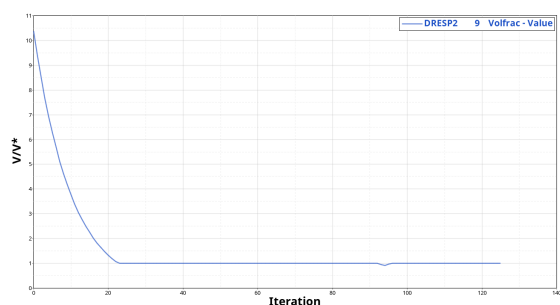


Figure 7.5: V/V^* history over iterations for *FRMX* configuration - Complete formulation

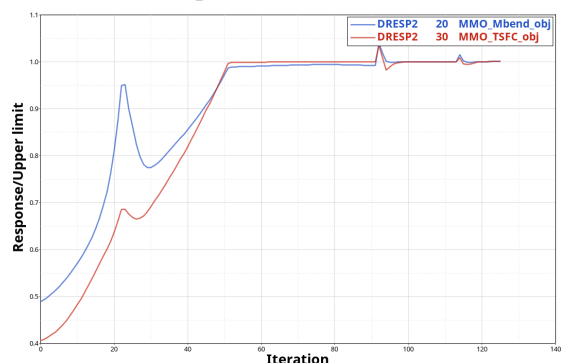


Figure 7.6: Optimization Responses history over iterations for *FRMX* configuration - Complete formulation

formulation imposed a 15% reduction for both $TSFC$ and M_{OGV} . But these constraints have been actually imposed on the p – aggregations value, which is a conservative approximation of the max function. That is the reason why the obtained performances are better than the upper limits of the imposed constraints. Once again the lower bifi proves to be an efficient component in order to reduce the tip clearances. Moreover, the *cowl load sharing* has been proven to be important for the improvement of the engine displacements control.

7.2 Pareto front

In a multi-objective optimization problem, a Pareto optimal solution is a solution where none of the objective can be further improved without degrading at least one other objective. The set of Pareto optimal solutions is called Pareto Front. In this project, the term *Pareto Front* has been referred to the set of solutions that have been obtained by

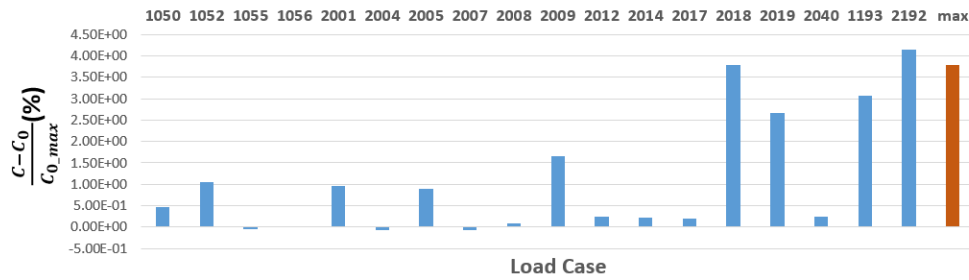


Figure 7.7: Design Space compliance variation of the Complete formulation compared to the Classic Formulation

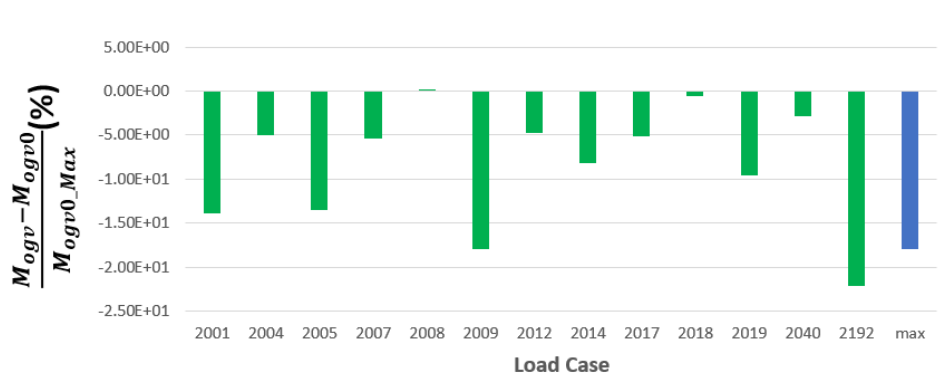


Figure 7.8: OGV bending moment variation of the Complete formulation compared to the Classic Formulation

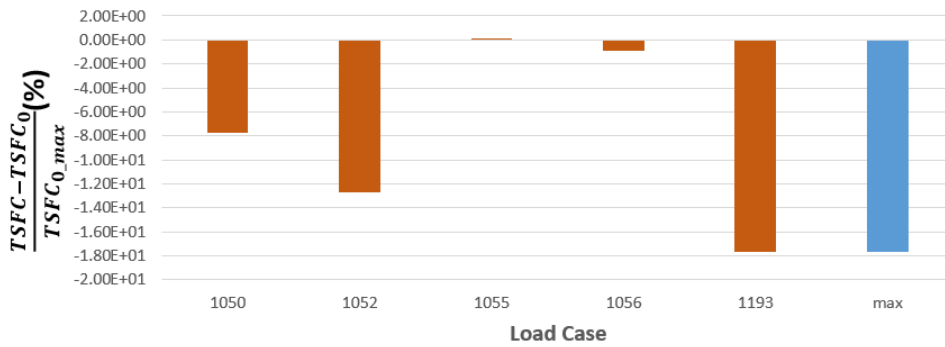


Figure 7.9: TSFC aggregation variation of the Complete formulation compared to the Classic Formulation

solving the *Complete Formulation* Optimization problem on the FRMX configuration for different values of upper bounds on the design criteria. That has been done in order to study the influence of the Design Criteria on the solution stiffness. In this paragraph, a Pareto front for each constraint which is associated with the engine displacement ($TSFC$

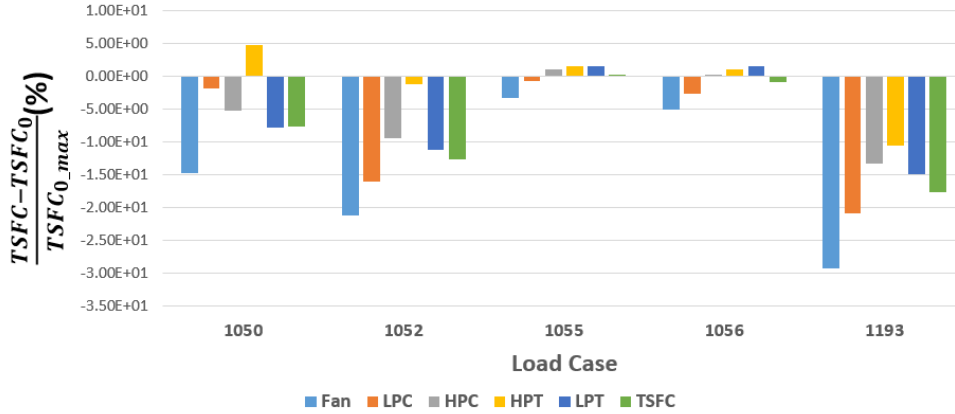


Figure 7.10: TSFC variation for each component and its aggregation of the Complete formulation compared to the Classic Formulation

and M_{OGV}) is shown and discussed. The convergences plot of the objective and constraints for every point of the Pareto front can be found in the Annexes. For each point of the Pareto front, the *FRMX* configuration was considered and the *Complete Formulation* of the optimization problem was solved.

7.2.1 *TSFC* Pareto Front

In order to evaluate the influence of the *TSFC* constraint on the *FRMX* solution, its upper limit constraint was gradually decreased. At the same time, the upper limit of the M_{OGV} was left unchanged (-15% respect to the *Classic Formulation* solution). Fig.7.11 shows the evolution of the p-norm of the compliance respect to the *TSFC* upper limit constraint. In the figure, both $\pi(C_{j \in J}, p)$ and $\pi(TSFC_{j \in J_1}, p)$ are normalized respect to the *Classic Formulation* values. It is evident that a stiffer Power Plant Structure involves a worse tip clearances control. This corroborates that compliance and *TSFC* variation are antagonist objectives.

Moreover, fig. 7.12 shows also the evolution of $\pi(M_{OGV_{j \in J_2}}, p)$ respect to the variation of the *TSFC* upper limit constraint. Even this time the axis values are normalized respect to the *Classic Formulation p-norm* values. It is evident that the reduction on *TSFC* variation caused by tip clearance degradation and the total bending moment on the OGV blades are not conflicting objectives.

In the fig.7.13, the already discussed solution imposing 15% reduction on both the design criteria is shown. Figures 7.13, 7.14, 7.15, 7.16 show the evolution of the Power Plant Structure by gradually further reducing the upper limit of the *TSFC* constraint:

- In fig.7.14, the rear rib is removed in order to allow a symmetric link from the lower

bifi and the IFS to the rear mount. These links can allow a more direct load path from the lower TRU beams and the IFS to the Power Plant Structure: the *cowl load sharing* becomes more and more necessary to limit the tip clearances variation. Moreover, they also surround the engine core by providing a further support to the motor. In the optimization response history (fig.9.4 in the Annexes), it is possible to remark that the constraint on the bending moment of the OGV blades is not active any more. This means, in accordance to fig. 7.12, that the $TSFC$ reduction is also beneficial for the M_{OGV} .

- By further reducing the $\pi(TSFC_{j \in J_1}, p)$ by 10% (fig. 7.15), the front mount is made less robust and the reinforcement from the lower bifi to the rear mount are less thin: the load path from the lower TRU beams and the IFS to the Design Space is made more stiff. The convergence graphs in Annexes shows that the constraint on the bending moment of the OGV blades is more inactive than in the previous point;
- Finally, demanding a further 10% reduction on $TSFC$, the density distribution in fig.7.16 was obtained. As for the precedent points the *cowl load sharing* becomes even more important. The constraint of the bending moment on the OGV blades is still less active than in the previous points (fig.9.12).

Looking at density distributions obtained in the Pareto Front, it is evident that the secondary structures participate to the primary load path in a more important way if the upper limit of the constraint $TSFC$ is reduced. So we can conclude that the *cowl load sharing* makes the structure less stiff but it is essential if the impact of the tip clearance variation on the TSC has to be reduced. Moreover, it seems that the tip clearances variation is more controlled if the core engine is contained by an additional support made up of two links between the lower bifi and the rear mount.

7.2.2 M_{OGV} Pareto

Same logic as for the previous Pareto Front was applied in order to assess the influence of the OGV bending moment constraint on the solution stiffness. The Pareto Front was obtained by reducing the M_{OGV} upper limit by 15%, 55% and 80% respect to the $\pi(M_{OGV_{j \in J_2}}, p)$ value obtained by the *Classic Problem* solution (while the $TSFC$ upper limit was kept equal to -15% respect to the *Classic Problem* value).

In fig. 7.17 the Pareto front is shown where the axis values are normalized respect to the the *Classic Problem* solution values. It is evident that the upper limit of the bending moment constraint on the OGV blade doesn't initially impact very much the Power Plant Structure stiffness up to -55% of M_{OGV} reduction. On the other hand, the $\pi(C_{j \in J}, p)$ increases by 10% of $\pi(C_{0j \in J}, p)$ when the upper limit of the M_{OGV} constraint is reduced from -55% to -80% respect to the *Classic Problem* solution value. In the fig.7.18, the

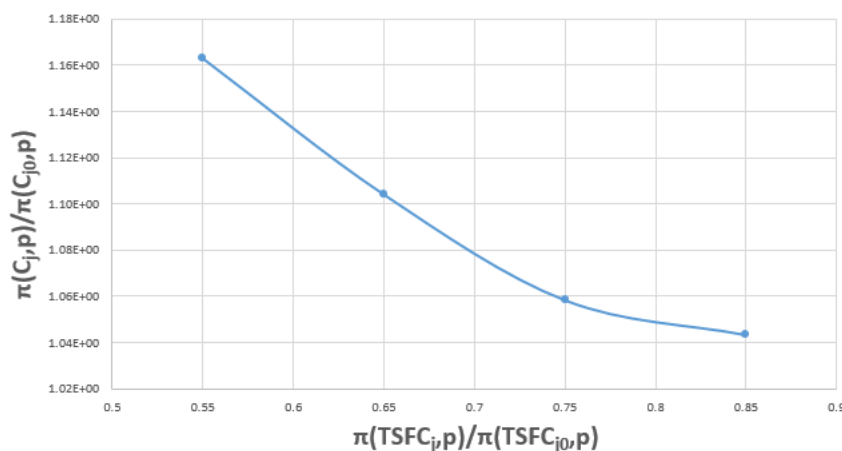


Figure 7.11: Pareto Front respect to $TSFC$ constraint - $FRMX$ configuration - Complete formulation

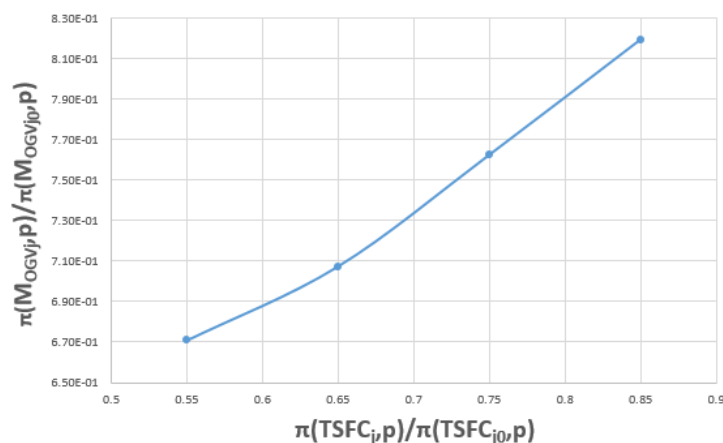


Figure 7.12: Variation of the bending moment on the OGV blades that is obtained by gradually decreasing the $TSFC$ upper limit - $FRMX$ configuration - Complete formulation

already discussed solution imposing 15% reduction on both the design criteria is shown. Figures 7.19 and 7.20 show the evolution of the Power Plant Structure by gradually further reducing the upper limit of the M_{OGV} constraint:

- in fig.7.19 the first contact zone with the IFS is made more robust respect to the previous point of the Pareto Front at the expense of a less stiff front mount. Also the third forward interface area between the Design Space and the IFS is larger. That means that the IFS can contribute more to the primary load path in this solution respect to the previous one (fig.7.18). The increase of the *cowl load sharing* makes the compliance slightly increase. Moreover, in the responses history (fig. 9.16 in the Annexes), it is possible to remark that the $TSFC$ constraint is not active anymore:

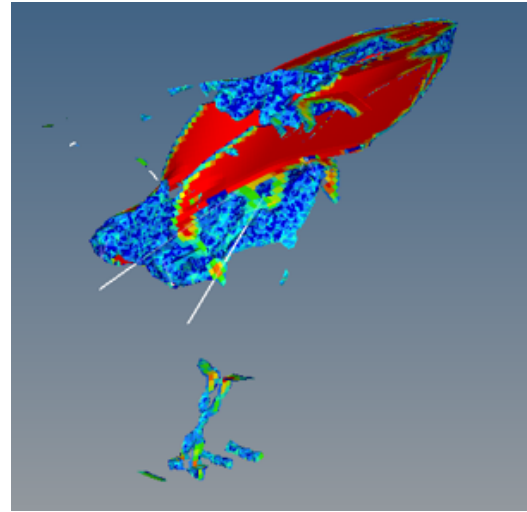
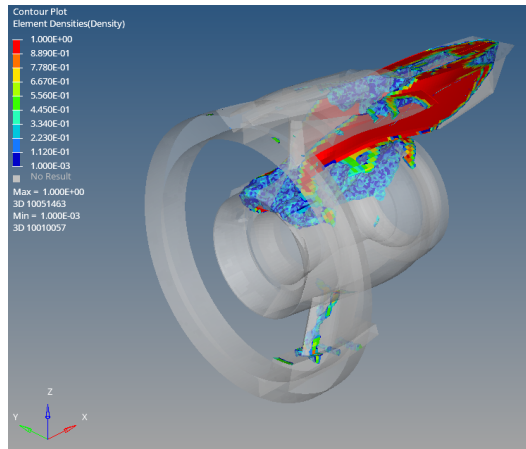


Figure 7.13: $\pi(TSFC_{j \in J_1}, p) / \pi(TSFC_{0j \in J_1}, p) = 0.85$; $\pi(M_{OGV_{j \in J_2}, p}) / \pi(M_{OGV_{0j \in J_2}, p}) = 0.85$ - Complete Formulation - Threshold=0.2

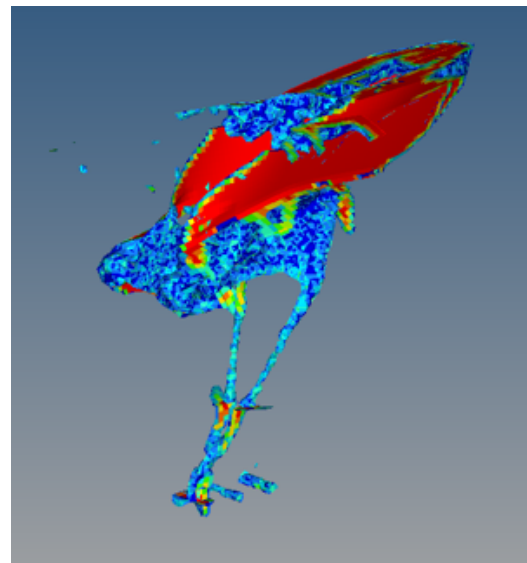
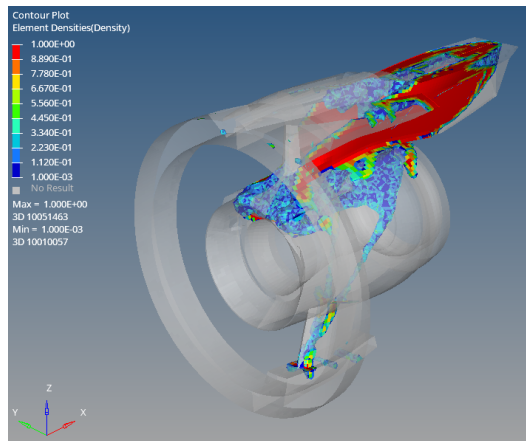


Figure 7.14: $\pi(TSFC_{j \in J_1}, p) / \pi(TSFC_{0j \in J_1}, p) = 0.75$; $\pi(M_{OGV_{j \in J_2}, p}) / \pi(M_{OGV_{0j \in J_2}, p}) = 0.85$ - Complete Formulation - Threshold=0.2

that means that the reduction of M_{OGV} is also beneficial for the tip clearances control and corroborates the fact that $TSFC$ and M_{OGV} are not antagonist objectives.

- in fig. 7.20 the lower bif is directly connected to the rear mount by two symmetric links meaning that the lower TRU beams contribute in an important way to the primary load path. Also the IFS has more importance for the transmission of loads since the 2 central contact area with the Design Space are now joined to form one

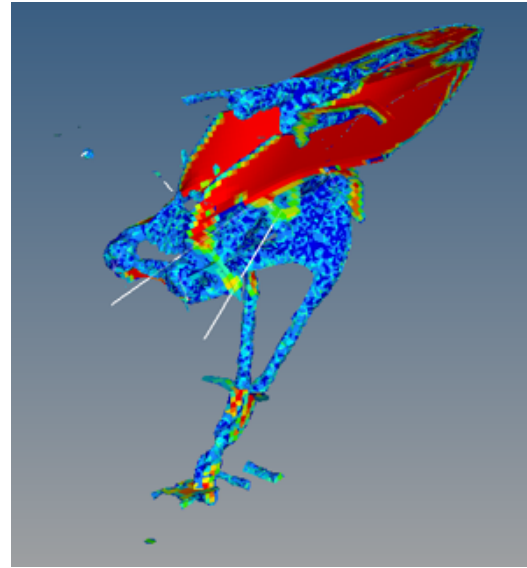
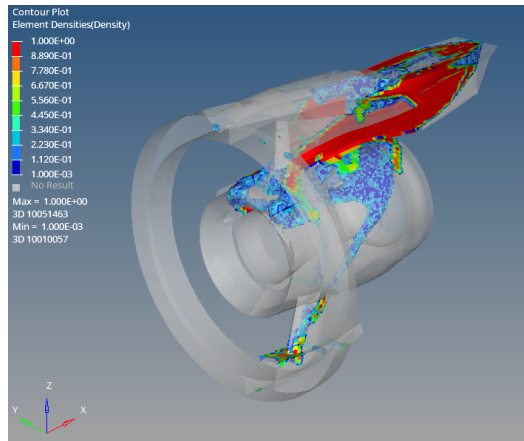


Figure 7.15: $\pi(TSFC'_{j \in J_1}, p) / \pi(TSFC_{0j \in J_1}, p) = 0.65$; $\pi(M_{OGV'_{j \in J_2}}, p) / \pi(M_{OGV_{0j \in J_2}}, p) = 0.85$ - Complete Formulation - Threshold=0.2

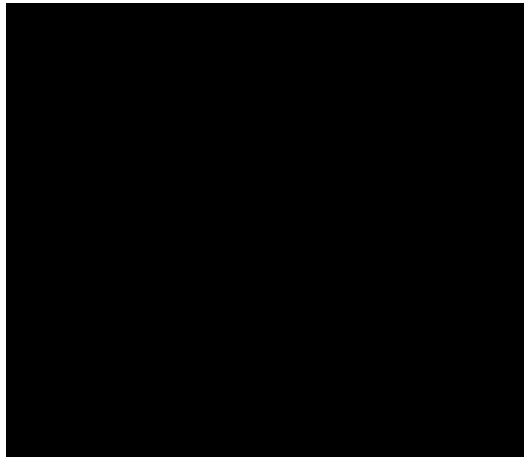


Figure 7.16: $\pi(TSFC'_{j \in J_1}, p) / \pi(TSFC_{0j \in J_1}, p) = 0.55$; $\pi(M_{OGV'_{j \in J_2}}, p) / \pi(M_{OGV_{0j \in J_2}}, p) = 0.85$ - Complete Formulation - Threshold=0.2

that is more robust. All that at the expense of a much less robust front mount. As seen for the *TSFC* Pareto Front, the two links between the Design Space and the lower bifi are also meant to contain the engine core.

With this Pareto Front, the relationship between the design criteria and the solution stiffness has been confirmed and. Moreover, once again the cowl load sharing seems necessary

to improve the design criteria performances.

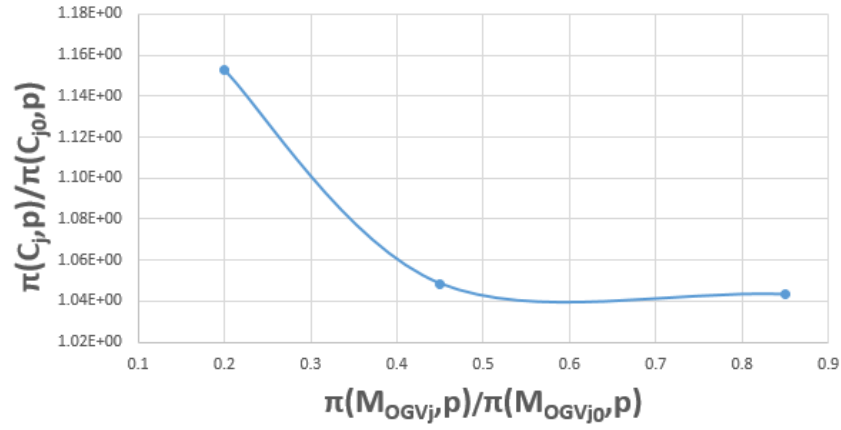


Figure 7.17: Pareto Front respect to M_{OGV} constraint - $FRMX$ configuration - Complete formulation

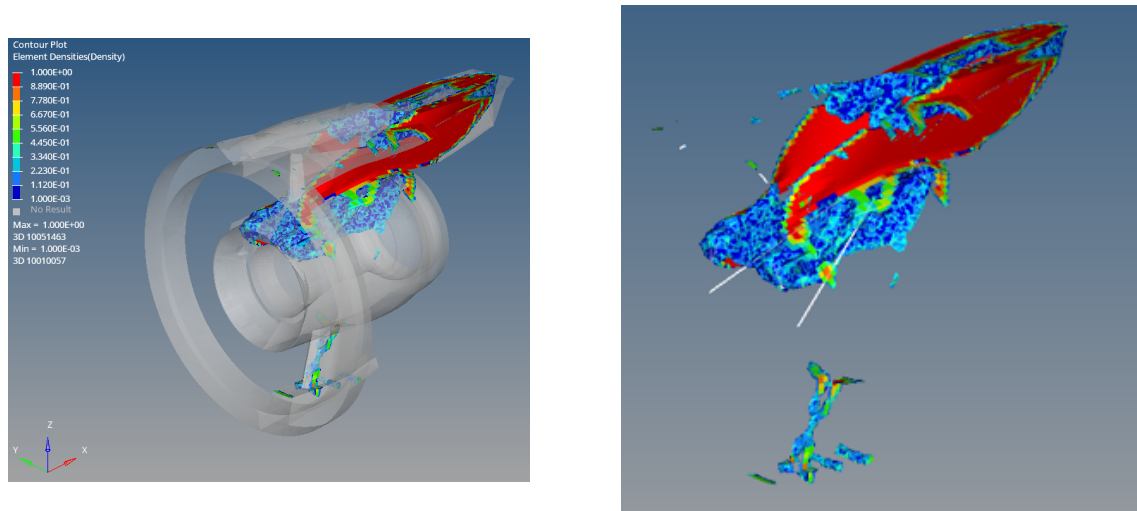


Figure 7.18: $\pi(TSFC_{j \in J_1}, p) / \pi(TSFC_{0j \in J_1}, p) = 0.85$ $\pi(M_{OGV_{j \in J_2}, p}) / \pi(M_{OGV_{0j \in J_2}, p}) = 0.85$ - Complete Formulation - Threshold=0.2

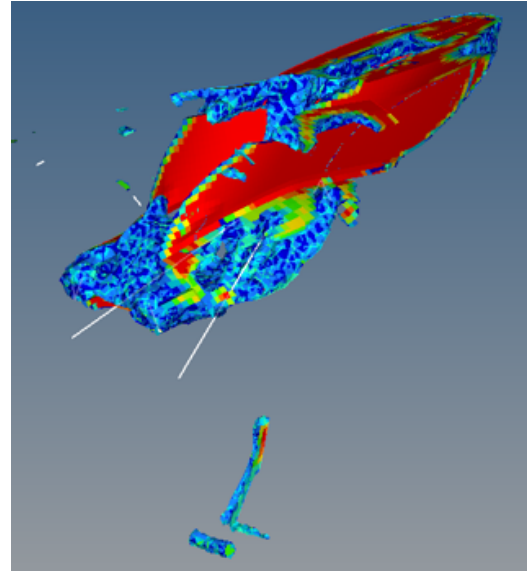
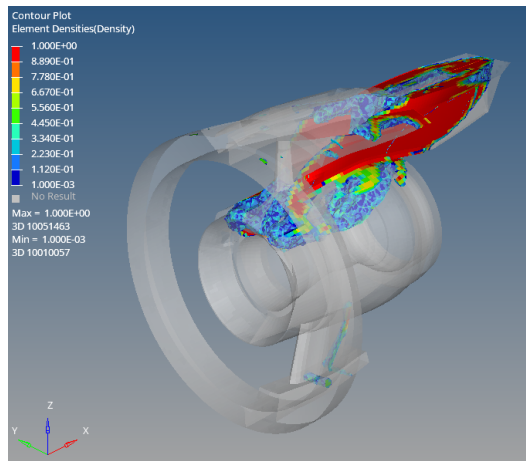


Figure 7.19: $\pi(TSFC_{j \in J_1}, p) / \pi(TSFC_{0j \in J_1}, p) = 0.85$ $\pi(M_{OGV_{j \in J_2}, p}) / \pi(M_{OGV_{0j \in J_2}, p}) = 0.45$ - Complete Formulation - Threshold=0.2

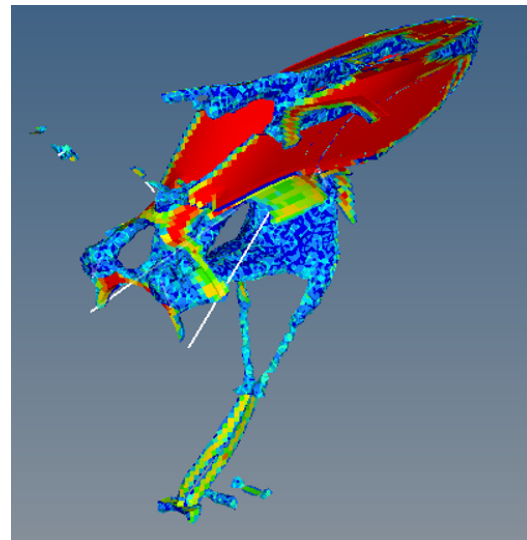
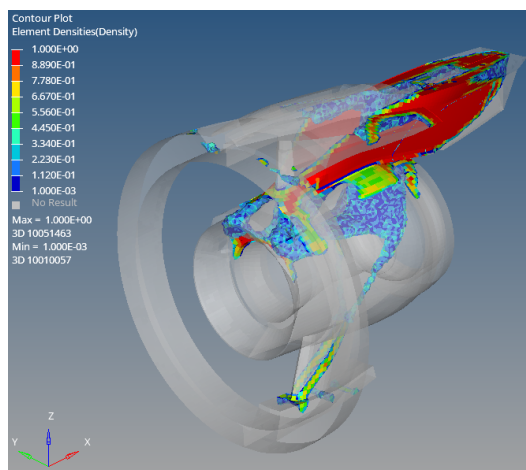


Figure 7.20: $\pi(TSFC_{j \in J_1}, p) / \pi(TSFC_{0j \in J_1}, p) = 0.85$ $\pi(M_{OGV_{j \in J_2}, p}) / \pi(M_{OGV_{0j \in J_2}, p}) = 0.20$ - Complete Formulation - Threshold=0.2

Chapter 8

Conclusions and Perspectives

Once the motivations and the objective of this work were presented, the structural optimization methods were briefly introduced. Several studies on the subject had already been done at Airbus: the main objective of this work was to move towards more realistic model hypothesis and to investigate more deeply the solutions by understanding the logic behind the optimized Power Plant Structure. From the results of the precedent chapters, it is possible to extract the following conclusions:

- the *Size Optimization* for the D-duct and C-Duct configurations showed that the lower bifi reduces the impact of tip clearances variation on *TSFC*;
- thanks to the *Size Optimization* on the IFS, it has been showed that a more stiff IFS would allow an important improvement in tip clearance control, especially for a D-duct configuration;
- to reduce the Degree of Static Indeterminacy results into a less stiff solution with degraded performances; on the other hand, to replace the glued surfaces between the Design Space and the engine by connecting rods is necessary to take the thermal expansion into account and to move towards more realistic model hypothesis;
- the configuration of assemblies referred as *FRMX*, where the torque moment is recovered on the front mount, results to be the stiffest one;
- in the configuration *REMX* and *FAN_REMX*, the rear rod in charge to recover the torque moment has not a sufficient moment arm to accomplish its function. Its moment arm is, in fact, limited by aerodynamic considerations. That is the reason why, by the minimization of the compliance, an hyperstatic solution is obtained, where secondary structures, like IFS a TRU beams, are part of the primary load path: this concept is referred as *cowl load sharing*;

- the *REMX* and *FAN_REMX*, where the *cowl load sharing* plays an important role, result to be less stiff but more efficient in terms of tip clearances and bending moment on the OGV than the *FRMX* solution. Table 8.1 summaries the analysed configurations performances obtained by the *Classic Formulation* optimization problem;
- by resolving the *Complete formulation* problem for the *FRMX* configuration the design criteria associated with the engine displacements (*TSFC* and M_{OGV}) could be improved. The *cowl load sharing* proves to be necessary to improve both the design criteria. However, a lost of stiffness would be necessary.

	$C_{\max}/C_{0\max}$	$TSFC_{\max}/TSFC_{0\max}$	$M_{OGV_{\max}}/M_{OGV_{0\max}}$
FRMX	1	1	1
REMX	1.28	0.77	0.78
FAN_REMX	1.41	0.39	0.74
TIE	0.73	0.77	0.95

Table 8.1: Performances summary - *Classic Formulation* Topology Optimization

Several aspects of the present work could be further investigated.

First of all a finer mesh in the Finite Element Method model would allow the topology optimization to find new load paths.

Then, the *cowl load sharing* should be eventually limited in order to avoid excessive loads on the secondary structures. That is the reason why it could be interesting and useful to introduce an upper bound also for the *cowl load sharing*.

Finally, in the present work, the position of the connecting rods have been supposed fixed during the topology optimization. A crossed optimization, where the position of the connecting rods would be optimized at the same time as the density field of the Design Space, could eventually propose improved engine interfaces.

Chapter 9

Annexes

9.1 *TSFC* Pareto - Optimization Convergence

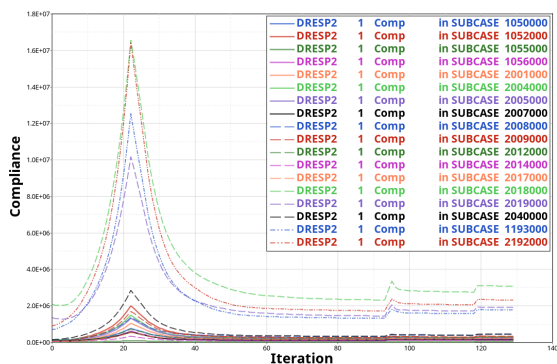


Figure 9.1: Design space compliance history over iterations for *FRMX* configuration - Complete formulation - $TSFC/TSFC_0 = 0.75 M_{OGV}/M_{OGV_0} = 0.85$

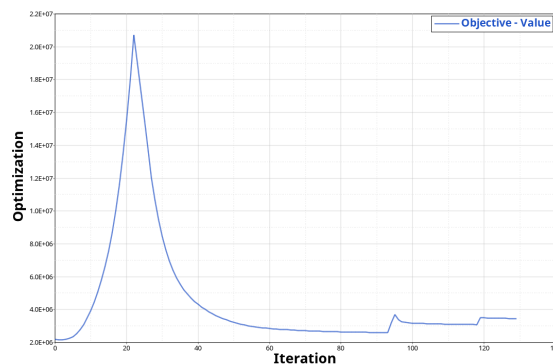


Figure 9.2: Optimization Objective history over iterations for *FRMX* configuration - Complete formulation - $TSFC/TSFC_0 = 0.75 M_{OGV}/M_{OGV_0} = 0.85$

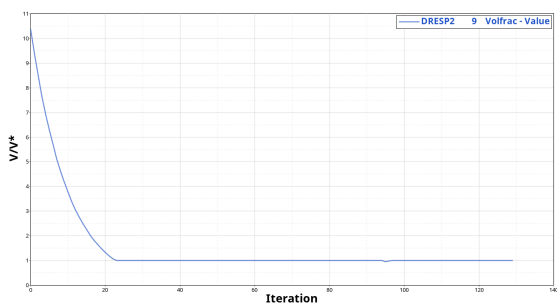


Figure 9.3: V/V^* history over iterations for *FRMX* configuration - Complete formulation - $TSFC/TSFC_0 = 0.75 M_{OGV}/M_{OGV_0} = 0.85$

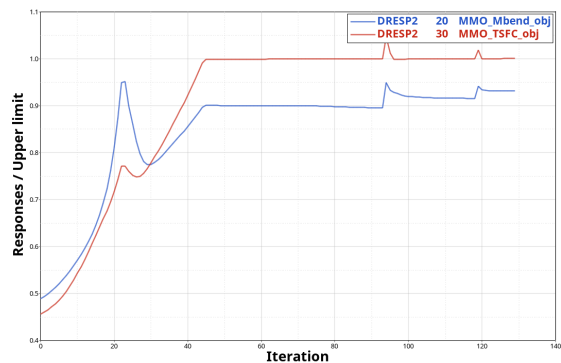


Figure 9.4: Optimization Responses history over iterations for *FRMX* configuration - Complete formulation - $TSFC/TSFC_0 = 0.75 M_{OGV}/M_{OGV_0} = 0.85$

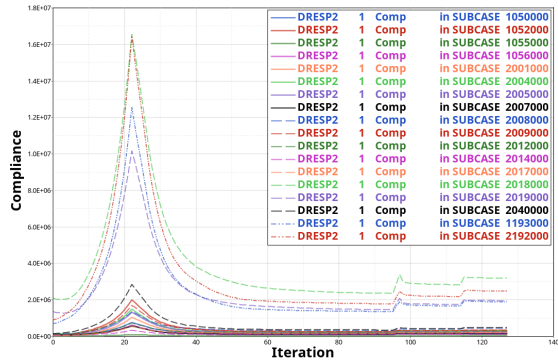


Figure 9.5: Design space compliance history over iterations for *FRMX* configuration - Complete formulation - $TSFC/TSFC_0 = 0.65$ $M_{OGV}/M_{OGV_0} = 0.85$

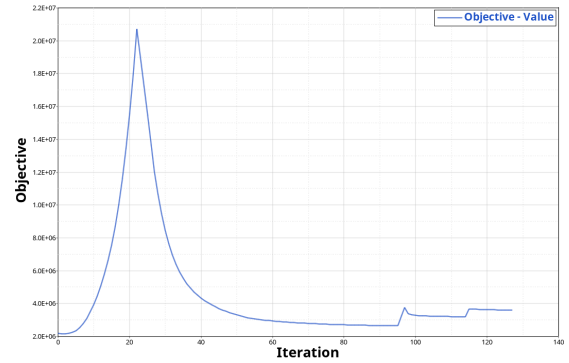


Figure 9.6: Optimization Objective history over iterations for *FRMX* configuration - Complete formulation - $TSFC/TSFC_0 = 0.65$ $M_{OGV}/M_{OGV_0} = 0.85$

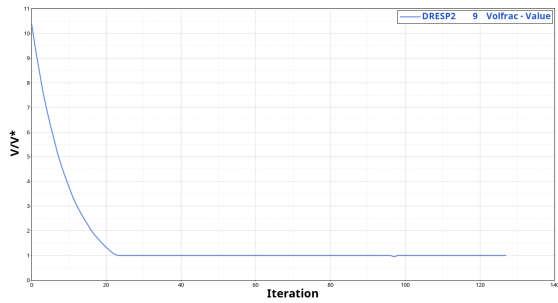


Figure 9.7: V/V^* history over iterations for *FRMX* configuration - Complete formulation - $TSFC/TSFC_0 = 0.65$ $M_{OGV}/M_{OGV_0} = 0.85$

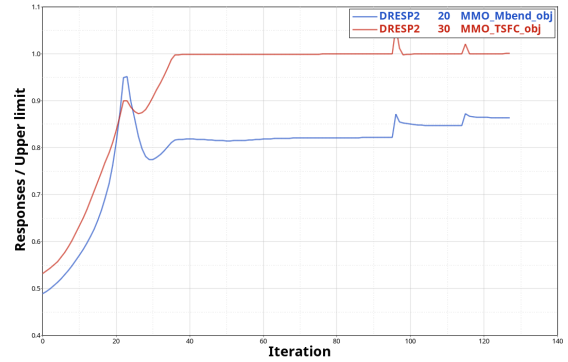


Figure 9.8: Optimization Responses history over iterations for *FRMX* configuration - Complete formulation - $TSFC/TSFC_0 = 0.65$ $M_{OGV}/M_{OGV_0} = 0.85$

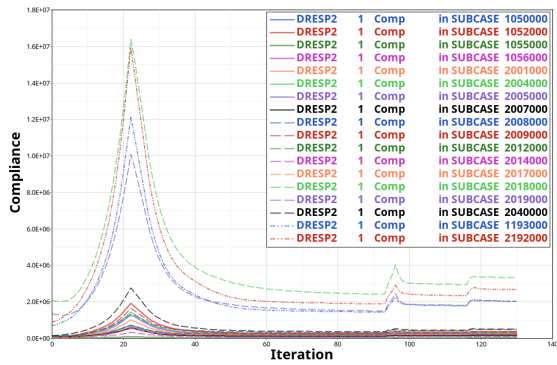


Figure 9.9: Design space compliance history over iterations for *FRMX* configuration - Complete formulation - $TSFC/TSFC_0 = 0.55$ $M_{OGV}/M_{OGV_0} = 0.85$

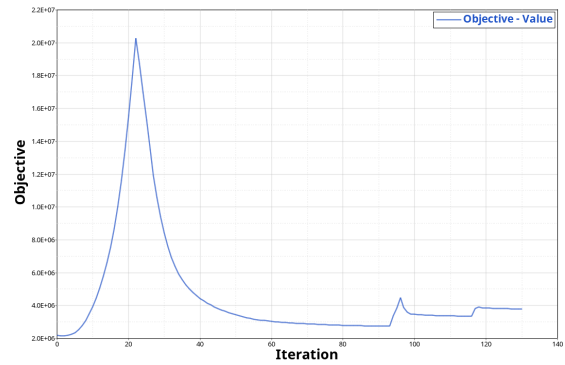


Figure 9.10: Optimization Objective history over iterations for *FRMX* configuration - Complete formulation - $TSFC/TSFC_0 = 0.55$ $M_{OGV}/M_{OGV_0} = 0.85$

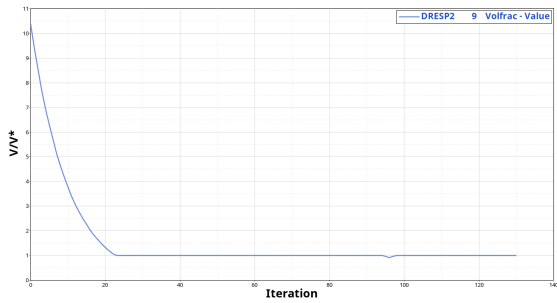


Figure 9.11: V/V^* history over iterations for *FRMX* configuration - Complete formulation - $TSFC/TSFC_0 = 0.55$ $M_{OGV}/M_{OGV_0} = 0.85$

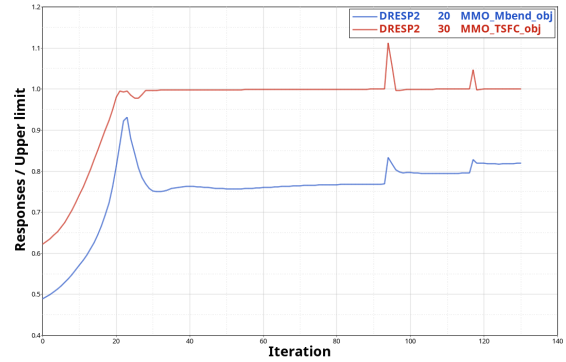


Figure 9.12: Optimization Responses history over iterations for *FRMX* configuration - Complete formulation - $TSFC/TSFC_0 = 0.55$ $M_{OGV}/M_{OGV_0} = 0.85$

9.2 M_{OGV} Pareto - Optimization Convergence

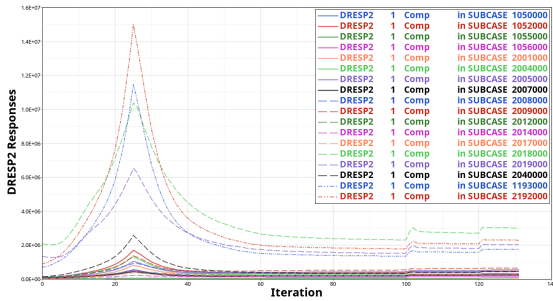


Figure 9.13: Design space compliance history over iterations for *FRMX* configuration - Complete formulation - $TSFC/TSFC_0 = 0.85 M_{OGV}/M_{OGV_0} = 0.45$

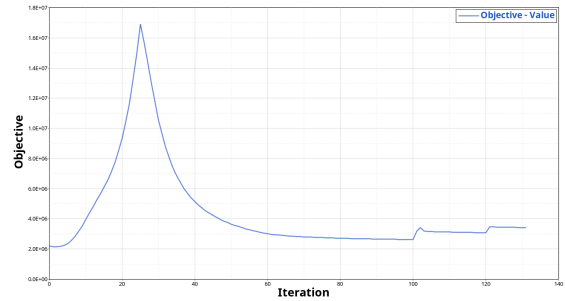


Figure 9.14: Optimization Objective history over iterations for *FRMX* configuration - Complete formulation - $TSFC/TSFC_0 = 0.85 M_{OGV}/M_{OGV_0} = 0.45$

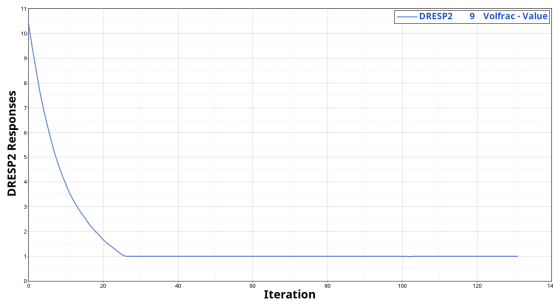


Figure 9.15: V/V^* history over iterations for *FRMX* configuration - Complete formulation - $TSFC/TSFC_0 = 0.85 M_{OGV}/M_{OGV_0} = 0.45$

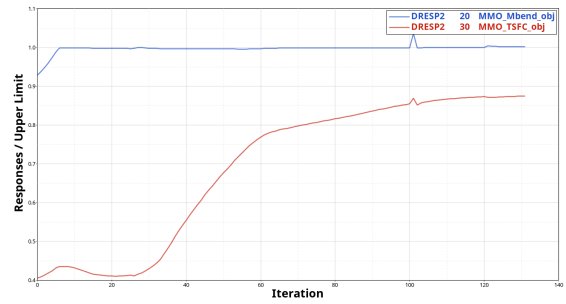


Figure 9.16: Optimization Responses history over iterations for *FRMX* configuration - Complete formulation - $TSFC/TSFC_0 = 0.85 M_{OGV}/M_{OGV_0} = 0.45$

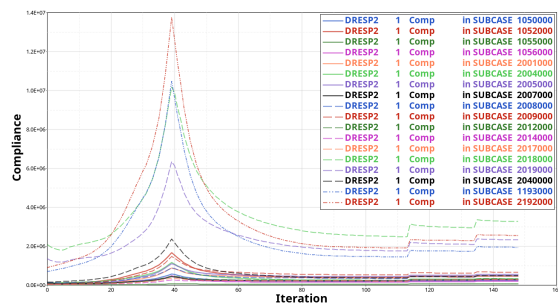


Figure 9.17: Design space compliance history over iterations for *FRMX* configuration - Complete formulation - $TSFC/TSFC_0 = 0.85 M_{OGV}/M_{OGV_0} = 0.20$

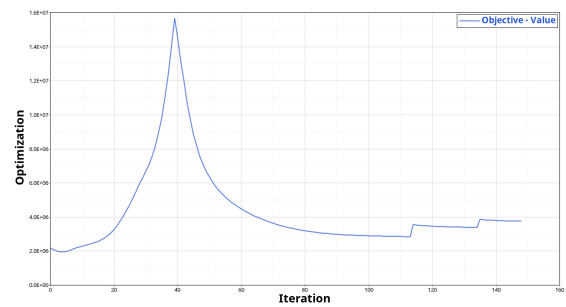


Figure 9.18: Optimization Objective history over iterations for *FRMX* configuration - Complete formulation - $TSFC/TSFC_0 = 0.85 M_{OGV}/M_{OGV_0} = 0.20$

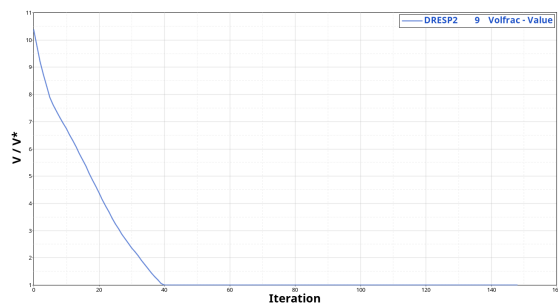


Figure 9.19: V/V^* history over iterations for *FRMX* configuration - Complete formulation - $TSFC/TSFC_0 = 0.85 M_{OGV}/M_{OGV_0} = 0.20$

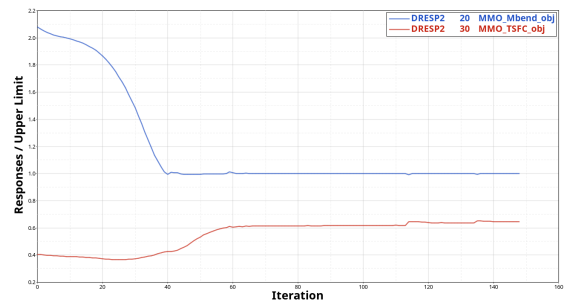


Figure 9.20: Optimization Responses history over iterations for *FRMX* configuration - Complete formulation - $TSFC/TSFC_0 = 0.85 M_{OGV}/M_{OGV_0} = 0.20$

Bibliography

- [Airbus] Airbus. *Global Market Forecast*.
- [A.R. Diaz 1995] O. Sigmund A.R. Diaz. *Checkerboard patterns in layout optimization*. Structural Optimization, 10:40-45, 1995.
- [Bendsøe 1995] M.P. Bendsøe. *Optimization of structural topology, shape and material*. Springer, 1995.
- [Boeing] Boeing. *Commercial market outlook*.
- [C. Fleury 1982] V. Braibant C. Fleury. *Prise en compte de contraintes linéaires dans les méthodes duales d'optimisation structurale*. LTAS Report SF-107, University of Liège, 1982.
- [C. Fleury 1986] V. Braibant C. Fleury. *Structural optimization: a new dual method using mixed variables*. International Journal for numerical methods in engineering, 23:409-428, 1986.
- [Capasso 2019] G. Capasso. *Structural optimization for Propulsion Airframe*. Master Thesis, 2019.
- [C.E. Hughes 2013] J.D. Heidmann C.E. Hughes D.E. Van Zante. *Aircraft Engine Technology for Green Aviation to Reduce Fuel Burn*. 2013.
- [C.Fleury 1979] C.Fleury. *Structural weight optimization by dual methods of convex programming*. Internal Journal for Numerical Methods in Engineering, 14:1761-1783, 1979.
- [Clemen 2010] Carsten Clemen. *Aero-mechanical optimisation of a structural fan outlet guide vane*. Structural and Multidisciplinary Optimization, 2010.
- [Coniglio 2019] S. Coniglio. *Optimisation topologique à formalisme Eulérien et Lagrangien appliquée à la conception d'un ensemble propulsif*. PHD, Institut Supérieur de l'Aéronautique et de l'Espace, 2019.

- [C.S. Jog 1996] R.B. Haber C.S. Jog. *Stability of finite element models for distributed-parameter optimization and topology design*. Computer Methods in Applied Mechanics and Engineering, 130:203-223, 1996.
- [E. Terrenoire 2019] T. Gasser O. Penanhoat E. Terrenoire D. A. Hauglustaine. *The contribution of carbon dioxide emissions from the aviation sector to future climate change*. Environmental Research Letters, 2019.
- [E.S. Hendricks 2012] M.T. Tong E.S. Hendricks. *Performance and Weight Estimates for an Advanced Open Rotor Engine*. 2012.
- [Falk 1967] J.E. Falk. *Lagrange multipliers and nonlinear programming*. Journal of Mathematical Analysis and Applications, 19:141-159, 1967.
- [Fleury 1989] C. Fleury. *Conlin: an efficient dual optimizer based on convex approximation concepts*. Structural Optimization, 1:81-89, 1989.
- [G. Allaire 1993] R.V. Kohn G. Allaire. *Topology optimization and optimal shape design using homogenization*. Topology Design of Structures, 207-218, 1993.
- [G. Allaire 2005] F. Jouve G. Allaire. *A level-set method for vibration and multiple loads in structural optimization*. Computer methods in applied mechanics and engineering, 194(30-33):3269-3290, 2005.
- [G. Kreisselmeier 1980] R. Steinhauser G. Kreisselmeier. *Systematic control design by optimizing a vector performance index*. Computer aided design of control systems, pages 113-117, 1980.
- [Guo X. 2014] Zhong W. Guo X. Zhang W. *Doing Topology Optimization Explicitly and Geometrically—A New Moving Morphable Components Based Framework*. Journal of applied Mechanics, 81(8): 081009 (12 pages), 2014.
- [GW. Jang 2003] Y.Y. Kim D. Sheen C. Park MN. Kim GW. Jang J.H. Jeong. *Checkerboard-free topology optimization using non-conforming finite elements*. International journal for numerical methods in engineering, 2003.
- [H. Kazemi 2018] J. Norato H. Kazemi A. Vaziri. *Topology optimization of structures made of discrete geometric components with different materials*. Journal of Mechanical Design, 140(11):111401, 2018.
- [H. Kazemi 2020] J. Norato H. Kazemi A. Vaziri. *Multi-material Topology Optimization of Lattice Structures using Geometry Projection*. PHD, University of Connecticut, 2020.

- [H.W. Kuhn 1951] W. Tucker H.W. Kuhn. *Nonlinear Programming*. Traces and Emergence of Nonlinear Programming, pp247-258, 1951.
- [ICAO 2018] ICAO. *The World of Air Transport in 2018*. 2018.
- [J. Liu 2016] Y. Ma J. Liu. *A survey of manufacturing oriented topology optimization methods*. Advances in Engineering Software, 100: 161-175, 2016.
- [J. Norato 2004] D. Tortorelli M.P. Bendsoe J. Norato R. Haber. *A geometry projection method for shape optimization*. International journal for numerical methods in engineering, 60:2289-2312., 2004.
- [J.A. Sethian 2000] A. Wiegmann J.A. Sethian. *Structural boundary design via level set and immersed interface methods*. Journal of Computational Physics, 163(2):489-528, 2000.
- [James Denman 2011] Olivier de Weck James Denman Sinha Kaushlk. *Technology Insertion in Turbofan Engine and Assessment of Architectural Complexity*. 13th International Dependency and Structure Modelling Conference, Cambridge, Massachusetts, USA, 2011.
- [Ji-Hong Zhu 2015] Liang Xia Ji-Hong Zhu Wei-Hong Zhang. *Topology Optimization in Aircraft and Aerospace Structure Design*. Archives of Computational Methods in Engineering, 23:595–622, 2015.
- [J.Norato 2015] D.Tortorelli J.Norato B.Bell. *A geometry projection method for continuum-based topology optimization with discrete elements*. Computer methods in applied mechanics and engineering, 293:306-327, 2015.
- [Joshua D. Deaton 2013] Ramana V.Grandhi Joshua D. Deaton. *A survey of structural and multidisciplinary continuum topology optimization: post 2000*. Structural Multidisciplinary Optimization, 49: 1-38, 2013.
- [Karush 1939] W. Karush. *Minima functions of Several Variables with Inequalities as Side Constraints*. Dissertetion, Dept. of Mathematics, University of Chicago, CHicago, Illinois, 1939.
- [Kenneth H. Huebner 2001] Douglas E. Smith Ted G. Byrom Kenneth H. Huebner Donald L. Dewhurst. *The finite element method for enginners*. Wiley, 2001.
- [K.J. Melcher 2004] J.A. Kypuros K.J. Melcher. *Toward a Fast-Response Active Turbine Tip Clearance Control*. NASA/TM–2003-212627/REV1,16th International Symposium on Airbreathing Engines sponsored by the International Society for Airbreathing Engines, 2004.

- [Kohn 1986] R.V. Kohn. *Optimal Design and Relaxation of Variational Problems*. Communications on Pure and Applied Mathematics, 39:113-137, 1986.
- [K.T Zuo 2007] Y.Q Zhang J. Yang K.T Zuo L.P. Chen. *Study of key algorithms in topology optimization*. The International Journal of Advanced Manufacturing Technology, 32:787-796, 2007.
- [L. Ambrosio 1993] G. Buttazzo L. Ambrosio. *An optimal design problem with perimeter penalization*. Calculus of Variations and Partial Differential Equations, 1:55-69, 1993.
- [L. He 2007] S Osher L. He CY. Kao. *Incorporating topological derivatives into shape derivatives based level set methods*. Journal of Computational Physics, 225(1):891-909, 2007.
- [L.A. Schmit 1974] B.Farshi L.A. Schmit. *Some Approximation concepts for Structural Synthesis*. AIAA Journal, 12:692-699, 1974.
- [L.A. Schmit 1976] H.Miura L.A. Schmit. *Approximate Concepts for Efficient Structural Synthesis*. NASA CR-2552, March 1976.
- [L.A. Schmit 1980] C. Fleury L.A. Schmit. *Structural synthesis by combining approximation concepts and dual methods*. AIAA Journal, 18:1252-1260, 1980.
- [L.A.Schmit 1976] H.Miura L.A.Schmit. *A New Structural Analysis/Synthesis Capability - ACCESS 1*. AIAA Journal,14:661-671, 1976.
- [L.A.Schmit 1978] H. Miura L.A.Schmit. *An Advanced Structural Analysis/Synthesis Capability - ACCESS 2*. International Journal for Numerical Methods in Engineering, 12: 353-377, 1978.
- [Lasdon 1970] L.S. Lasdon. *Optimization theory for large systems*. Dover Publications, Inc., Mineola, New York, 1970.
- [Lootsma 1989] F.A. Lootsma. *A comparative study of primal and dual approaches for solving separable and partially separable nonlinear optimization problems*. Structural Optimization, 1:73-79, 1989.
- [M. Burger 2004] W. Ring M. Burger B. Hackl. *Incorporating topological derivatives into level set methods*. Journal of Computational Physics, 194(1):344-362, 2004.
- [M. Zhou 2001] G.I.N. ROzvary M. Zhou. *On the validity of ESO type methods in topology optimization*. Structural Multidisciplinary Optimization, 21:80-83, 2001.

- [M.B. Graf 1997] E.M. Greitzer F.E. Marble C.S. Tan M.B. Graf T.S. Wong. *Effects of non-axisymmetric tip clearance on axial compressor performance and stability*. Volume 1: Aircraft Engine; Marine; Turbomachinery; Microturbines and Small Turbomachinery., ASME, 1997.
- [M.P. Bendsøe 1988] N. Kikuchi M.P. Bendsøe. *Generating optimal topologies in structural design using a homogenization method*. Computer methods in applied mechanics and engineering, 71:197-224, 1988.
- [M.P. Bendsøe 1989] M.P. Bendsøe. *Optimal shape design as a material distribution problem*. Structural Optimization, 1:193-202, 1989.
- [M.Y. Wang 2003] D. Guo M.Y. Wang X. Wang. *A level set method for structural topology optimization*. Computer methods in applied mechanics and engineering, 192:227-246, 2003.
- [NASA 2013] NASA. *Green Aviation: a better way to treat the planet*. 2013.
- [Niordson 1983a] F.I. Niordson. *Optimal design of plates with a constraint on the slope of the thickness function*. International Journal of Solids and Structures, 41:1417-1434, 1983.
- [Niordson 1983b] F.I. Niordson. *Optimal design of plates with a constraint on the slope of the thickness function*. International Journal of Solids and Structures, 19:141-151, 1983.
- [O. Sigmund 1998] J. Petersson O. Sigmund. *Numerical instabilities in topology optimization: a survey on procedures dealing with checkboards, mesh-dependencies and local minima*. Structural Optimization, 16:68-75, 1998.
- [O.M. Querin 1998] Y.M. Xie O.M. Querin G.P. Steven. *Evolutionary structural optimization (ESO) using a bidirectional algorithm*. Engineering Computations, 15(8):2031-1048, 1998.
- [Oussama Rouetbi 2017] Bernand Anselmetti Henri Denoix Oussama Rouetbi Laurent Pierre. *ISO Tolerancing of hyperstatic mechanical systems with deformation control*. Advances on Mechanics, Design Engineering and Manufacturing, 2017.
- [Overvelde 2012] J. Overvelde. *The moving node approach in topology optimization*. Master's thesis, TU Delft, Delft University of Technology., 2012.
- [P. Duysinx 1998] O. Sigmund P. Duysinx. *New Developments in handling stress constraints in optimal material distribution*. 7th AIAA/USAF/NASA/ISSMO symposium on multidisciplinary analysis and optimization, 1998.

- [R.B. Haber 1996] M.P. Bendsøe R.B. Haber C.S. Jog. *A new approach to variable topology shape design using a constrain on perimeter*. Structural Optimization, 11:1-12, 1996.
- [Richter 2011] Hanz Richter. *Advanced control of turbofan engines*. Springer, 2011.
- [Rolls-Royce 2005] Rolls-Royce. *The jet engine*, 2005 edition. Rolls-Royce Technical Publications, 2005.
- [S. Lattime 2002] B. Steinetz S. Lattime. *Turbine Engine Clearance Control System: Current Practices and Future Directions*. AIAA-2002-3790, NASA/TM—2002-211794, 38th Joint Propulsion Conference and Exhibit, July 7–10, 2002., 2002.
- [S. Zhang 2016] A. Gain N. Lyu S. Zhang J. Norato. *A geometry projection method for the topology optimization of plate structures*. Structural Multidisciplinary Optimization, 54:1173-1190, 2016.
- [Sethian 1999] J.A. Sethian. *Level Set Methods and Fast Marching Methods: Evolving Interfaces in Computational Geometry, Fluid Mechanics, Computer Vision, ad Materials Science*. Cambridge University Press, 1999.
- [Sigmund 1994] O. Sigmund. *Design of material structures using topology optimization*. PhD Thesis, Department of Solid Mechanics, Technical University of Denmark, 1994.
- [Sigmund 1997] O. Sigmund. *On the design of compliant mechanisms using topology optimization*. Mechanics of Structures and Machines, 25:493-524, 1997.
- [W. Zhang 2016] J. Zhang X. Guo W. Zhang D. Li. *Minimum length scale control in structural topology optimization based on the Moving Morphable Components (MMC) approach*. Computer methods in applied mechanics and engineering, 311:327–355, 2016.
- [W. Zhang 2017a] J. Yuan J. Song X. Guo W. Zhang D. Li. *A new three-dimensional topology optimization method based on moving morphable*. Computational Mechanics, 59:647-665, 2017.
- [W. Zhang 2017b] J. Zhou D. Li X. Guo W. Zhang W. Yang. *Structural Topology Optimization Through Explicit Boundary Evolution*. Journal of Applied Mechanics, 84:011011 (10 pages), 2017.
- [W. Zhang 2018] J. Zhou Z. Du B. Li X. Guo W. Zhang D. Li. *A Moving Morphable Void (MMV)-based explicit approach for topology optimization considering stress constraints*. Computer methods in applied mechanics and engineering, 334:381-413, 2018.

- [Wei P. 2009] Xing X. Wei P. Yu Wang M. *A study on X-FEM in continuum structural optimization using a level set model*. Computer-Aided Design, 42(708-719), 2009.
- [Wolfe 1963] P. Wolfe. *A duality theorem for non-linear programming*. Quarterly of Applied Mathematics, 19:239-244, 1963.
- [X. Guo 2016] J. Zhang J. Yuan X. Guo W. Zhang. *Explicit structural topology optimization based on moving morphable components (MMC) with curved skeletons*. Computer methods in applied mechanics and engineering, 310: 711–748, 2016.
- [X. Lei 2019] Z. Du W. Zhang X. Guo X. Lei C. Liu. *Machine learning-driven real-time topology optimization under moving morphable component-based framework*. Journal of Applied Mechanics, 86(1): 011004 (9 pages), 2019.
- [X. Yang 2018] H. Tang X. Yang. *Performance Modeling and Optimization Assessment of Variable Pitch Fan for Ultrafan Engine*. Propulsion and Energy Forum, 2018.
- [Y.M. Xie 1997] G.P. Steven Y.M. Xie. *Evolutionary structural optimization*. Springer, 1997.